IMPLEMENTATION OF AN ACTUATOR DISC MODEL USING BLADE ELEMENT THEORY FOR PROPELLERS INTO SU2 SOFTWARE

A THESIS SUBMITTED TO
THE GRADUATE SCHOOL OF NATURAL AND APPLIED SCIENCES
OF
MIDDLE EAST TECHNICAL UNIVERSITY

BY

KAAN YENİPAZAR

IN PARTIAL FULFILLMENT OF THE REQUIREMENTS
FOR
THE DEGREE OF MASTER OF SCIENCE
IN
AEROSPACE ENGINEERING

SEPTEMBER 2023

Approval of the thesis:

IMPLEMENTATION OF AN ACTUATOR DISC MODEL USING BLADE ELEMENT THEORY FOR PROPELLERS INTO SU2 SOFTWARE

submitted by **KAAN YENİPAZAR** in partial fulfillment of the requirements for the degree of **Master of Science** i**n Aerospace Engineering, Middle East Technical University** by,

Prof. Dr. Halil Kalıpçılar
Dean, Graduate School of **Natural and Applied Sciences** _____

Prof. Dr. Serkan Özgen
Head of the Department, **Aerospace Engineering, METU** _____

Prof. Dr. Dilek Funda Kurtuluş
Supervisor, **Aerospace Engineering, METU** _____

Examining Committee Members:

Prof. Dr. Yusuf Özyörük
Aerospace Engineering, METU _____

Prof. Dr. Dilek Funda Kurtuluş
Aerospace Engineering, METU _____

Prof. Dr. Nafiz Alemdaroğlu
School of Civil Aviation, Atılım University _____

Assoc. Prof. Dr. Nilay Sezer Uzol
Aerospace Engineering, METU _____

Assist. Prof. Dr. Özge Başkan Perçin
Aerospace Engineering, METU _____

Date: 11.09.2023

I hereby declare that all information in this document has been obtained and presented in accordance with academic rules and ethical conduct. I also declare that, as required by these rules and conduct, I have fully cited and referenced all material and results that are not original to this work.

Name Last name : Kaan Yenipazar

Signature :

ABSTRACT

IMPLEMENTATION OF AN ACTUATOR DISC MODEL USING BLADE ELEMENT THEORY FOR PROPELLERS INTO SU2 SOFTWARE

Yenipazar, Kaan
Master of Science, Aerospace Engineering
Supervisor: Prof. Dr. Dilek Funda Kurtuluş

September 2023, 120 pages

The aim of the current study is to develop an actuator disc model in the SU2 (Stanford University Unstructured) CFD Solver using the blade element theory (BET) approach. The primary objective is to reduce computational costs and save time with accurate results. The integrated model has applications in optimizing rotating components such as propellers as well as accurately predicting wake structures, which is important for understanding slipstream effects in aircraft and wake interactions. The available methodologies in SU2 for simulating rotating blades include the steady-state rotating frame, unsteady sliding mesh, and the existing actuator disc model. The new actuator disc model proposed in this study is a steady-state model that assumes an infinite number of blades within the disc domain, making it applicable to varying flow conditions, such as the forward flight of helicopters or aircraft experiencing an angle of attack. In this model, the rotating parts are not physically represented in the numerical domain; instead, they are replaced by a disc, and their effects are implemented using momentum sources. The new model was validated by comparing it with experimental data and another CFD solver that is the rotating frame approach. These comparisons demonstrated that the new model is performs accurately and can be a fast alternative approach with enough accuracy compared to the expensive full rotor solutions with the rotating frame.

Keywords: SU2, Blade Element, CFD, Actuator Disc, Propeller

ÖZ

SU2 YAZILIMINDA PERVANELER İÇİN PALA ELEMAN TEORİSİ KULLANILARAK BİR AKTÜATÖR DİSK MODELİNİN UYGULANMASI

Yenipazar, Kaan
Yüksek Lisans, Havacılık ve Uzay Mühendisliği
Tez Yöneticisi: Prof. Dr. Dilek Funda Kurtuluş

Eylül 2023, 120 sayfa

Bu çalışmanın amacı, SU2 (Stanford Üniversitesi Yapılandırılmamış Ağ) pala elemanı teorisi (BET) yaklaşımını kullanarak alternatif bir aktüatör disk modeli geliştirmektir. Temel hedef, hesaplama maliyetlerini azaltmak, zaman tasarrufu sağlamak ve doğru sonuçlar elde etmektir. Entegre model, pervaneler gibi döner bileşenleri optimize etmek ve iz bölgeleri gibi yapıları doğru bir şekilde tahmin etmek için uygulamalara sahiptir. Bu, uçaklardaki hava akışı etkilerini anlamak için önemlidir. SU2 ile döner kanatları simüle etmek için mevcut olan yöntemler arasında daimi durumlu döner çerçeve, zamana bağlı kayar ağ ve mevcut aktüatör disk modeli bulunmaktadır. Bu çalışmada önerilen yeni aktüatör disk modeli, sonsuz sayıda pal içeren bir disk alanı varsayımıyla daimi durumlu/zamana bağlı olmayan bir modeldir, bu da helikopterlerin ileri uçuşu veya hücum açısındaki uçaklar gibi zamanla değişen akış koşullarına uygulanabilir olmasını sağlar. Bu modelde, dönen parçalar sayısal alan içinde fiziksel olarak temsil edilmez; bunun yerine bir disk ile değiştirilir ve etkileri momentum kaynakları kullanılarak uygulanır. Yeni model, deneysel verilerle ve döner çerçeve yaklaşımı olan başka bir akış çözücüsü ile karşılaştırılarak doğrulandı. Bu karşılaştırmalar, yeni modelin doğru bir şekilde performans gösterdiğini ve döner referans çerçevesi ile pahalı tam

rotor çözümlerine kıyasla yeterli doğrulukla hızlı bir alternatif yaklaşım olabileceğini gösterdi.

Anahtar Kelimeler: SU2, Pala elemanı teorisi, HAD, Aktüatör Disk, Pervane

To my beloved nephew Kuzey and niece İstiklal, whose bright futures inspire me to strive for excellence.

ACKNOWLEDGMENTS

I would like to express my heartfelt gratitude to the following individuals who have played a crucial role in the completion of this thesis:

Prof. Dr. Dilek Funda Kurtuluş, my supervisor, for her unwavering support, guidance, and patience throughout this research journey. Her expertise and open-door policy have been always invaluable.

My loving family, including my dad, mom, sisters, brothers, nephew, and niece, for their unwavering belief in me and their constant encouragement. Your support has been my driving force.

My dear friends, Furkan, Bolel, Şanal, Özge, and Umut Can, for their unwavering support and understanding during the ups and downs of this research.

Erdem Ayan, my former manager, for providing me with endless opportunities to grow and improve in my field. I am also grateful to Murat Canıbek, Görkem Demir and Mert Cangül for giving me this opportunity and their guidance during my time at Turkish Aerospace.

My colleagues at Turkish Aerospace and SimScale Gmbh, especially Caner Atlı, Kübra Yaldız, Altan Cevher, and Şeyda Aydın for their valuable contributions, support, and friendship throughout this journey.

TABLE OF CONTENTS

LIST OF TABLES

TABLES

LIST OF FIGURES

FIGURES

LIST OF ABBREVIATIONS

2D	2-Dimensional
3D	3-Dimensional
AEDISC	Aerospace Engineer’s Disc
AOA	Angle of Attack
APC	Advanced Precision Composites
AR	Aspect Ratio
BEM	Blade Element Momentum Theory
BET	Blade Element Theory
C++	Programming Language C++
CAD	Computer Aided Design
CFD	Computational Fluid Dynamics
CFG	Configuration File
DAT	Data File
ENSAM	École Nationale Supérieure d'Arts et Métiers
EVTOL	Electric Vertical Take-off and Landing
MT	Momentum Theory
NACA	National Advisory Committee for Aeronautics
NS	Navier-Stokes
O-Grid	O Shaped Grid Domain
PDE	Partial Derivative Equation
PIV	Particle Image Velocimetry
RANS	Reynolds Averaged Navier-Stokes Equations
RAD	Radian
RPM	Revolution Per Minute
RPS	Revolution Per Second

SST	Shear Stress Transport
SU2	Stanford University Unstructured
UAV	Unmanned Aerial Vehicle
UIUC	University of Illinois at Urbana-Champaign
URANS	Unsteady Reynolds Averaged Navier Stokes Equations

LIST OF SYMBOLS

A_1	First Coefficient to Calculate Lift Coefficient at High AOA
A_2	Second Coefficient to Calculate Lift Coefficient at High AOA
AR	Aspect Ratio of the Blades
B_1	First Coefficient to Calculate Drag Coefficient at High AOA
B_2	Second Coefficient to Calculate Drag Coefficient at High AOA
C_P	3D Power Coefficient of the Rotating Component
C_T	3D Thrust Coefficient of the Rotating Component
C_d	2D Drag Coefficient
$C_{d_{max}}$	Maximum Drag Coefficient of the Blade Section
$C_{d_{stall}}$	2D Drag Coefficient at Stall
C_l	2D Lift Coefficient
$C_{l_{rot}}$	2D Lift Coefficient after 3D Rotational Effects Included
$C_{l_{non-rot}}$	2D Lift Coefficient Before 3D Rotational Effects Included
C_{normal}	2D Sectional Normal Coefficient
C_{thrust}	2D Sectional Thrust Coefficient
C_{power}	2D Sectional Power Coefficient
$C_{tangent}$	2D Sectional Tangential Coefficient
D	Diameter of the Rotating Component
E	Internal Energy of Flow
F'	Normalized Force with respect to Cell Volume
F^c	Convective Fluxes
F^v	Viscous Fluxes

F_a	Force in Axial Direction
F_t	Force in Tangential Direction
F_x	Force in x Direction
F_y	Force in y Direction
F_z	Force in z Direction
H	Enthalpy
J	Advance Ratio of Blades
K	Velocity Gradient
M	Mach Number
P	Pressure
Q	Torque
R	Radius of the Blade
Re	Reynolds Number
T	Temperature of Flow
U	Flow Primitives
V_n	Velocity in Normal Direction in BEM
V_t	Velocity in Tangential Direction in BEM
V_{total}	Total Velocity of the Blade Section
a	Induction Factor for Axial Velocity
a'	Induction Factor for Tangential Velocity
c	Chord of Blade Section
c/r	Separation Point
n	Revolution per Seconds

n'	Empirical Value to Calculate the Velocity Gradient, typically 1
p	Point Location of the Mesh Node
q	Center of the Blade
r	Local Radius of the Blade Section
r'	Normalized Local Radius of the Blade Section
t	Time
u_r	Velocity in Radial Direction
u_t	Velocity in Tangential Velocity
n_ω	Rotating Axis of Blades
n_{t_x}	X Component of Tangential Velocity of the Blade Section
n_{t_y}	Y Component of Tangential Velocity of the Blade Section
n_{t_z}	Z Component of Tangential Velocity of the Blade Section
n_{ω_x}	X Component of Rotational Axis of the Blade
n_{ω_y}	Y Component of Rotational Axis of the Blade
n_{ω_z}	Z Component of Rotational Axis of the Blade
v	Velocity of Flow
v_a	Axial Velocity of Blade Section
v_t	Tangential Velocity of Blade Section
$v_{t_{total}}$	Total Rotational Velocity of the Blade Section
α	Angle of Attack at the Blade Section
$\alpha_{Cl=0}$	Angle of Attack where 0 Lift Coefficient Occurs
$\alpha_{Cl_{max}}$	Angle of Attack where Maximum Lift Coefficient Occurs
α_i	Induced Angle of Attack

α_{stall}	Stall Angle of Attack
ε	Solidity at the Blade Section
γ	The Ratio of Specific Heats
μ	Dynamic Viscosity of Flow
μ_{tot}^{*}	Total Dynamic Viscosity
ρ	Density of Freestream
θ	Pitch of the Blade Section
τ	Shear Stresses
ω	Rotational Velocity
φ	Domain Volume
φ_i	Cell Volume

CHAPTER 1

INTRODUCTION

Over the years, the simulation of rotating parts has been a topic of significant interest and research in the field of computational fluid dynamics (CFD). The accurate representation of rotating components, such as propellers, wind turbines, and axial turbines, is essential for optimizing their performance and understanding the flow phenomena associated with them. One of the key challenges in simulating rotating parts is the computational cost and time required to obtain reliable results. (Durasevic et al., 2022)

Simulating rotating parts with CFD is crucial for several reasons. Firstly, it enables engineers to optimize the design and performance of rotating components such as propellers (Lloyd et al., 2022), turbines (Yang et al., 2023), and fans (Ramirez et al., 2022). By accurately modeling the flow behavior and interactions around these rotating parts, CFD allows for the identification of design improvements that can enhance efficiency, increase power output, and reduce energy consumption. CFD simulations of rotating parts also play a significant role in understanding the complex flow phenomena associated with them. This includes the prediction of wake structures (Chen et al., 2023) and the assessment of dynamic loads (Maalouly et al., 2022). Such insights are vital for ensuring the structural integrity and operational safety of rotating machinery.

1.1 Problem Definition and Aim of the Research

Many tools and methods have been enhanced to help determine the results of problems related with rotating components using CFD. Each of these tools has its own strengths and weaknesses in terms of accuracy, computational requirements,

and complexity. With these tools readily available in the literature, researchers can develop customized tools that cater to their specific research goals and purposes.

One way to analyze the aerodynamics of rotating blades is by combining CFD and blade element theory (BET). This hybrid approach combines the power and accuracy of CFD equations with the simplicity and effectiveness of blade element theory. In the past, this hybrid tool has been implemented in various commercial and open-source software. For example, there was an implementation of an actuator disc model using BET theory in Stanford University Unstructured (SU2) software. However, this model has limitations in terms of operating conditions and specific purposes. These limitations include definition of a constant power and thrust coefficient distribution throughout the blade radius. In real scenario, thrust and power coefficients should be updated in each point according to the obtained flow variables in each iteration. However, the former actuator disc model failed to account for this update due to constant definition of thrust and power coefficients at all operating conditions. Therefore, there is a need for a new implementation of an actuator disc model in SU2 software using blade element theory.

Implementing a new model in SU2 software requires a good understanding of the software components. Although SU2 is designed to be object-oriented, which makes it relatively easier to implement a new model, it can still be challenging to understand the necessary modifications. Additionally, apart from the software complexity, a thorough validation process is necessary to ensure the model can be used in future studies. To achieve this, it is important to choose high-fidelity comparison cases and provide the new model with inputs of the highest possible fidelity.

This thesis aims to provide a detailed study on implementing the actuator disc model into SU2 software, as we call it AEDISC (Yenipazar et al., 2023) and validating its performance. The study includes a comprehensive almost step-by-step guide that outlines the methodologies for implementing the model.

1.2 Thesis Scope

Chapter 1 provides a concise overview of the requirements for implementing the hybrid methodology. It includes a brief introduction to CFD and SU2 software, highlighting the necessary steps for implementing this particular hybrid CFD-BET model. Additionally, Chapter 1 offers a summary of the subsequent chapters and provides a brief explanation of the topics covered in each chapter.

Chapter 2 delves into a comprehensive literature survey, focusing on various models that are employed to simulate rotating components. Each model is thoroughly discussed, and relevant references are provided for further exploration. This chapter also includes experimental studies that were performed to assess the performance of rotating components.

Chapter 3 serves as a platform for discussing the methodologies employed in this study. The chapter starts with a detailed information about the experimental case and data, which is later used for model validation in Chapter 4. This includes a comprehensive explanation of the model, as well as an overview of the operational conditions and geometrical properties of the experimental setup. It also encompasses a detailed exploration of the hybrid CFD-BET approach, along with another comparison methodologie such as the rotating frame. The chapter commences by providing an overview of the general equations within the SU2 software, specifically focusing on the rotating frame approach. It then proceeds to delve into the blade element theory. Within the methodology section, the code structure of SU2 is presented, along with a step-by-step guide on implementing the new model into the SU2 software. Additionally, the supporting data required for the model, including the 2D airfoil database, is thoroughly discussed within this chapter.

Chapter 4 serves as the platform for presenting the results of the study, focusing on comparisons between the developed hybrid model with experimental data and another methodology, namely the rotating frame approach. These comparisons are conducted across various operating conditions, considering multiple outputs of

these methodologies. The objective is to ensure the readiness and efficiency of the newly implemented model through rigorous comparisons and analyses. By examining different aspects and performance metrics, this chapter provides a comprehensive assessment of the implemented model and its viability for further applications.

Chapter 5 marks the conclusion of the study, wherein a comprehensive summary and synthesis of the methodology and results are presented for the readers. This chapter serves as a culmination of the entire study, offering a concise overview of the implemented methodologies and the obtained results. By bringing together all the key findings and insights, this section aims to provide a clear and cohesive understanding of the study's outcomes to the intended users or readers.

CHAPTER 2

LITERATURE REVIW

Several CFD software packages have been utilized in both industry and academia, offering the necessary capabilities to simulate rotating components. SU2 is a robust CFD software developed by researchers at Stanford University (SU2 Team, 2023). It is designed to handle unstructured grids, providing flexibility and versatility in solving complex fluid flow problems. With its node-based solver, SU2 offers a comprehensive range of capabilities for simulating various flow phenomena and optimizing engineering designs. (Palacios et al., 2013) The software provides several methodologies for accurately modeling rotating blades and predicting their behavior. This includes the steady-state rotating frame approach, the unsteady sliding mesh technique, and the actuator disc model using the blade element theory with limitations in it. Each method offers distinct advantages and can be applied to different scenarios.

In their study, Galimberti et al. (2023) addressed the issue of propeller noise, which is a significant concern in aerospace research. They focused on developing an efficient framework within SU2. To enhance computational efficiency and enable larger and faster simulations for propeller design and optimization, the researchers utilized the rotating frame approach rather than sliding mesh approach in the acoustic computation. This approach not only improved the studies efficiency but also facilitated propeller-related simulations in a sufficiently accurate manner.

Morellia et al. (2021) utilized the open-source SU2 code to conduct computational aerodynamic analyses of rotorcraft main rotor blades. They took advantage of the steady rotation characteristic exhibited by the flow around the main rotor in specific operational conditions such as hover where the flow is assumed to be parallel to the rotation of axis, by using rotating frame approach.

In their study, Morellia et al. (2021) further explored the capabilities of the SU2 code by incorporating a sliding mesh approach as well. This approach allowed them to simulate operating conditions in which unsteady effects play a significant role, such as forward flight.

Iannini (2022) conducted a study on the aerodynamic interactions between two tandem propellers in airplane mode flight condition using a multi-fidelity approach. The research incorporated experimental data, a mid-fidelity software and high-fidelity simulations in SU2, employing the sliding mesh approach. The investigation aimed to assess the performance losses of the rear propeller in the tandem configuration and understand its impact on eVTOL aircraft performance. The use of unsteady sliding mesh was necessary to accurately capture the dynamic behavior and interactions between the tandem propellers in the airplane mode flight condition.

A general actuator disc model that was based in the general momentum theory was implemented in SU2 by Saetta et al. (2020). The authors described the model and discussed its application with different test cases. The previous version of the model was available in SU2 up to release 7.0.6, but the new model introduced in this paper offers enhanced capabilities and improved functionality. It is applicable only to the inviscid compressible flow regime, meaning it does not consider viscous effects. Secondly, the model assumes a steady regime, neglecting unsteady effects. Lastly, it is designed for scenarios where the angle between the disc axis and the freestream velocity is negligible. While the model can simulate rotorcraft hovering (although not specifically tested), it is not suitable for helicopter rotors in forward flight, or aircraft with propellers at an angle of attack.

Besides all these high-fidelity CFD options there are also simpler approaches available for analyzing the performance of rotating components. One such approach is the blade element momentym theory. This theory, first introduced by William Froude in the late 19th century (Froude, 1878), was initially developed to

study the behavior of ship propellers. However, its applications have expanded to include the analysis of aircraft propellers and helicopter rotors.

Morgado et al. (2014) developed JBLADE, an open-source propeller design and analysis tool. The software utilizes an improved version of the blade element momentum theory, incorporating a new model for three-dimensional flow equilibrium. It also introduces a method for predicting the airfoil drag coefficient at a 90-degree angle of attack. The tool allows for the simulation and performance estimation of propellers under various operating conditions.

MacNeill et al. (2017) employed the blade element theory methodology with correction methodologies to accurately determine the power and thrust coefficients of propellers. Their study incorporated 3D scanning to capture airfoil sections at different angles of attack and Reynolds Numbers, while also considering 3D rotational effects such as stall delay. The extended blade element momentum theory method yielded improved modeling accuracy. The results showed a close agreement with experimental data, with power and thrust coefficients matching effectively. In both studies (Morgado et al., 2014 and MacNeill et al., 2017) the primary focus is on power and thrust coefficients, which are important performance indicators. However, the blade element momentum theory, despite its efficiency and timesaving benefits, has limitations when it comes to predicting the swirl and flow behavior behind the rotating components. (Ning et al., 2015) These limitations become particularly evident in industries such as aerospace, marine, and wind turbine applications, where accurate prediction of flow characteristics downstream of the rotating component is also crucial for optimal performance.

The limitations of the rotating frame and blade element momentum theory, as well as the computational expense associated with the sliding mesh approach, have highlighted the need for an alternative steady-state actuator disc model. To achieve this, the researchers adopt the blade element theory approach, which combines the advantages of CFD in terms of power and accuracy, with the efficiency and time-saving benefits of the blade element momentum theory. By employing the blade

element theory, theese studies seek to enhance the prediction of thrust and power coefficients, as well as the wake structures both in axial and cross flow conditions, which plays a crucial role in such as: understanding slipstream effects in aircraft and wake interactions. (Adjiri et al., 2022) The coupling of both methodology CFD and BET refers to the integration of these two approaches in the modeling process. In this context, the aerodynamic forces obtained by using BET, are incorporated as a source term in Navier-Stokes (Leray, 1934) equations. These forces are distributed across the volume elements, taking into account the blade geometry and aerodynamic profile data by BET. The local axial and tangential forces are calculated based on the velocity field obtained from the CFD solver at each iteration. In the simulation, the representation of rotating parts is achieved through the use of a virtual disc known as the actuator disc.

In their study, Balduzzi et al. (2018) present a hybrid BET-CFD model that combines the benefits of both approaches for analyzing wind turbine performance and wake structure. The authors validate the model that was implemented by incorporating user-defined functions into the ANSYS Fluent software and perform a sensitivity analysis to determine the optimal siting of a small wind turbine on the rooftop of a tall building in a densely built environment. A comparison with a full CFD calculation demonstrated the effectiveness of the hybrid BET-CFD approach proposed. Another study (Guo et al., 2015) was also performed to couple blade element momentum theory with the Reynolds Averaged Navier-Stokes equations (RANS) in computational fluid dynamics software ANSYS CFX to analyze flows in marine current turbines with reduced computational resources. It was found that the two-dimensional lift and drag coefficients had significant effects on the BET-CFD predictions. Overall, the study concluded that BET-CFD based on numerical hydrofoil data can accurately predict the thrust but generally overestimates the power. The authors suggested that improving the BET-CFD accuracy would require considering more reasonable two-dimensional predictions for hydrofoils and accounting for three-dimensional effects. When generating 2D airfoil database, it’s important to consider the effects of different flow conditions such as low Mach

number effects or low Reynolds number. It's important to use correct tools to analyze such points. Some previous works on symmetric airfoils at low Reynolds numbers has been performed in Aerospace Engineering Department of METU (Naeem et al., 2023; Kurtulus, 2022; Kurtulus 2021; Gunaydinoglu et al. 2020; Durmaz et al., 2013; Kurtulus et al., 2004; Kurtulus et al., 2005; Kurtulus et al., 2006a; Kurtulus et al., 2006b; Akay et al. 2007).

In addition to the requirement for a 2D database, the coupling of blade element momentum theory with a CFD approach necessitates further modifications to account for the complex 3D phenomena involved. Blade element momentum theory, which is primarily based on simplified 2D aerodynamic principles, may not fully capture the complex flow behaviors and 3D effects present in practical applications. As a result, additional refinements and adjustments are necessary to enhance the accuracy and reliability of the coupled BET-CFD approach. Rotational effects play a crucial role in rotating part performance, and are often neglected in BET models. This becomes particularly important at low advance ratios, emphasizing the need for a comprehensive evaluation of various methods to improve aerodynamic modeling in this regime. To address these challenges, MacNeill et al. (2017) extracted airfoil sections from the blades to create an aerodynamic database, covering a wide range of angles of attack and Reynolds Numbers. These databases are then modified to incorporate the effects of rotation, enabling a more accurate representation of propeller performance according to the comparisons.

Apart from the numerical studies, various experimental studies have also been carried out to achieve either more precise outcomes or to confirm the findings obtained from these numerical studies. For example, some experimental tests have been carried out around propellers and helicopter blades (Kaya et al.; 2016; Sahbaz et al. 2017).

Validation of numerical computations can be achieved through various methods. Among these, experimental results are considered the most reliable source of

validation data due to their ability to accurately reflect real-life scenarios. Comparing numerical results with experimental data provides a robust means of validation. Additionally, numerical results can also be compared with other numerical results, although this approach is not as preferable as comparing with experimental data. Nonetheless, such comparisons can still provide valuable insights for validation purposes.

For the validation of their new actuator disc model, an enhanced experimental study were conducted by Adjiri et al. (2022) at the Dynfluid Laboratory wind tunnel (ENSAM School Paris Tech). The study utilized Particle Image Velocimetry (PIV) measurements to explore the wake characteristics of a miniature two-bladed wind turbine. The analysis revealed a strong correlation between the numerical simulations and the experimental measurements obtained from the ENSAM wind tunnel.

The accuracy of the BET-CFD calculation was also evaluated by Guo et al. (2015) through the analysis of the performance and flow field characteristics of an isolated horizontal axis marine current turbine. The evaluation of the BET-CFD results incorporated the examination of the experimental and numerical lift and drag coefficients. Additional sources of turbulence were introduced in the solved flow field by Balduzzi et al. (2018) to adjust the standard CFD settings used in simulating urban flows for the accurate prediction of turbine performance using the CFD-BET model. The incorporation and calibration of these additional sources were conducted by comparing them to a full RANS with rotating frame calculation which are known as high fidelity solvers.

Morgado et al. (2014) developed a software called JBLADE, which is based on blade element momentum theory. For comparison, they utilized experimental tests from NACA Technical Report 530 by Gray (1941) titled "Wind-Tunnel Tests of Two Hamilton Standard Propellers Embodying Clark Y and NACA 16-Series Blade Sections," as well as NACA Technical Report 594 by Theodorsen et al. (1937) titled "Characteristics of Six Propellers Including the High-Speed Range.".

Despite the availability of essential information such as airfoil shape, twist, pitch, and chord in this experimental test, it was conducted a significant time ago. Morgado et al. (2014) acknowledged that the measurement method for pitch angles of these propeller sections was not clearly documented, necessitating the reliance on assumptions. Additionally, due to the limitations of the older experimental setup, there is a possibility of significant error margins. Consequently, these data were deemed suboptimal for our purposes.

The UIUC Propeller Data Site (Brandt et al., 2023) provide a collection of propeller experimental data obtained through wind tunnel studies. This website offers measurements for propellers utilized in small unmanned aerial vehicles (UAVs) and model aircraft. The findings from the wind tunnel experiments were found to closely match the measurements taken at Ohio State University (Deters et al., 2014) indicating a strong correlation between the results obtained from different sources. This site provides experimental results in thrust coefficients, power coefficients and efficiency of each propeller in different rotation rates of propeller, as well as the geometrical parameters of each propeller, except for the airfoil sections which is a significant lacking. The site also lacks results for propellers that are subjected to cross flows. That’s why we also needed to find a propeller study based on one of the data presented in this site, which also includes a scanning phase so we could obtain the airfoil sections.

In their study, MacNeill et al. (2017) employed 3D scanning techniques to acquire precise airfoil sections of some of propellers presented in UIUC database, constituting a propeller blade, enabling a methodical evaluation. This approach facilitated accurate measurements of propeller pitch, chord, and the aerodynamic shape at various radial positions. By segmenting the blade into 'slices' along its radius, multiple airfoils were cataloged and utilized as representations for each section of the propeller. The researchers determined that the scanned point cloud at each radial position could be matched with the most closely fitting NACA four- or five-digit airfoil section, and they presented these fitted airfoil sections in their study.

CHAPTER 3

METHODOLOGY

To successfully implement and validate the new enhanced actuator disc model AEDISC, it is important to have a clear understanding of several concepts. In this chapter, we delve into these concepts, providing detailed explanations and associated assumptions. Implementing the actuator disc model using the blade element momentum theory requires a solid grasp of the theory of CFD and BEM itself. Therefore, we offer a comprehensive explanation, complete with relevant equations and diagrams.

To ensure accurate validation of the model, a robust 2D airfoil database representing the aerodynamic characteristics of blade sections is essential. Consequently, we dedicated significant effort to acquiring this database and developed correction methods specifically tailored for rotating applications.

In addition to obtaining the necessary data, a thorough understanding of the SU2 software, which will be used for implementing the model, is crucial. SU2 is an open-source code that allows users to modify the underlying C++ code (ISO/IEC., 2020). and interact with it using Python wrappers. (Economon et al., 2016) However, comprehending the code structure can be challenging for researchers due to it's size. To address this, we provide a detailed description of the C++ files in the source code, illustrating how a new actuator disc model can be built from scratch.

By following this step-by-step approach and gaining a comprehensive understanding of the concepts, blade element momentum theory, the 2D airfoil database, and the SU2 software, we can successfully implement and validate the enhanced actuator disc model.

3.1 Definition of the Test Case

We conducted a thorough investigation to acquire a generic test model suitable for rotating applications. The requirements for this model included a precise definition of its 3D geometry, encompassing clear specifications for the span-wise chord distribution, twist distribution, and airfoil shapes throughout the blade. Additionally, we sought to obtain comprehensive data through further studies, including accurate results such as the thrust coefficient and power coefficient under various operating conditions.

Obtaining such a model proved to be a challenging task. While there are several experimental models available in the literature with corresponding experimental results, most of them lack the crucial presentation of one of the study's most significant parameters: the airfoil shapes throughout the blade. This absence is primarily due to the complexity of acquiring such information, which typically necessitates advanced measurement techniques like laser scanning.

The selection of an APC Thin Electric 19x12 propeller that’s side and front views are provided in Figure 3.1 and Figure 3.2 respectively, characterized by a 19-inch diameter and 12-pitch, was primarily driven by the propeller data's currency and its extensive use in various studies available on the UIUC Propeller Data Site (Brandt et al., 2023). These factors played a significant role in validating our choice. Furthermore, the airfoil sections utilized in this thesis were previously provided by MacNeill et al. (2017) making them widely employed in our research.

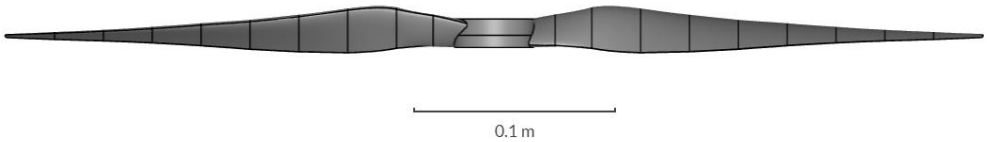

Figure 3.1. Side view of APC Thin Electric 19x12 Propeller

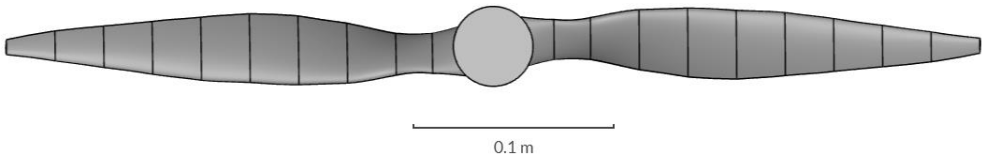

Figure 3.2. Front view of APC Thin Electric 19x12 Propeller

Geometrical data for each section is available in the propeller data site. Chord and twist distribution are presented with respect to local radius, and the data for APC 19x12 Propeller are presented in Figure 3.3.

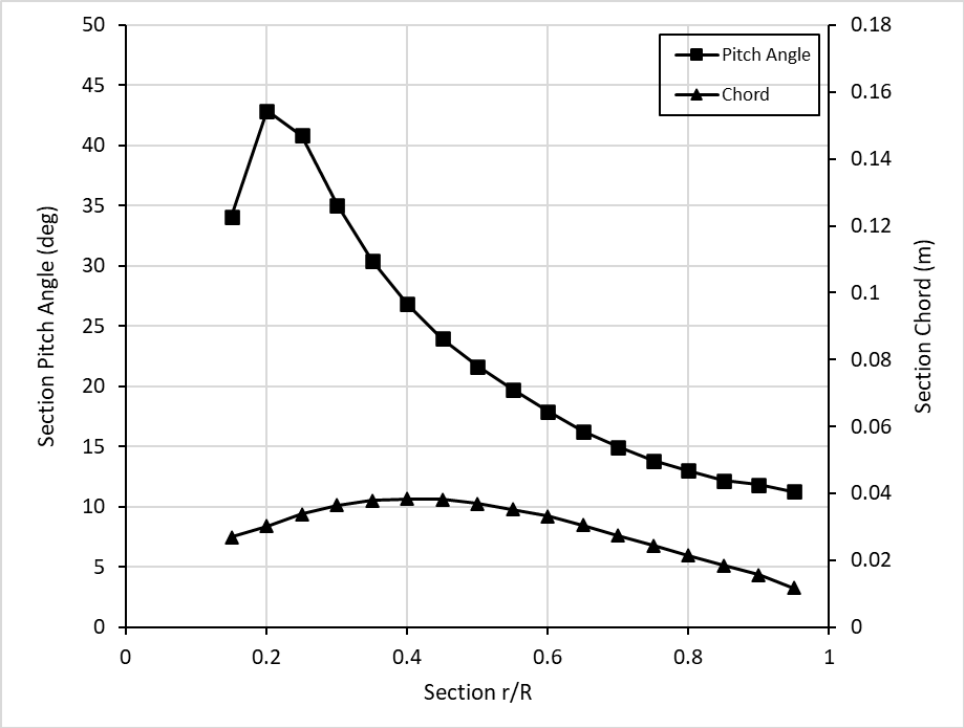

Figure 3.3. Local twist and chord distribution of APC 19x12 Propeller

We mentioned that MacNeill et al. (2017) obtained airfoil sections by using a 3D scanning technique, then each point data is fitted into a NACA profile airfoil. For the APC 19x12 propeller, distribution of the NACA airfoil sections is presented in Table 3.1.

Table 3.1 Distribution of the airfoil sections throughout the APC 19x12 Propeller

Local Radius (r/R)	*Airfoil Section*
0.2	NACA 5524
0.3	NACA 4417
0.4	NACA 4515
0.5	NACA 4513
0.6	NACA 4512
0.7	NACA 4411
0.8	NACA 4410
0.9	NACA 4309
1.0	NACA 4309

Having airfoil distribution data throughout the blades is significantly important, as well as to have chord and twist distribution. Both studies performed in this study, rotating frame and BET-CFD, require such information. BET-CFD method requires 2D aerodynamics of these sections, where the rotating frame approach requires a 3D model. Geometrical properties and airfoil section data are implemented in the SU2 code by adding a separate data file, which will be discussed in upcoming chapters.

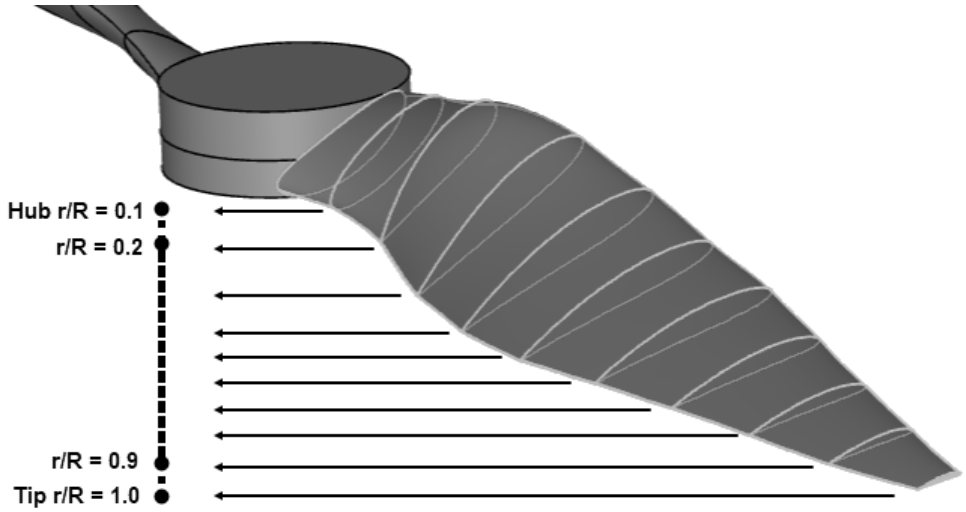

Figure 3.4. 3D model of APC 19x12 Propeller and the location of airfoil sections

A 3D model of the APC 19x12 Propeller was necessary to perform 3D CFD simulations with the rotating frame approach. The 3D model, as can be seen in Figure 3.4, based on the geometrical and airfoil data, was prepared on NX software which is a commercial CAD design tool widely used in the industry.

3.2 CFD Equations in SU2 and Rotating Frame Methodology

Implementation of the BET to SU2 software requires modifications in several parts of the source code. In order to proceed, an understanding of the certain equations solved within SU2 solver was necessary. SU2 is a multiphysics solver that allows users to perform fluid flow analysis, thermal analysis, thermal and flow coupled analysis, structural analysis, and structural and flow coupled analysis. The solver is an open-source one, and it's mainly developed by the Stanford University. Different turbulence models are available within the solver, and k-w SST turbulence model is used throughout this research.

The system of partial differential equations (PDEs) arising from the physical modeling of the problem should exhibit structure provided in Equation 3.1.

$$\partial_t U + \nabla\overrightarrow{F^c} - \nabla\overrightarrow{F^v} = Q \; for \; t > 0 \tag{3.1}$$

In this representation, $\partial_t U$ will represent the time-dependency of the flow variables (mass, momentum, energy), $\overrightarrow{F^c}$ represents the convective fluxed of flow variables, $\overrightarrow{F^v}$ are the diffusive viscous fluxes, and Q represents the source term. The source term here could be used to represent any additional source or sinks in the domain such as velocity sources, power and heat sources, heat sinks, etc.

Following the assumption that the flow is governed by the compressible Navier-Stokes equations, where the conservative variables can be expressed in the form:

$$U = (\rho, \rho v_1, \rho v_2, \rho v_3, \rho E)^T \tag{3.2}$$

Where, ρ is expressed as density, E is the total energy/mass, and $\vec{v} = (v_1, v_2, v_3)$ is the flow velocity in cartesian coordinate system. In this particular case, the convective and viscous fluxed can be expressed as in Equation 3.3 and Equation 3.4 respectively.

$$\overrightarrow{F_i^c} = \begin{pmatrix} \rho v_i \\ \rho v_i v_1 + P \\ \rho v_i v_2 + P \\ \rho v_i v_2 + P \\ \rho v_i H \end{pmatrix}, i = 1,2,3 \tag{3.3}$$

$$\overrightarrow{F_i^v} = \begin{pmatrix} . \\ \tau_{i1} \\ \tau_{i2} \\ \tau_{i3} \\ v_j \tau_{ij} + \mu_{tot}^* C_p \partial_i T \end{pmatrix}, i = 1,2,3 \tag{3.4}$$

In Equation 3.3 static pressure is expressed with P, and H is the enthalpy of the fluid. In Equation 3.4, τ_{ij} corresponds to viscous stresses, C_p is the specific heat of the fluid, T is the temperature, and μ_{tot}^* is the combination of dynamic viscosity that satisfies the Sutherland's Law and turbulent viscosity which can be computed by using turbulence models.

In this study, the new model is implemented by using the compressible formulation so that the density variations can be accounted as well. A significant portion the propeller applications are known to be operating in compressible regime due to high speeds near the blade tips, hence this was a necessity, rather than a choice. Most of the modifications in the code was made by referring to the existing rotating frame approach that already exists in the software itself.

Implementation of a new model in SU2 such as rotating frame approach, is utilized by modifications in the convective and source terms in the compressible formulation. (Palacios et al., 2012) While using the rotating frame approach, a transformation into a reference frame is necessary which will be rotating with a rotational velocity $\vec{\omega} = (\omega_1, \omega_2, \omega_3)$. A position vector $\vec{r}$ is defined that represents the vector between the center of rotation, and any point in the domain, and the velocity due to rotation in cartesian coordinates, $\overrightarrow{u_r}$ is computed as the cross product of rotational velocity and the position vector. Convective fluxes and source terms in order to achieve rotating frame approach is modified as shown in Equation 3.5a and 3.5b respectively.

$$\overrightarrow{F^c} = \begin{pmatrix} \rho(\vec{v} - \overrightarrow{u_r}) \\ \rho\vec{v}\,x\,(\vec{v} - \overrightarrow{u_r}) + P \\ \rho H(\vec{v} - \overrightarrow{u_r}) + P\overrightarrow{u_r} \end{pmatrix} \tag{3.5a}$$

$$Q = \begin{pmatrix} 0 \\ -\rho(\vec{\omega}\,x\,\vec{v}) \\ 0 \end{pmatrix} \tag{3.5b}$$

In rotating frame approach, modifications are needed in the convective fluxes to account for the rotation of the solution, and source terms are necessary to include the rotational velocities within the domain. It is important to note that no extra terms for mass or energy sources are required in the rotating frame, assuming that there is no additional mass or temperature changes caused by rotation. (Palacios et al., 2013)

In the BET and CFD coupling methodology, there is no requirement for modifications within the convective flux terms since our objective is to capture the

rotational effects through blade forces rather than explicitly representing the rotation itself. The focus is on implementing the resultant forces obtained from each section using the Q term. Similar to the rotating frame approach, our study assumes the absence of additional mass or energy sources.

The implementation of the new enhanced actuator disc model in SU2 is being considered as an alternative to other approaches like the steady-state rotating frame method and the transient sliding mesh method. Another validation case was required to compare it with the new BET-CFD model, considering errors in the experimental setup and the discrepancies that may arise between numerical methods and experimental data. The steady-state rotating frame method was chosen as the second validation case due to its computational efficiency. Additionally, the availability of propeller data on the propeller site only for propellers experiencing axial flows makes the steady-state rotating frame approach a suitable candidate for validation.

In SU2, the rotating frame method is utilized to simulate scenarios involving rotating components, such as propellers or turbines. This method enables the incorporation of the rotational motion by transforming the governing equations into a reference frame that rotates at the same angular velocity as the component. By doing so, the equations of motion can be expressed in a frame where the rotating component appears stationary. This transformation involves introducing additional terms in the equations. (Vijayanandha et al., 2022)

In order to perform the 3D CFD analysis with rotating frame approach, 3D model obtained from the experimental validations case is used. A tetrahedral based mesh with prism layers is generated in Pointwise software for accurate computations. RANS equations with k-ω SST (Shear Stress Transport) turbulence model are used to capture the wake properties of each blade, and to assess the correct wall treatment. Y+ value is ensured to be below one. A comprehensive mesh independency study is performed in order to avoid numerical deviations as much as

possible. The change in thrust and power coefficients with respect to mesh size is presented in Figure 3.5a and Figure 3.5b respectively.

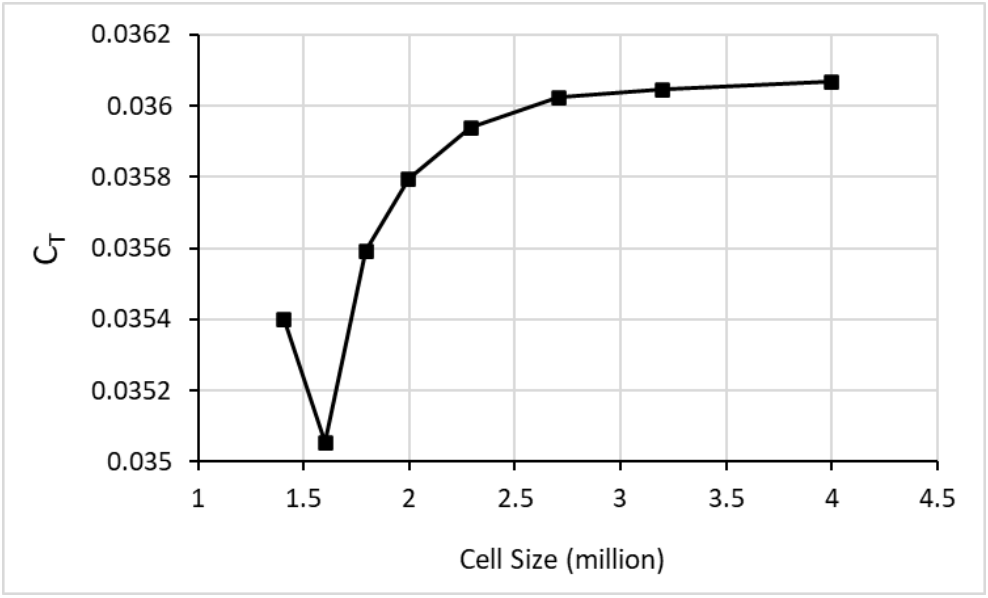

(a) Thrust coefficient convergence

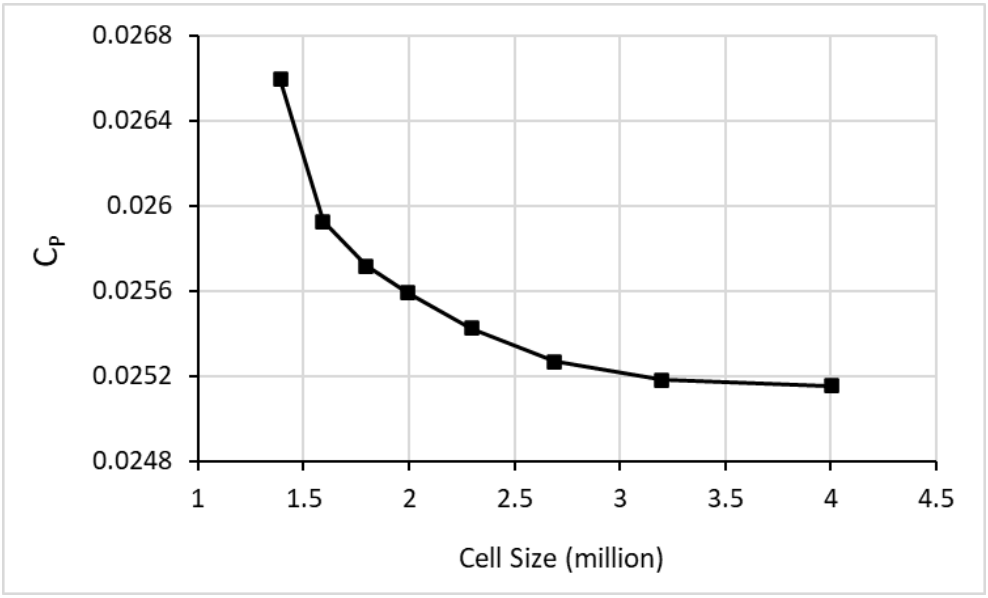

(b) Power coefficient convergence

Figure 3.5. Mesh independency study for steady-state rotating frame approach with thrust and power coefficients with respect to cell count.

The study on mesh independence involved augmenting the number of surface triangles on the propeller blades as can be seen in Figure 3.6a and Figure 3.6b. In exchange, the volume mesh density is also increased due to size of the initial volume elements groving from the surface. As the density of the surface mesh increased, a converging trend was observed for both coefficients. The thrust coefficient displayed a logarithmic increase and reached a stabilized value, while the power coefficient exhibited a logarithmic decrease and also achieved a stable value. These findings indicate that the initial coarse mesh configurations led to stronger blade separations than anticipated. This proves the importance of refining the mesh to accurately capture the flow behavior around the propeller blades.

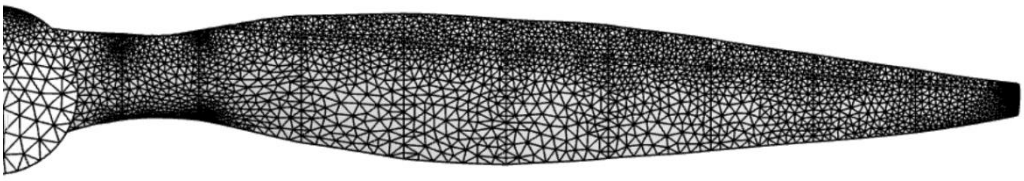

(a) Surface mesh representation of the coarse grid with total number of cells = 1.8 million

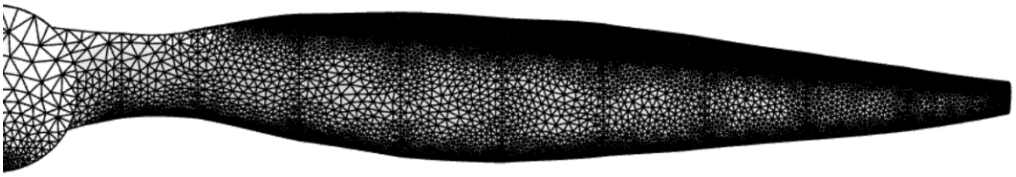

(b) Surface mesh representation of the coarse grid with total number of cells = 4.0 million

Figure 3.6. Surface triangulation in 2 different configurations for the mesh independency study

Mesh independency study was performed in 3000 RPM of the propeller with a 11.99 m/s freestream velocity in axial direction, that corresponds to an advance ratio of 0.5. The advance ratio is defined as the ratio of freestream velocity and product of RPS and diameter of the propeller as given in Equation 3.6.

$$J = \frac{V_\infty}{nD} \tag{3.6}$$

In the context of the k-ω SST turbulence model, maintaining a y+ value below 1 is still relevant for accurate predictions near the wall. The k-ω SST model (Menter, 1994) is a two-equation turbulence model that combines elements of the k-ε (Jones, 1972) and k-ω models (Wilcox, 1988) to provide improved accuracy in a wide range of flow regimes. By giving appropriate inputs, y+ value for this study maintaned below one which can be seen in Figure 3.7. It improves boundary layer resolution, and aids in accurate modeling of laminar-to-turbulent transition as well, which is a significantly important phenomena in low Reynolds Number flows.

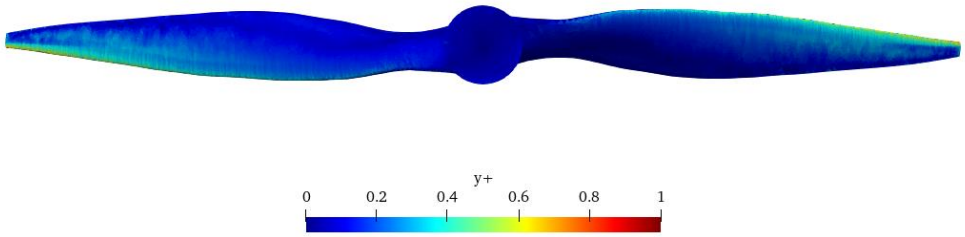

Figure 3.7. y+ values presented on the blades in 3000 RPM and 0.5 advance ratio.

In rotating frame applications, it is important to consider the velocity difference along the propeller span when generating the first prism layers on the surface. The propeller tips experience higher velocities due to the rotational speed, while the velocities near the hub are lower. To account for this velocity variation, thicker first prism layers can be generated near the hub, where the velocities are lower. Conversely, thinner first prism layers are typically generated near the propeller tips, where the velocities are higher. By adjusting the thickness of the first prism layers

based on the velocity difference, the mesh resolution can be optimized for accurate predictions of the velocity profiles and boundary layer behavior throughout the rotating propeller.

Once a final configuration for the mesh (3.2 million cells) and simulation setup is decided where the relative error becomes 0.06% in thrust, and 0.12% in power, the optimized configuration is used to perform rotating frame CFD analysis in several other advance ratios with two different RPM value for an accurate comparison. Advance ratios used in these simulations are presented in Table 3.2.

Table 3.2 Analysis points that are collected as a validation data and corresponding advance ratio and RPM values of the propeller.

Analysis ID	*Advance ratio*	*RPM*
1	0.149	3000 and 2500
2	0.280	3000 and 2500
3	0.406	3000 and 2500
4	0.500	3000 and 2500
5	0.601	3000 and 2500
6	0.706	3000 and 2500
7	0.763	3000 and 2500

By keeping the rotating frame rate constant in SU2 configuration file (Palacios et al., 2013), only the freestream velocity is changed to achieve the desired advance ratios. 2000 iterations are performed to ensure the force and moment values are reaching a converged state. Obtained force and moment coefficients are non-dimensionalized into thrust and power coefficients by following relations provided in Equation 3.7 and Equation 3.8 respectively.

$$C_T = \frac{T}{\rho n^2 D^4} \tag{3.7}$$

$$C_P = \frac{Q\omega}{\rho n^3 D^5} \tag{3.8}$$

In Equation 3.7 and Equation 3.8, T corresponds to thrust force in axial direction (N), $Q\omega$ is the product of moment around the rotation axis (N.m) and rotational rate (rad/s), and ρ is the density of the freestream flow. Resultant forces and moments are gathered manually, while the post-processing is performed in an open-source post-processing tool called Paraview. Paraview is an open-source post-processing tool commonly used in scientific visualization to analyze and visualize data from computational simulations. It provides a user-friendly interface and a wide range of features for exploring and interpreting simulation results, including the visualization of 2D and 3D data, the creation of animations, and the extraction of meaningful insights from the data. (Ayachit et al., 2015)

The aerodynamic coefficient values, as well as post-processing results for the steady-state rotating frame analysis are used to validate the newly implemented BET-CFD code, and are provided in results and discussion section.

3.3 Standard Blade Element Momentum Theory

The Blade Element Momentum method combines the momentum theory (MT) and the blade element theory (BET). It is a computational algorithm used to determine how well a rotor performs under specific conditions, such as wind speed, rotation speed and pitch angle. (Branlard, 2017)

The original BEM algorithm, described by Glauert (1934), assumes a rotor with an infinite number of blades operating in steady and uniform wind conditions. However, to make the algorithm more accurate and flexible, additional modifications are often made to account for real-world conditions. These adjustments help improve the predictions made by the BEM method.

In the blade element theory, the blade is divided into sections, and each section is assumed to have its own independent aerodynamic properties, and these properties

in each section is not influenced by other sections. To determine the behavior of each section, a process of iteration is used, combining the blade element theory with the momentum theory. This process calculates the induced velocities in the normal and tangential directions of the blade and continues until each section reaches a state of convergence. To visually represent the combination of the blade element and momentum theories, a triangle is often used around one of the lifting sections, as shown in Figure 3.8. It's important to note that this representation specifically applies to propeller applications, and the diagram may look slightly different in the context of wind turbine applications.In propeller applications, where power is input into the fluid, the normal velocity increases compared to the freestream velocity, while the tangential velocity decreases. However, in wind turbine applications, where power is extracted from the fluid by the rotating part, the opposite behavior is observed.

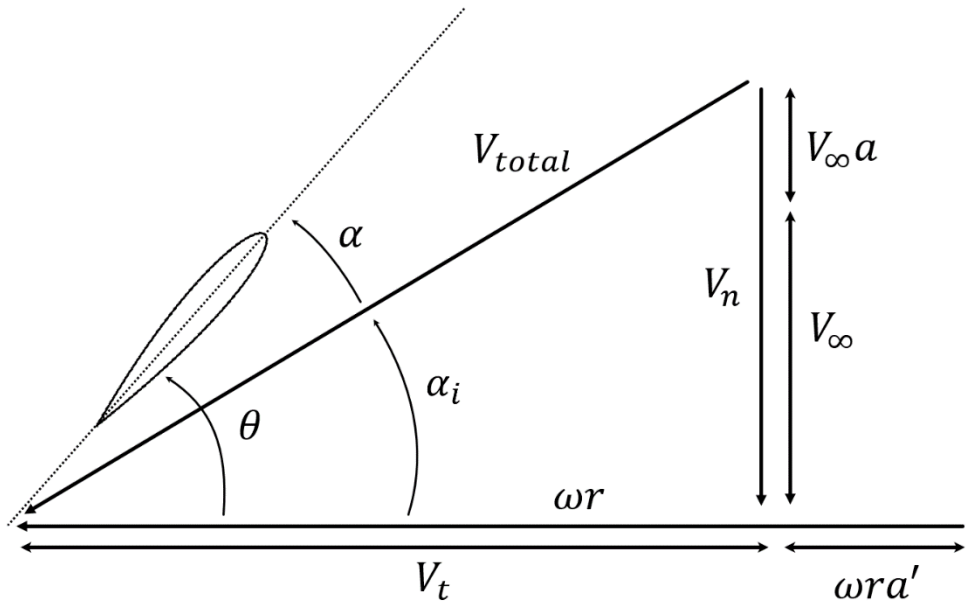

Figure 3.8. Representation of the blade element momentum theory triangle in propeller applications

Two induction factors a and a' are introduced in order to perform the iterative process, and in propeller applications they are assumed to be related by Equation 3.9 and 3.10 to normal and tangential components of the resultant velocity near the lifting section.

$$V_n = V_\infty(1 + a) \tag{3.9}$$

$$V_t = \omega r(1 - a') \tag{3.10}$$

Where V_n is the resultant normal component of the velocity near the lifting section, V_∞ is the freestream velocity, V_t is the resultant tangential component of the velocity near the lifting section, ω is the rotational velocity of the blades and r is the local radius of the lifting section. Equations 3.1 and 3.2 would be the first equations to be solved in blade element momentum theory, so that means we would need to assume initial values for the induction factors a and a'.

Based on the computed normal and tangential components of the velocity, and induced flow angle, α_i, is computed by using the relationship in Equation 3.11 and the triangle in Figure 3.8.

$$\emptyset = \arctan\left(\frac{V_n}{V_t}\right) \tag{3.11}$$

The total velocity, V_{total}, experienced by the blade section can be also calculated by using the Equation 3.12 which is one of the basic trigonometric relations.

$$V_{total} = \sqrt{V_n^2 + V_t^2} \tag{3.12}$$

Induced flow angle essentially means the effective angle of attack experienced by the blade sections will be smaller than sections pitch value. In this case the effective angle of attack can be computed based on the induced flow angle as presented in Equation 3.13.

$$\alpha = \theta - \alpha_i \tag{3.13}$$

In Equation 3.13., effective angle of attack is represented by α, where the pitch angle of the blade section is represented as θ. Please note that the pitch value in

reality corresponds to collective pitch angle of the blade, plus the twist angle of the blade section. In literature, there are different conventions for the pitch and twist angles, however in this study θ is assumed to be the ultimate blade section angle that accounts for both propeller collective pitch angle and twist angle of the blade sections.

Once the effective angle of attack and total velocity values are obtained, resultant lift and drag coefficients of the blade section can be calculated based on look-up tables, in other words airfoil database as shown in Equation 3.14 and Equation 3.15.

$$C_l = C_l(V_{total}, \alpha) \tag{3.14}$$

$$C_d = C_d(V_{total}, \alpha) \tag{3.15}$$

In the standard blade element momentum theory, the lift and drag coefficients are typically considered as functions of velocity and effective angle of attack. The effects of viscosity and compressibility are not explicitly accounted for in this simplified approach. However, in more advanced studies, like BET-CFD coupling, additional dependencies can be incorporated to capture the effects of viscosity through the Reynolds Number (Reynolds, 1883) or the effects of compressibility using the Mach number (Mach, 1871). In the subsequent sections, a similar workflow was followed to obtain more precise airfoil data. This involved considering these extended dependencies to enhance the accuracy of the lift and drag coefficients, taking into account factors such as viscosity and compressibility.

Obtained lift and drag coefficients can be projected into normal and tangential directions by using the induced flow angle as can be seen in Equation 3.16 and Equation 3.17.

$$C_{normal} = C_l cos\alpha_i + C_d sin\alpha_i \tag{3.16}$$

$$C_{tangent} = C_l sin\alpha_i - C_d cos\alpha_i \tag{3.17}$$

Normal and tangential coefficients then can be transformed into local thrust and power coefficients of each section by using Equation 3.18 and Equation 3.19.

$$C_{thrust} = \frac{V_n^2+V_t^2}{V_{total}^2} \varepsilon C_{normal} \tag{3.18}$$

$$C_{power} = \frac{V_n^2+V_t^2}{V_{total}^2} \varepsilon C_{tangent} \tag{3.19}$$

In Equation 3.18 C_{thrust} corresponds to local thrust coefficient of the blade section, where in Equation 3.19 C_{power} corresponds to local power coefficient of the blade section. ε is known as the solidity of the blade, and it can be calculated by using the relation in Equation 3.20.

$$\varepsilon = \frac{number\ of\ blades\ x\ section\ chord}{2\pi r} \tag{3.20}$$

Computation of local thrust and power coefficients, at this stage, are in fact sufficient to calculate the total thrust and power coefficient of the blade by integrating local variables. However, one should note that the BEM method is an iterative process, hence the iterations should be continued until induction factors a and a' reached a convergence. As the local thrust and power coefficients are calculated, these induction factors can be updated by using Equation 3.21 and Equation 3.22.

$$a = \frac{1}{\frac{4\sin^2\alpha_i}{\varepsilon C_{normal}} + 1} \tag{3.21}$$

$$a' = \frac{1}{\frac{4sin\alpha_i cos\alpha_i}{\varepsilon C_{tangent}} - 1} \tag{3.22}$$

Equations 3.21 and 3.22 represent a commonly used method in the literature to calculate the induction factors using the momentum theory. This approach, as discussed by Hansen (2008) and Bak (2010), incorporates the consideration of drag coefficients as well in the computation of the induction factors.

By incorporating the updated induction factors, it becomes possible to revisit Equation 3.9 and Equation 3.10, enabling the iteration process to be performed once more. Once the induction factors reach a state of convergence, the global

thrust and power coefficients of the rotating component can be determined by integrating the local variables across the blade sections. Figure 3.9 depicts a comprehensive schematic illustrating the entire coupling process of the blade element and momentum theories as described.

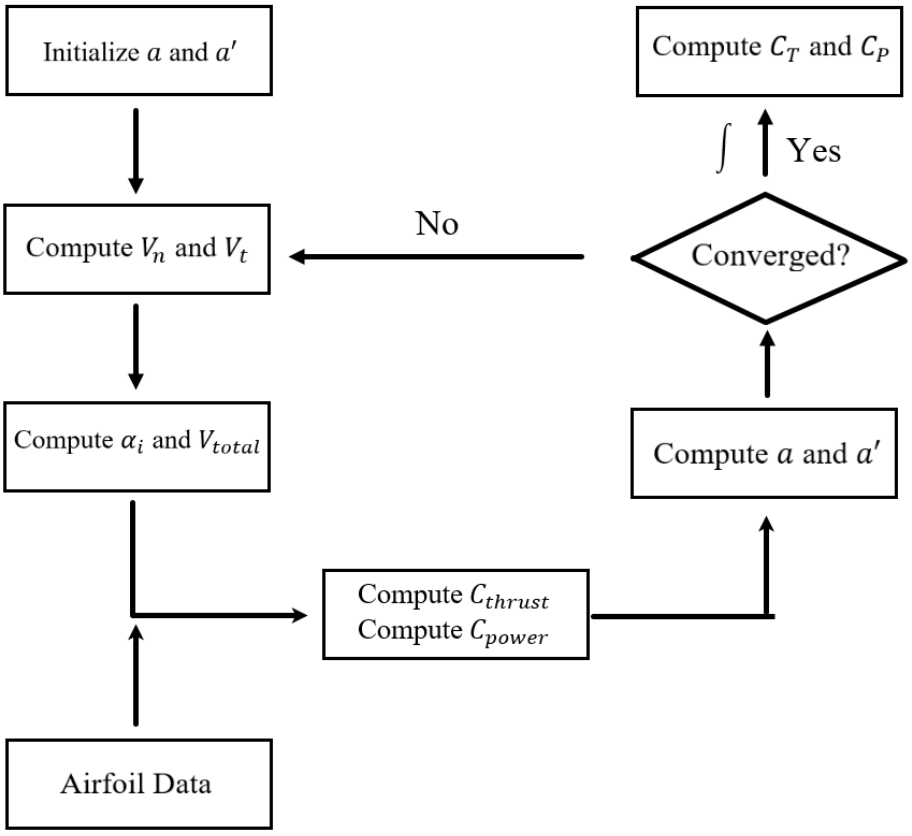

Figure 3.9. Representation of the coupling of Blade Element and Momentum Theories

The schematic representation of the iteration process may vary slightly when implementing the model in the SU2 software. In the next case, the induced velocities are calculated using the RANS equations, eliminating the need for the momentum theory. In standard BEM, the convergency is checked by introducing an error value between the current and previous iteration on computed thrust and

power coefficients. In the BET-CFD methodology, the convergency is checked by the CFD residuals for pressure, velocity, temperature, etc. The primary implementation methodology in this study, as it's clear by the name "BET-CFD," primarily involves the coupling between the blade element theory and CFD, with the blade element theory playing a crucial role. Prior to implementing the model, it is essential to acquire precise airfoil data, as depicted in Figure 3.9, which is crucial for the entirety of the iteration process. The subsequent section will delve into this topic in detail, as well as the correction methodologies to be applied.

3.4 2D Aerodynamic Database and 3D corrections

The accuracy of airfoil data holds utmost significance when employing standard blade element momentum theory. This accuracy directly impacts the derived thrust and power coefficients, subsequently affecting the calculated induced factors. It is crucial to represent the blade sections accurately as any inaccuracies can disrupt the entire iteration process within the blade element momentum theory. (Hansen et al., 2006) The same principle applies to BET-CFD coupling methods. Although induction factors are not computed in BET-CFD methods, the airfoil data still exerts a direct influence on the resultant forces acting on the blade, consequently influencing the magnitude of the momentum sources as a result. In addition to the importance of accuracy in numerical calculations, it is essential to consider the incorporation of 3D effects into the airfoil database to achieve more precise solutions. (Yang et al., 2014) Recognizing this necessity, we outline a comprehensive workflow in this section, aiming to establish a 2D airfoil database that incorporates both CFD computations and 3D correction methodologies. By integrating these factors, we can enhance the accuracy and reliability of the obtained results.

3.4.1 CFD Computations of 2D Airfoils

To streamline the process, we utilized the open-source SU2 software for conducting CFD calculations on 2D airfoil sections. The airfoil sections for the test blade were already specified in Table 3.1. For representational purposes, airfoil sections at three distinct positions on the blade are depicted in Figure 3.10.

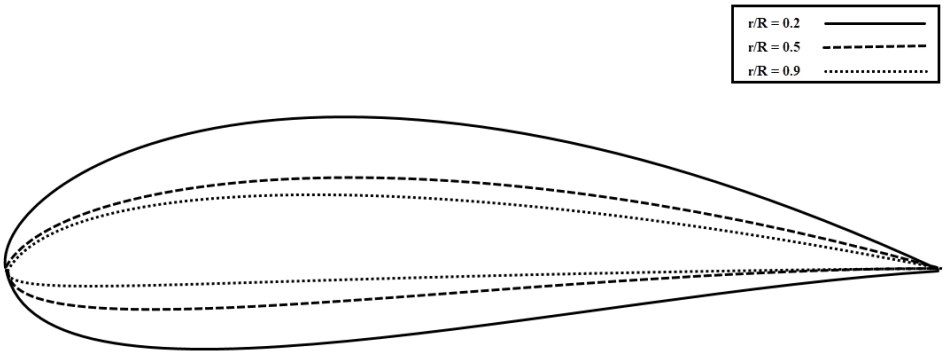

Figure 3.10. Airfoil sections through blade in three different blade radius location

Before we dive into the details of obtaining the aerodynamic database, we needed to conduct a study to ensure that our mesh strikes the right balance between accuracy and efficiency. Since we require high accuracy, we need a large number of analysis points which may consume significant resources, so a prior study on mesh independence was necessary here as well. To do this, we created five different mesh configurations and analyzed how the lift and drag coefficients change as we refine the mesh. We weren't concerned about the moment coefficient because we're not focusing on the twisting forces of the blade, which are more relevant to structural considerations. For each mesh configuration, we used a specific type of mesh called a Structured O-Grid, as shown in Figure 3.11a. We gradually increased the number of elements along the edges of the airfoil, as shown in Figure 3.11b, until we observed that the aerodynamic coefficients reached a stable and consistent value. These analyses were conducted at a freestream velocity

of 36 m/s, with a fixed angle of attack set to 5 degrees. First height of the initial cell is arranged such that the resultant y+ value is below 1.

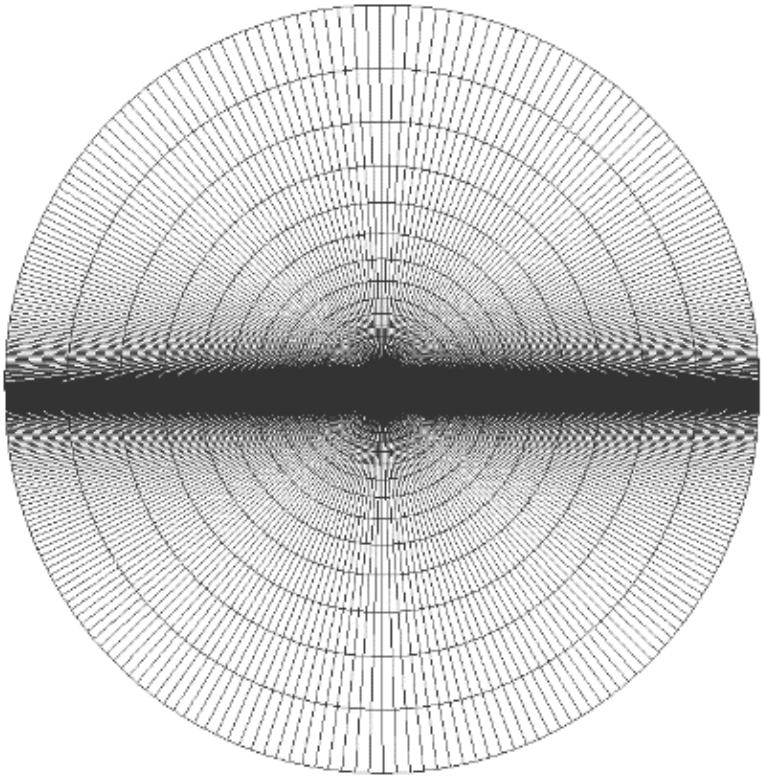

a) O-Grid structures mesh domain

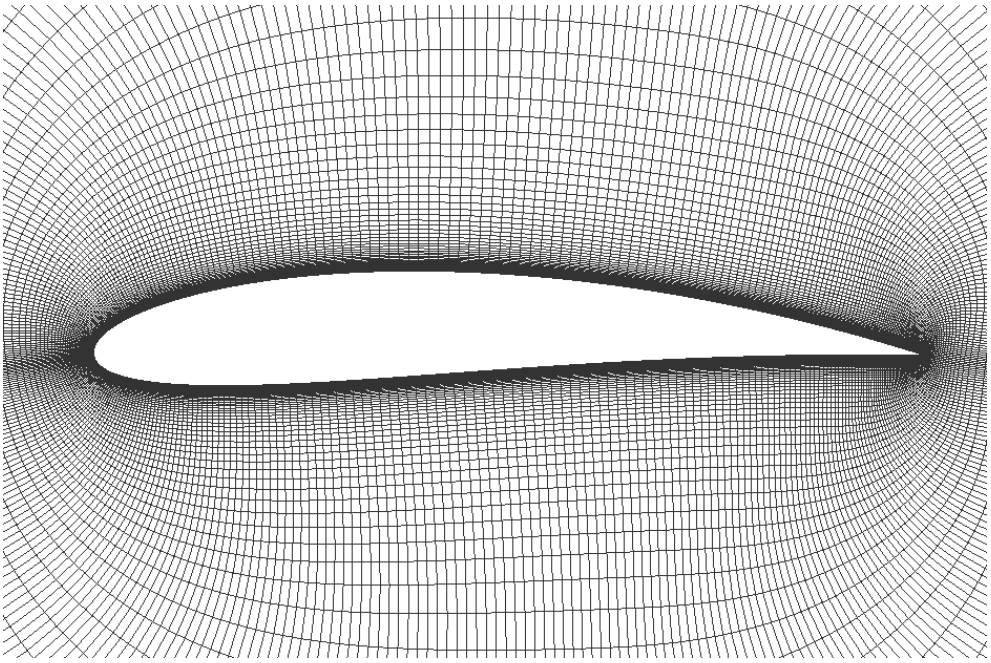

b) Structured elements near the airfoil

Figure 3.11. Computed global domain mesh (a) and the mesh around the airfoil (b) NACA 4513 which corresponds to r/R = 0.5

When conducting a study to determine the optimal mesh size, it is crucial to ensure that we have enough detail near the front and back edges of the airfoil. If we don't pay attention to this, we might end up comparing different setups that aren't really comparable. Instead, we should focus on the overall number of points on both the upper and lower surfaces of the airfoil. To create the different meshes, we used the Pointwise software and a special tool called normal extrusion. This tool helped us generate the meshes we needed by extending the points in a specific direction.

We looked at the convergence of two coefficients: lift and drag. In Figure 3.12a, we can see how the lift coefficient converges for the specific blade section we're studying. In Figure 3.12b, we have the convergence of the lift and drag coefficients. When we look at the results, we can clearly see that the lift coefficient increases and then levels off as we add more cells to the mesh. On the other hand, the drag coefficient decreases and then stabilizes as we increase the number of cells. Based on these observations, a mesh configuration with 49,000 elements has

been chosen where the relative error becomes 0.07% in lift coefficient, and 0.25% in drag coefficient.

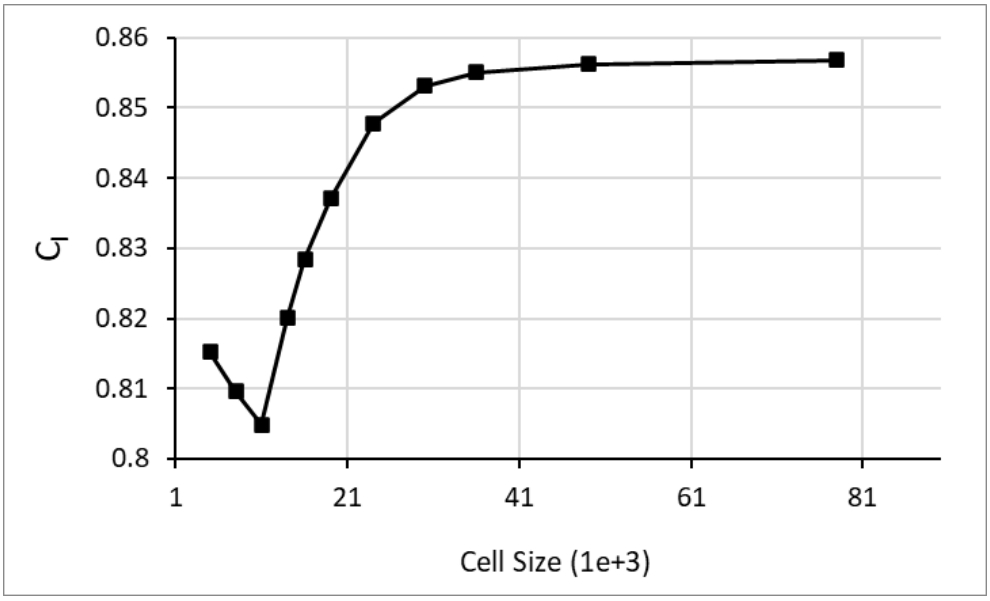

(a) Convergence of lift coefficient

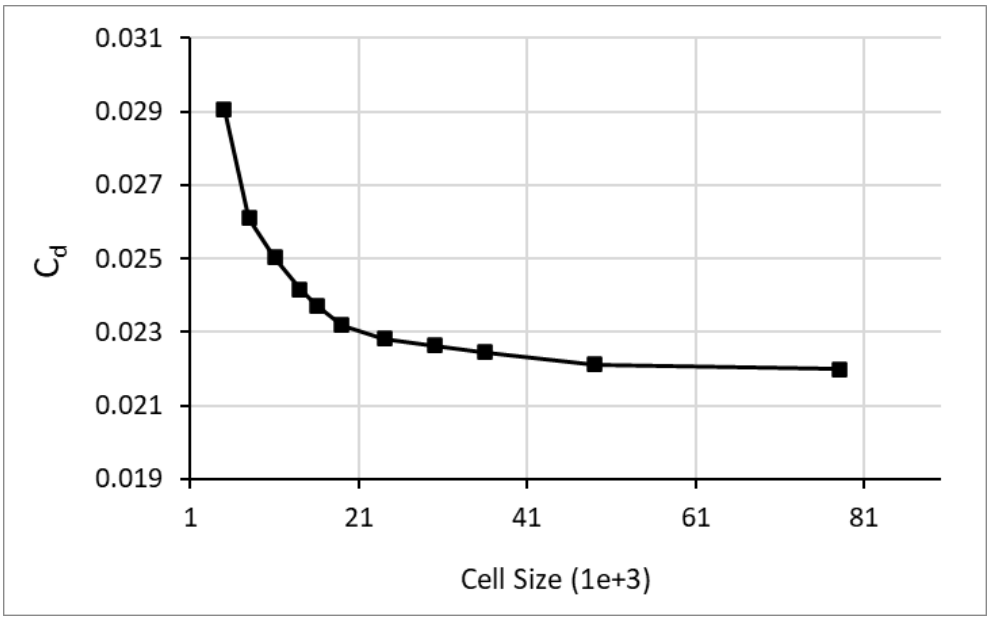

(b) Convergence of drag coefficient

Figure 3.12. Convergence of lift and drag coefficients for the 2D airfoil section with respect to cell size.

Once we have decided on the mesh configuration, the next step is to determine the analysis points for creating the airfoil database. In the standard blade element momentum theory approach, the lift and drag coefficients depend mainly on the angle of attack and velocity, as these are the variables obtained during the iteration process. However, when performing a BET-CFD coupled study, we can also consider the effects of compressibility and viscosity by incorporating density and velocity information. To ensure accurate validation, it is important to account for all parameters that influence the lift and drag coefficients.

To identify the parameters that have significant effects on the flow coefficients, three sweep study was conducted. The sweep study was conducted specifically at the middle section of the blade, which corresponds to the NACA 4513 airfoil. This study involved performing CFD analysis on the selected airfoil section while changing one parameter of interest at a time, while keeping the other two parameters constant. By doing this, we were able to observe the impact of each parameter, which are Mach Number, Reynolds Number, and Angle of Attack, on the flow coefficients and establish certain computing points that help finalize the selection of airfoil analysis data points. Computing points are going to be the analysis points, where the further CFD computations will be performed to generate the airfoil database.

3.4.1.1 Mach Number Computing Points

During the Mach and Reynolds Number sweep studies, it was important to maintain one parameter constant. Therefore, in each sweep point, the density was adjusted to ensure this consistency. In Figure 3.13, the change of flow coefficients with respect to different Mach numbers is shown. In the Mach number sweep study, the Reynolds Number is kept at 200,000 while the angle of attack is set to 4 degrees. The interval of Mach number is obtained by considering the advance ratio of the propeller setup in experiments, which determines the velocity distribution throughout the blade.

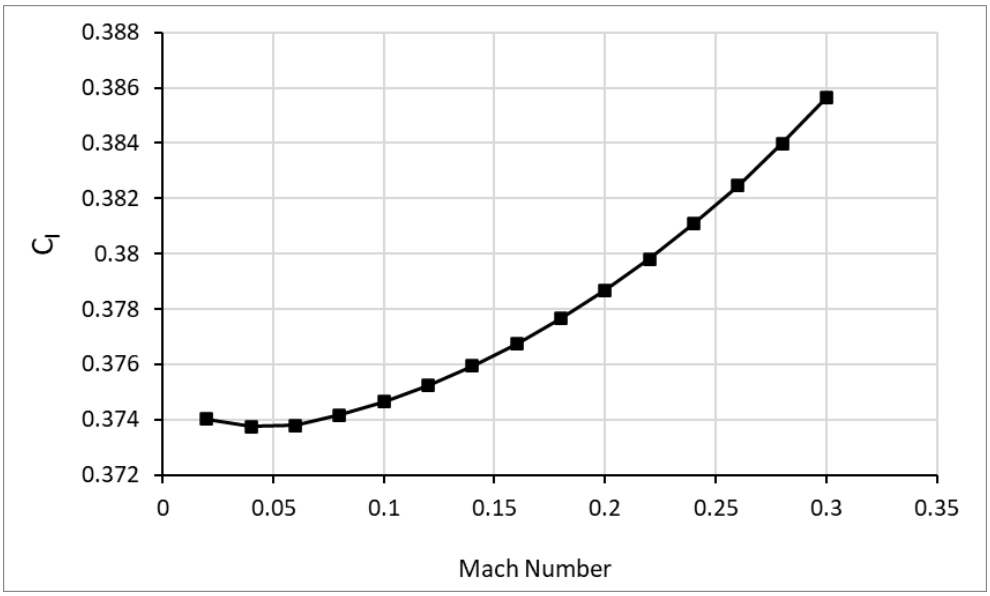

(a) Change of lift coefficient

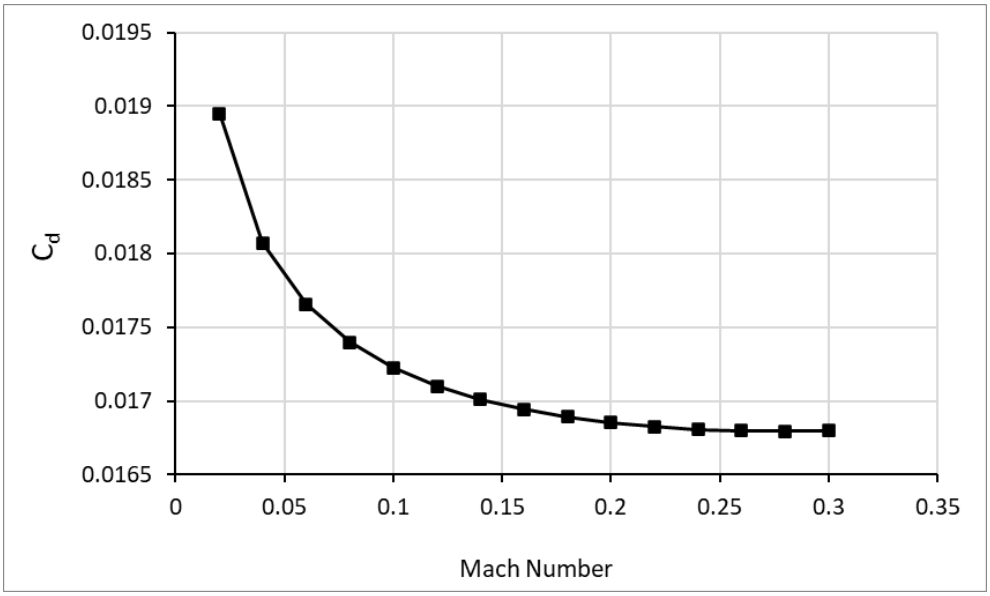

(b) Change of drag coefficient

Figure 3.13. Change of lift (a) and drag (b) coefficients on airfoil NACA 4513 with respect to Mach Number

There is a general pattern observed in the flow coefficients of lift and drag as the Mach number increases. The lift coefficient typically rises, while the drag coefficient tends to decrease. However, there is an unexpected behavior observed

between Mach numbers 0.02 and 0.06. During this range, the lift coefficient decreases, and the change in drag coefficient is quite steep.

To further investigate this phenomenon, we analyzed the pressure coefficient distribution along the normalized chord for four different Mach number samples, as shown in Figure 3.14. Additionally, we examined the distribution of the skin friction coefficient on the upper surface of the airfoil along the normalized chord for the same four Mach number samples, as depicted in Figure 3.15.

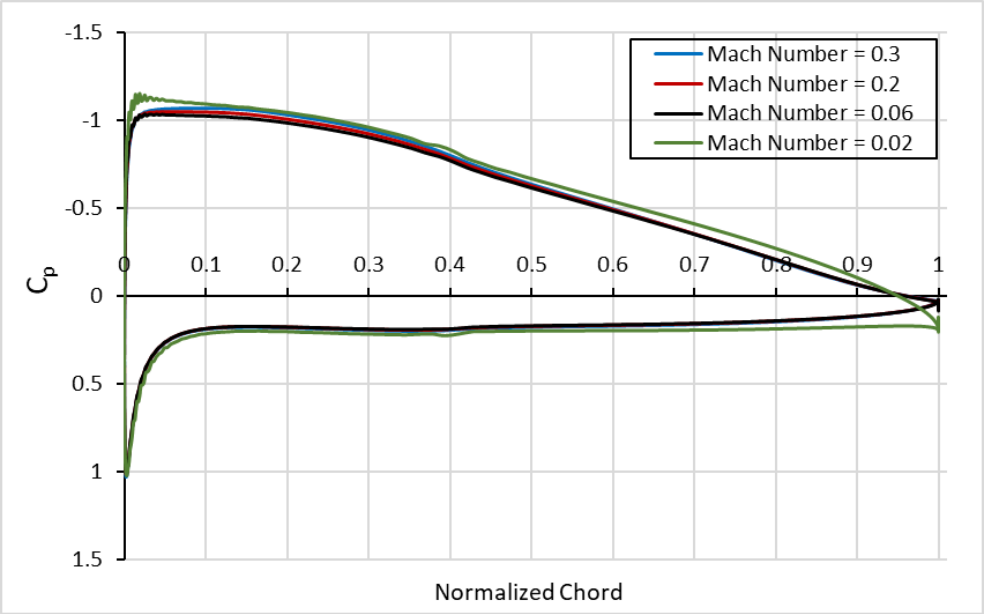

Figure 3.14. Pressure coefficient distribution on upper and lower surfaces of NACA 4513 airfoil with different Mach Numbers

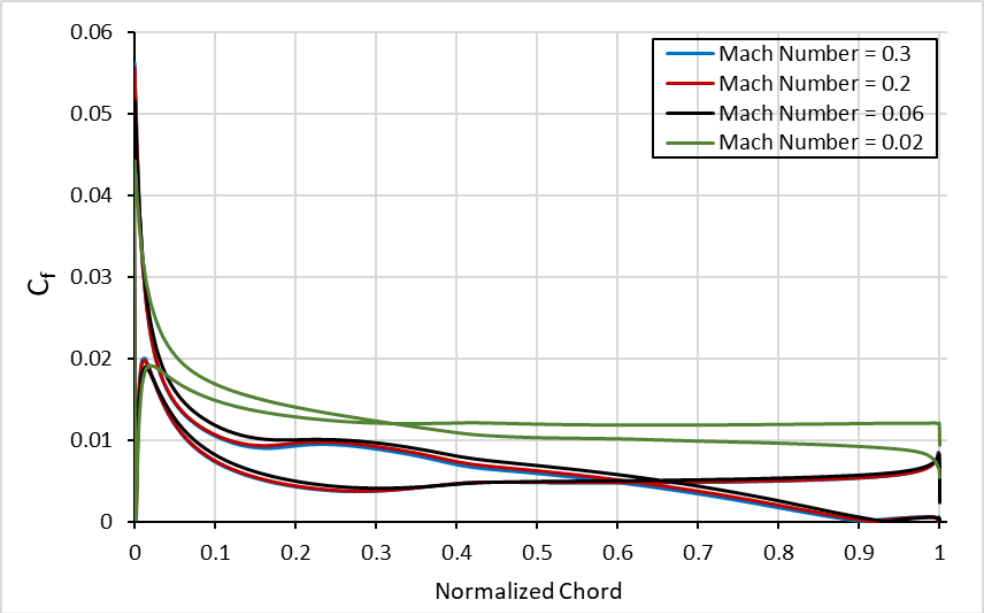

Figure 3.15. Skin Friction coefficient distribution on upper surface of NACA 4513 airfoil with different Mach Numbers

When we look at the trend in increasing lift coefficient with respect to Mach number, it seems reasonable between Mach numbers 0.06 and 0.3. As the flow velocity increases, the fluid exerts more dynamic pressure on the airfoil. This increased pressure creates a greater difference in pressure between the upper and lower surfaces of the airfoil.

The trend of decreasing drag coefficient up to Mach numbers 0.17 can be explained by the reduction in the total thickness of the boundary layer. This decrease in thickness leads to lower skin friction coefficients, which are the dominant factor in drag up to Mach number 0.17. However, between Mach numbers 0.17 and 0.3, there is an increase in drag coefficient due to the pressure components of drag becoming more dominant than friction drag.

Considering these aspects, we would expect a similar behavior between Mach numbers 0.02 and 0.06. However, we observe a drop in lift coefficient and a steep decrease in drag coefficient in these regions. This behavior could be attributed to the capabilities of the solver used and its difficulty in accurately resolving problems at low Mach numbers. As a result, Mach numbers below 0.06 are not

included as computing points, and it is decided to extrapolate the data from the nearest bounds during calculations.

Considering that the changes in both drag and lift coefficients are relatively small compared to other sweep studies, we choose three Mach computing points for the airfoil analysis: 0.06, 0.17, and 0.3. These computing points are decided that they represent significant changes of this specific airfoil characteristics at different Mach numbers.

3.4.1.2 Reynolds Number Computing Points

The change of lift and drag coefficients with respect to changing Reynolds Number is shown in Figure 3.16. During this sweep study, the Mach number is kept constant at 0.2, and the angle of attack is kept constant at 4 degrees.

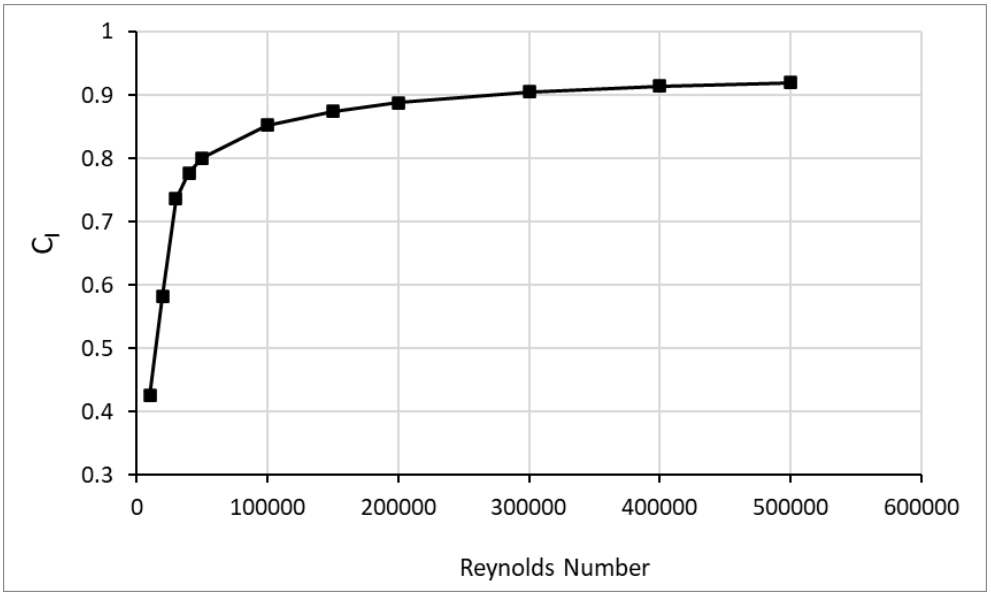

(a) Change of lift coefficient

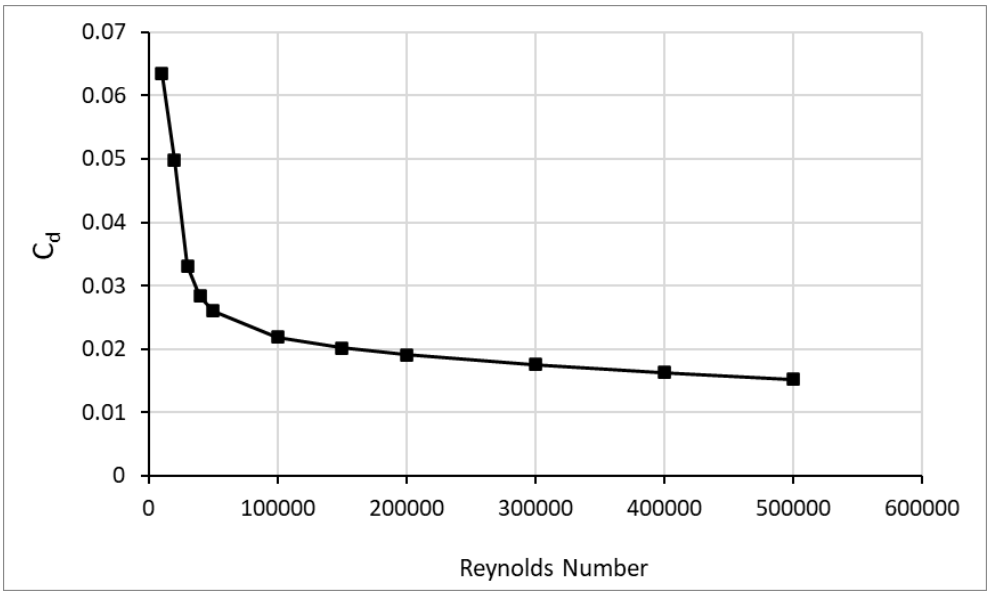

(b) Change of drag coefficient

Figure 3.16. Change of lift (a) and drag (b) coefficients on airfoil NACA 4513 with respect to Reynolds Number

Looking at Figure 3.16, we can clearly see that the Reynolds Number has a more significant impact compared to the Mach sweep. The Reynolds Number directly affects how turbulent the flow is. The most noticeable changes occur at lower Reynolds Numbers, especially when the flow transitions from laminar to turbulent behavior. When it comes to the lift coefficient, we observe an increasing trend as the Reynolds number increases. On the other hand, the drag coefficient shows a decreasing trend as the Reynolds Number increases.

To further investigate this phenomenon, we can examine the pressure coefficient distribution along the normalized chord of the NACA 4513 airfoil for four different Reynolds Number samples, as shown in Figure 3.17. Additionally, Figure 3.18 displays the skin friction coefficient distribution along the normalized chord for the same four Reynolds Number samples.

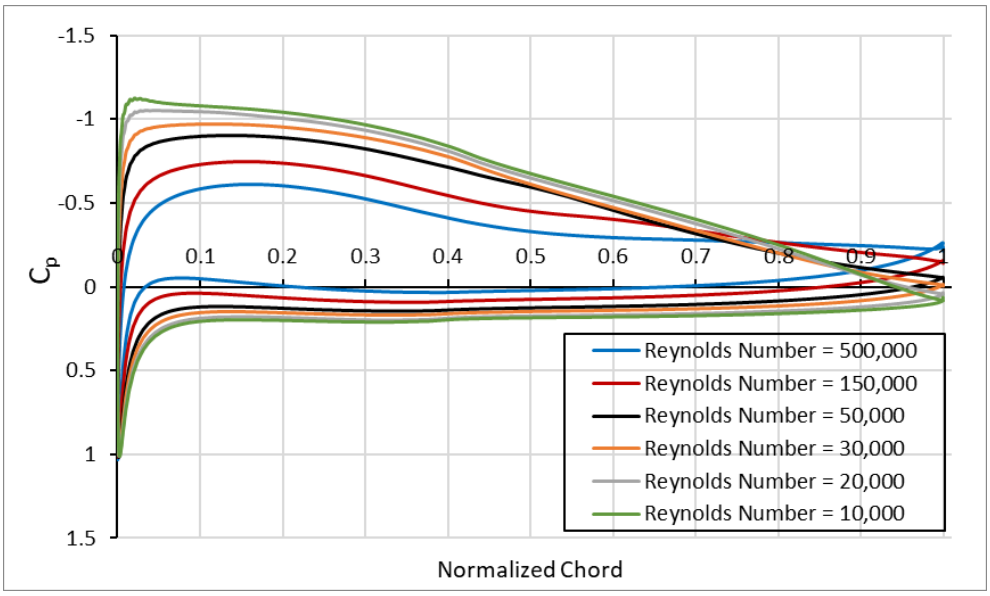

Figure 3.17. Pressure coefficient distribution on upper and lower surfaces of NACA 4513 airfoil with different Reynolds Numbers

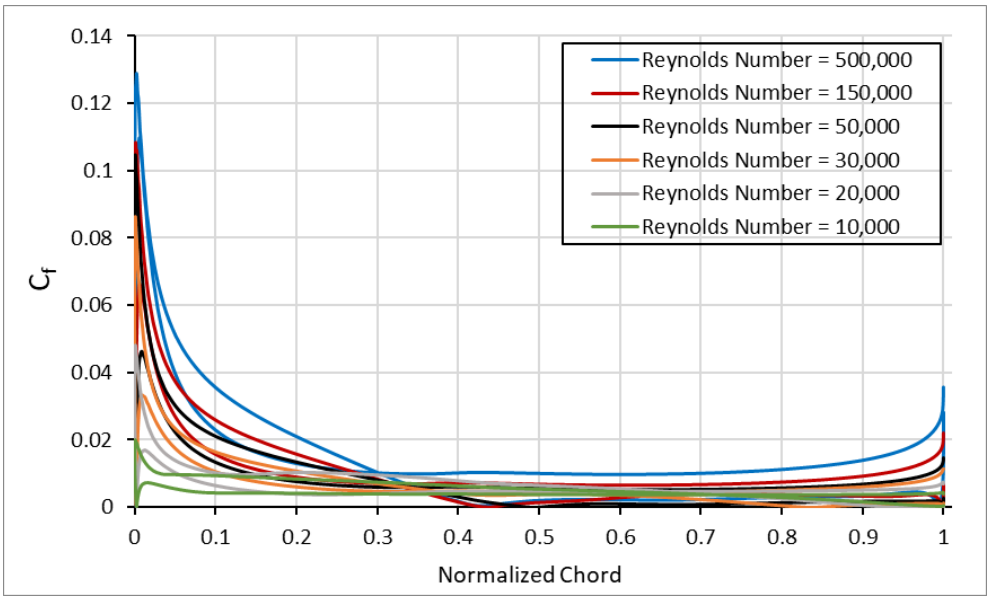

Figure 3.18. Skin Friction coefficient distribution on upper surface of NACA 4513 airfoil with different Reynolds Numbers

Upon reviewing Figure 3.17, the relationship between the lift coefficient and the Reynolds Number appears to be following the general trends. The increase in lift

coefficient with Reynolds Number and the decrease in drag coefficient can be explained by the effects of viscous forces and boundary layer behavior on the airfoil. The increase in Reynolds Number also affects the separation of the flow over the airfoil. Higher Reynolds Numbers tend to delay flow separation, allowing the airflow to stay attached to the airfoil surface for longer. This delayed separation contributes to an increase in lift and decrease in drag. The flow becomes more turbulent. Turbulence can energize the boundary layer, reducing the adverse pressure gradient near the trailing edge of the airfoil and further delaying flow separation. Observing Figure 3.18, we can see that as the Reynolds Number increases, there is a general decrease in skin friction coefficients. This decrease can be attributed to the reduction in boundary layer thickness. The point of transition from laminar to turbulent flow can be roughly identified for Reynolds Numbers below 50,000. However, for a more precise determination of the transition point, a more advanced transition model would be needed. In our analysis, we have employed the k-w SST turbulence model, which is considered adequate for our specific requirements based on the research conducted by Aftab et al. (2016). By examining the skin friction coefficient plots, it is evident that the flow around the airfoil surfaces is assumed to be fully turbulent for Reynolds Numbers above 50,000, as there are no points indicating a close-to-zero skin friction coefficient in these samples.

Based on the assumption that the studies conducted for the Reynolds Number sweep are sufficiently accurate for our specific purpose, we have identified five computing points for the Reynolds Number in order to generate the airfoil database. These computing points are set at the following values: 10,000, 30,000, 50,000, 150,000, and 500,000. By including these specific Reynolds Number values, we aim to ensure a comprehensive and representative dataset that captures the aerodynamic behavior of the airfoil across a range of Reynolds Numbers.

3.4.1.3 Angle of Attack Computing Points

Determining the computing points for the angle of attack is a relatively straightforward process compared to other factors. The general approach is to have fewer computing points in the linear region and more computing points near the stall region, where non-linear effects are more pronounced. However, to ensure consistency with other sweep studies, an angle of attack sweep study was conducted as well. Figure 3.19 shows the variations in lift (a) and drag (b) coefficients for different angle of attacks. The angle of attack sweep study involved changing the angle of attack while keeping the Mach Number constant at 0.2 and the Reynolds Number constant at 200,000.

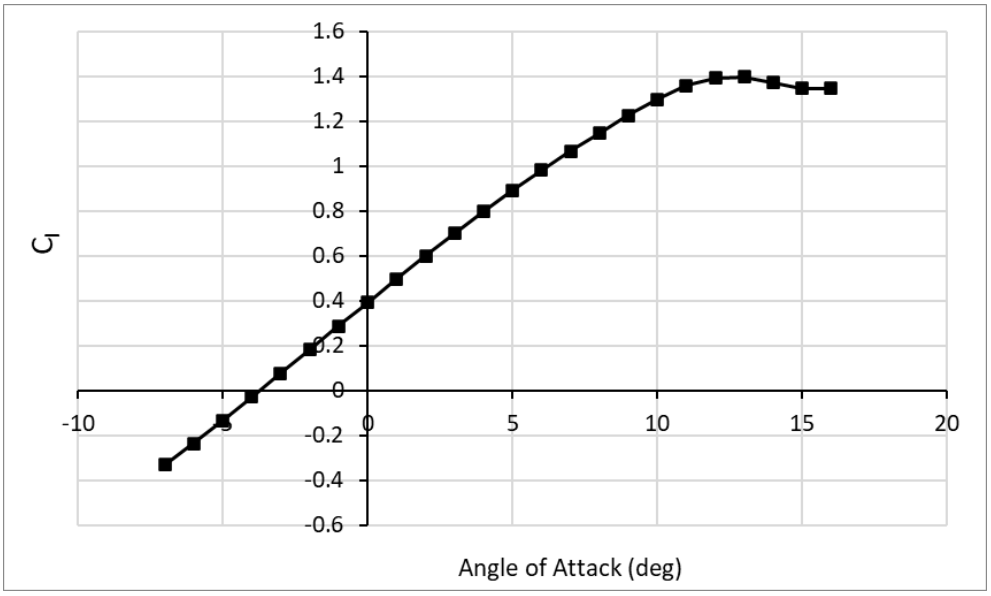

(a) Change of lift coefficient

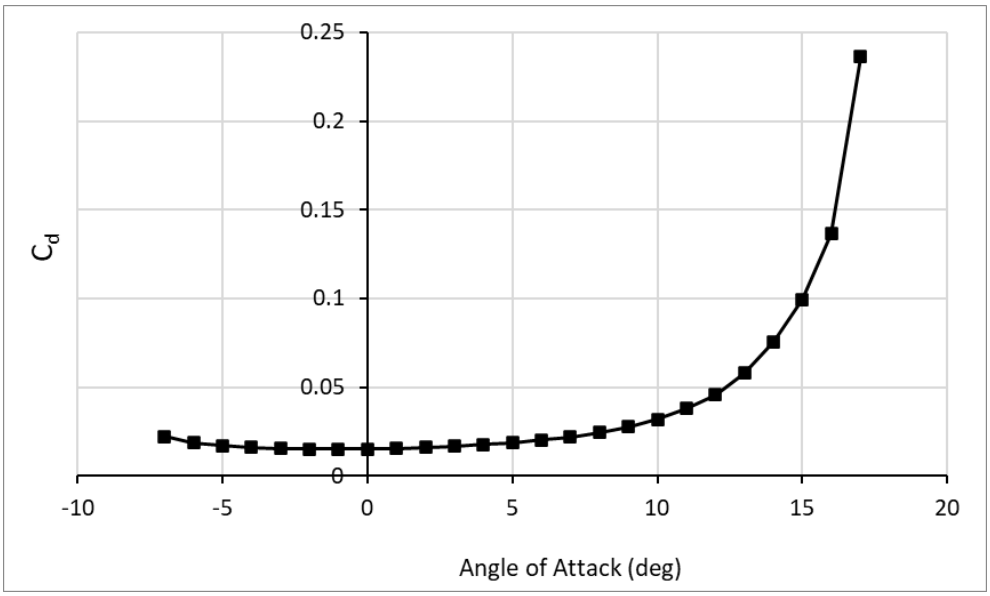

(b) Change of drag coefficient

Figure 3.19. Change of lift (a) and drag (b) coefficients on airfoil NACA 4513 with respect to angle of attack.

Both lift and drag coefficients show an expected change with respect to angle of attack. Although sweep studies are performed within the angle of attack range between -10 and 20, the airfoil database is clipped near the angle of attacks where the stall occurs due to unreliability of steady-state RANS equations after the stall point. The flow after the stall is highly unsteady and chaotic, therefore we need other methodologies to obtain coefficients at higher angle of attacks, which is described in the following section.

To further investigate the effect of the angle of attack, we can examine the pressure coefficient distribution along the normalized chord of the NACA 4513 airfoil for three different angle of attack samples, as shown in Figure 3.20. Additionally, Figure 3.21 displays the skin friction coefficient distribution along the normalized chord for the same three angle of attack samples.

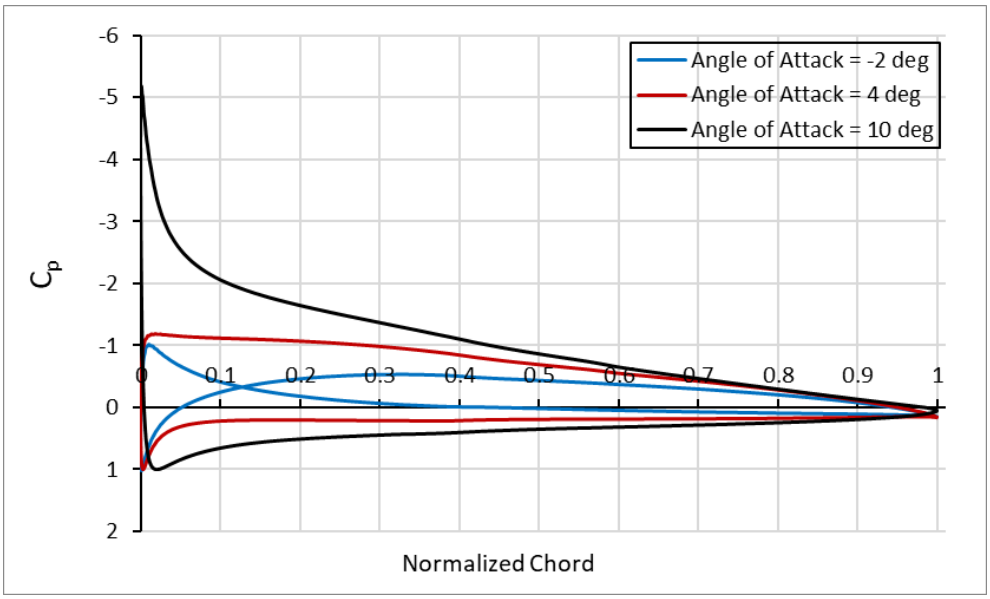

Figure 3.20. Pressure coefficient distribution on upper and lower surfaces of NACA 4513 airfoil with different angle of attacks.

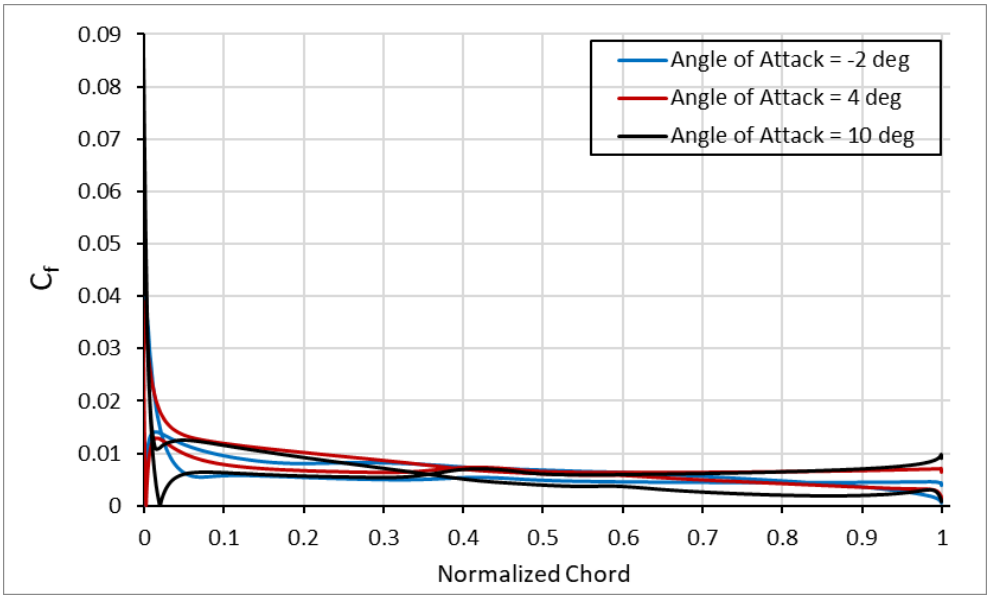

Figure 3.21. Skin Friction coefficient distribution on upper surface of NACA 4513 airfoil with different angle of attacks.

The pressure distribution on the airfoil aligns with our expectations. Higher angles of attack exhibit higher pressure values on the upper surface of the airfoil, and the

peak pressure becomes more pronounced at larger angles of attack. Within the range of -2 to 10 degrees, there is no significant separation observed, indicating a nearly linear behavior in this region. Notably, when examining the pressure and skin friction coefficients, we observe a negative lift at an angle of attack of -2 degrees for this specific airfoil section. In summary, the overall trend in pressure distribution and skin friction coefficient appears accurate, as we would anticipate increased flow acceleration on the upper surface of the airfoil at higher angles of attack, resulting in decreased pressure on that surface. To create the airfoil database, we need to determine the key angle of attack values that capture both the linear and non-linear regions. In total, 12 computing points have been identified to cover the desired range of angle of attacks.

To create the airfoil database, we need to consider various computing points for Mach number, Reynolds Number, and angle of attack. These computing points are selected to cover a wide range of conditions and capture the behavior of the airfoil accurately. Additionally, we need to analyze multiple sections of the blade, ranging from r/R = 0.1 to r/R = 0.9 with a 0.1 increment. This leads to a total of 626 2D airfoil analyses for the generation of the airfoil database, where each analyses took 1.1 minutes with 2000 iterations on an 8-core machine. It's important to note that in subsequent sections, we will use a multiple linear interpolation method between these data points for simplicity and efficiency. Therefore, having a dense airfoil database is essential to ensure accurate interpolation, while considering the limitations of available resources.

After creating the initial airfoil database, we need to make some adjustments to make it suitable for the blade element momentum theory and to incorporate the 3D effects of the blade. In the upcoming sections, we will delve into these methods and explain how we finalize the airfoil database.

3.4.2 Modifications on the Airfoil Database

In order to accurately validate the new enhanced actuator disc model, it is necessary to refine the generated airfoil database. This refinement involves making adjustments to ensure its compatibility with blade element theory and to incorporate important 3D effects like stall delay phenomena, and important extensions such as high angle of attacks flow coefficients. These modifications are crucial to ensure the applicability and reliability of the airfoil database for our validation purposes.

3.4.2.1 Stall Delay Model

In rotating blades, stall delay refers to the phenomenon where the flow separation and the decrease in lift is delayed due to the rotational effects of the blades. The rotation can enhance the flow stability and alter the flow patterns, resulting in a delayed stall and improved aerodynamic performance at higher angles of attack. (Himmelskamp, 1947) In order to account for these rotational effects, several models have been developed to modify 2D airfoil aerodynamic data to be used in blade element momentum theory applications. One of these can be used in this study as well, since the corrections should be directly applied to the database itself, instead of modifying the source code.

One of the stall delay models introduced by Snel (1994), was successfully implemented, and evaluated in Gur et al. (2005) study with wind turbine applications. This stall delay model focuses on improving the modeling of stalled flow on rotating blades, aiming to predict rotor performance in the stall regime. Through the analysis of boundary layer equations, formulation of a quasi-3D system, extension of a viscous inviscid interaction code, and comparison with measurements, a correction formula for obtaining rotating airfoil data was developed, yielding power curves closer to measurements compared to 2D airfoil data.

The Corrigan and Schilling's stall delay model (Corrigan et al., 1994) is a mathematical approach used to estimate the delay in stall occurrence for helicopter rotor blades. It incorporates factors such as blade geometry, operational conditions, and aerodynamic characteristics to predict the onset of stall and improve the performance of rotor blades in various flight conditions. This model was also successfully implemented and evaluated in Tangler's (1997) studies. This model establishes a correlation between the ratio of local blade chord to radius and the delay in stall, which is characterized by a shift in the angle-of-attack of the non-rotating coefficients as presented in Equation 3.14. The implementation of this method involves straightforward modifications to the 2D airfoil data tables, resulting in a significant and realistic improvement in overall rotor power. (Tangler et al., 1997) Therefore, this model has been the perfect candidate to modify the airfoil database for BET-CFD validation.

$$\Delta\alpha = (\alpha_{Cl_{max}} - \alpha_{Cl=0})\left(\left(\frac{K\left(\frac{c}{r}\right)}{0.136}\right)^{n'} - 1\right) \tag{3.23}$$

Based on Equation 3.23, we need detailed investigation in the existing airfoil database, as each angle of attack sweep that corresponds to a specific blade section, Mach number point and Reynolds Number point should be modified independently. α_{Cl_max} is the angle of attack where the maximum lift coefficient occurs, $\alpha_{Cl=0}$ is the angle of attack where the zero lift occurs. K is defined as a parameter for the velocity gradient, and its empirical relation with the separation point, $\frac{c}{r}$ which was assumed to be at the trailing edge in this study, is defined in Figure 3.22.

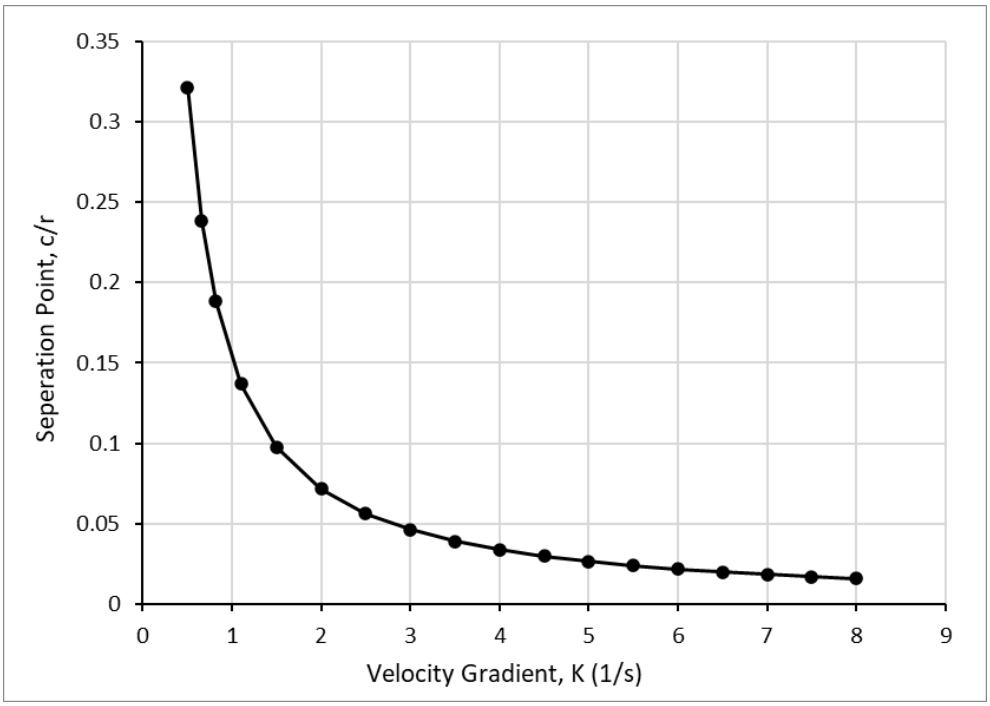

Figure 3.22. Relation between the separation point, c/r and velocity gradient, K.

Once the shift in angle of attack is obtained due to rotational effects, the lift coefficient can also be modified as Equation 3.24.

$$C_{l_{rot}}(\alpha + \Delta\alpha) = C_{l_{non-rot}}(\alpha + \Delta\alpha) + \left(\frac{\partial C_l}{\partial \alpha}\right)\Delta\alpha \qquad (3.24)$$

Based on the approach proposed by MacNeill (2017), the lift coefficient is adjusted based on the new angle of attack increment, while the drag coefficient is modified by only shifting the angle of attack. The adjustments in lift and drag coefficients to incorporate rotational effects at blade section r/R = 0.5, Mach Number = 0.2, and Reynolds Number 200,000, following the methodology suggested by Corrigan and Schillings (1994), are illustrated in Figure 3.23.

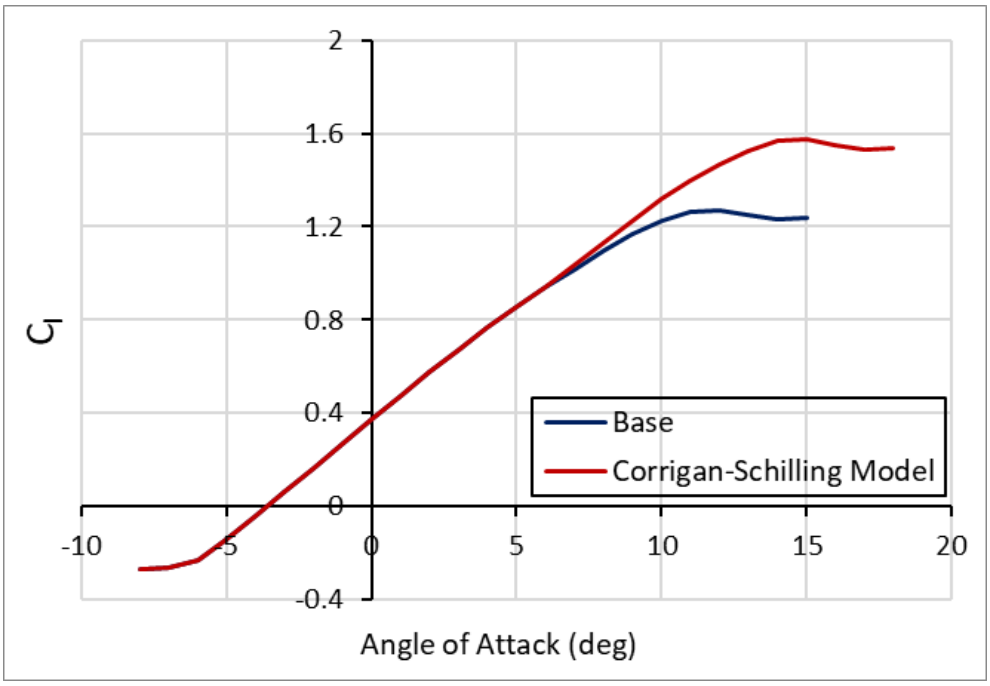

(a) Change and shift in lift coefficients

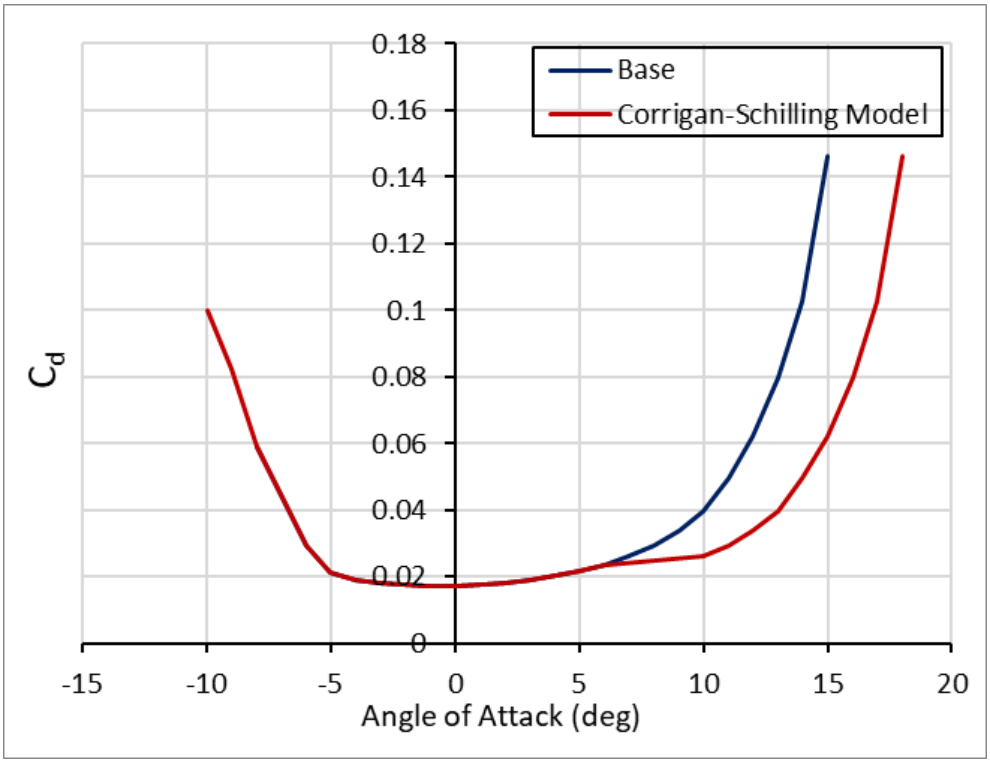

(b) Shift in drag coefficients

Figure 3.23. (a) Lift coefficient and (b) Drag coefficient versus angle of attack for base configuration without a stall delay model and with the Corrigan-Schilling Stall Delay Model

All flow coefficients in the airfoil database if modified accordingly, and the results would be similar in all of them to the one presented in Figure 3.23. The modifications in flow coefficients are primarily targeted at higher angle of attacks. This implies that the model's impact will be more pronounced during lower advance ratios of the blade, where the effective angle of attack tends to be relatively higher compared to other operating conditions.

3.4.2.2 High Angle of Attack Aerodynamics

Steady-state RANS computations are accurate up to a certain point, and they become less reliable as the airfoil sections reach angles beyond the stall. Analyzing points beyond the stall angle would require more computational resources due to an increased number of analysis points and the need for higher fidelity solvers like URANS (Unsteady Reynolds Averaged Navier-Stokes Equations). However, flow coefficients at high angles of attack are essential for applications such as blade element momentum theory. Consequently, several models have been developed to generate these coefficients and accurately represent the flow behavior at high angles of attack.

One approach is to rely on experimental data, such as the comprehensive study conducted by Critzos et al. (1955), which examined the aerodynamic characteristics of the NACA 0012 airfoil across a wide range of angles of attack up to 180 degrees. However, it should be noted that this method would be specific to one airfoil type, and won’t fully consider the impact of airfoil shape variations and specific flow characteristics.

The Viterna-Corrigan method (Viterna et al., 1982), is a technique used to extrapolate data for angles of attack greater than the stall angle but less than or

equal to 90 degrees. This method was developed based on flat plate theory and relies on an initial angle of attack, which would be the stall angle in this case. In this study, this methodology is preferred as it allows for extrapolation that is tailored to each airfoil configuration and flow condition, utilizing the maximum lift coefficient specific to each condition.

The Viterna-Corrigan method is designed to estimate or predict the lift and drag coefficients through the utilization of the following equations:

$$C_l = A_1 sin2\alpha + A_2 \frac{\cos^2 \alpha}{sin\alpha} \tag{3.25}$$

$$C_d = B_1 \sin^2 \alpha + B_2 cos\alpha, \tag{3.26}$$

Where A_1, A_2, B_1 and B_2 are obtained by following equations:

$$A_1 = \frac{C_{d_{max}}}{2} \tag{3.27}$$

$$A_2 = C_{l_{stall}} - C_{d_{max}} \sin \alpha_{stall} \cos \alpha_{stall} \tag{3.28}$$

$$B_1 = C_{d_{max}} = 1.11 + 0.018AR \tag{3.29}$$

$$B_2 = C_{d_{stall}} - \frac{C_{d_{stall}} \sin^2 \alpha_{stall}}{cos\alpha_{stall}} \tag{3.30}$$

In Equation 3.27 the $C_{d_{max}}$ corresponds to maximum drag coeficient, and can be calculated by using Equation 3.29 where the AR represents the aspect ratio of the blade. Following the equations above, each angle of attack sweep that corresponds to different blade section and flow conditions are extrapolated up to 90 and -90 degrees. The fact that the model can extrapolate up to 90 degrees is more than sufficient, since the blades are subjected to higher angle of attacks rarely, but still we are able to use a different methodology for beyond 90 degrees which has relatively lower fidelity such as flat plate theory. (Mahmuddina, 2016) In the high angle of attack region according to flat plate theory, the upper surface of the airfoil

experiences flow separation and does not receive direct impact from the flow. The lower surface, on the other hand, exhibits completely laminar flow and contributes minimally to the overall drag force. As a result, when the airfoil is positioned at a high angle of attack, it behaves similarly to a thin flat plate. (Tangler, 2004) Using Viterna and Corrigan's methodology for angle of attacks up to 90 degrees, and the flat plate theory which is given in Equation 3.31 and Equation 3.32 for beyond seems only accurate and sufficient.

$$C_l = 2\sin\alpha\cos\alpha \tag{3.31}$$

$$C_d = 2\sin^2\alpha \tag{3.32}$$

The results of extrapolation for the NACA 4513 airfoil, blade section r/R = 0.5, Mach Number 0.2, and Reynolds Number 200,000, is presented in Figure 3.24.

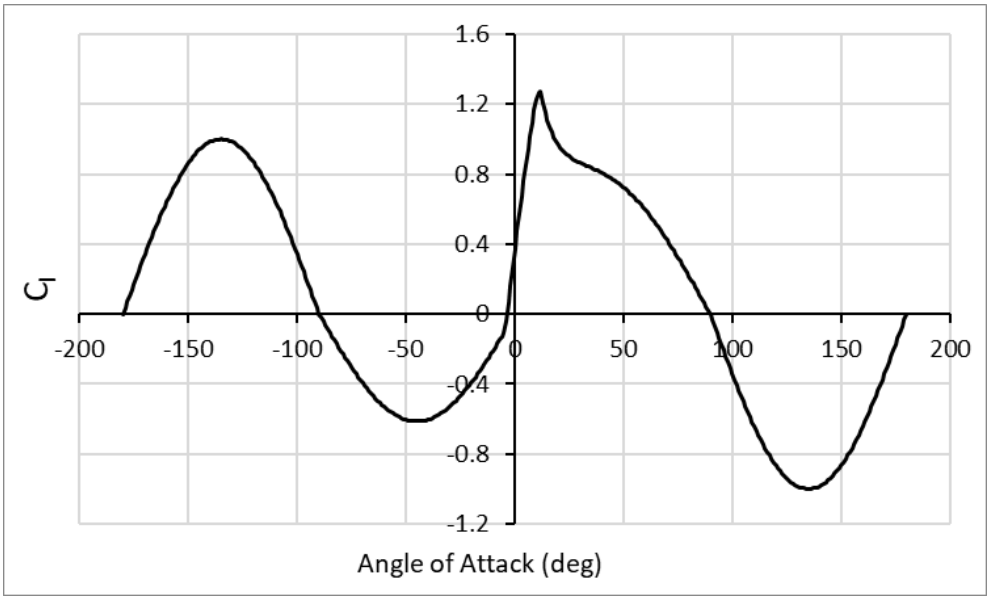

(a) Lift coefficient vs angle of attack

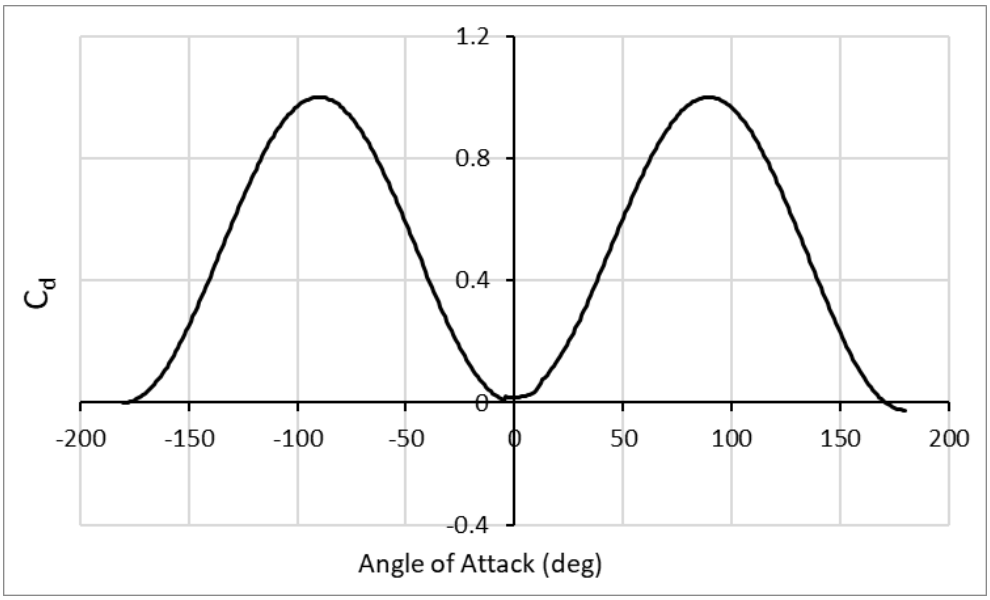

(b) Drag coefficient vs angle of attack

Figure 3.24. (a) Lift coefficient and (b) Drag coefficient versus angle of attack extrapolated from -180 to 180 degrees

Please note that there is a discrepancy between the drag coefficients at a 90 degree angle of attack in Viterna-Corrigan's method and flat plate theory. To address this, a scaling factor is applied to the Viterna-Corrigan method for positive angles of attack up to 90 degrees, based on the maximum drag coefficient as described in Equation 3.29.

The same extrapolation methodology is applied to all blade sections, as well as the various Mach Number and Reynolds Number computing points, to determine the flow coefficients. It is important to emphasize that the extrapolation should be performed after applying all correction factors to the database to maintain continuity in the nonlinear regions. Once the extrapolation is completed, the 2D airfoil database is considered finalized.

3.5 Integrating Blade Element Theory with SU2

Successfully implementing the new actuator disc model using blade element theory in SU2 necessitates a thorough comprehension of the underlying code structure. It is essential to modify the code in a manner that preserves its user-friendliness, facilitating ease of use for both experienced and new users. Additionally, the code modifications should effectively serve our intended purpose while minimizing any potential impact on performance.

At the core of SU2 is the CFD solver module, which employs various numerical methods to solve the governing equations for fluid flow. The code structure includes modules for handling turbulence modeling, boundary conditions, and physical models for different flow regimes. These modules provide flexibility in selecting appropriate models based on the specific simulation requirements. (Palacios et al., 2013) Overall, the code structure of SU2 is designed to be modular, flexible, and extensible, allowing users to customize and adapt the code to their specific needs.

Integrating the BET method into a CFD code involves replacing the physical blades in the flow domain with an arbitrary disc domain, as depicted in Figure 3.25. The domain shown on the left consists of tetrahedral and prism layers to enable accurate computations using a rotating frame and sliding mesh approach, which significantly increases the computational requirements. On the right, the domain represents an actuator disc model, consisting of hexahedral volume elements where the aerodynamic forces are distributed as momentum sources.

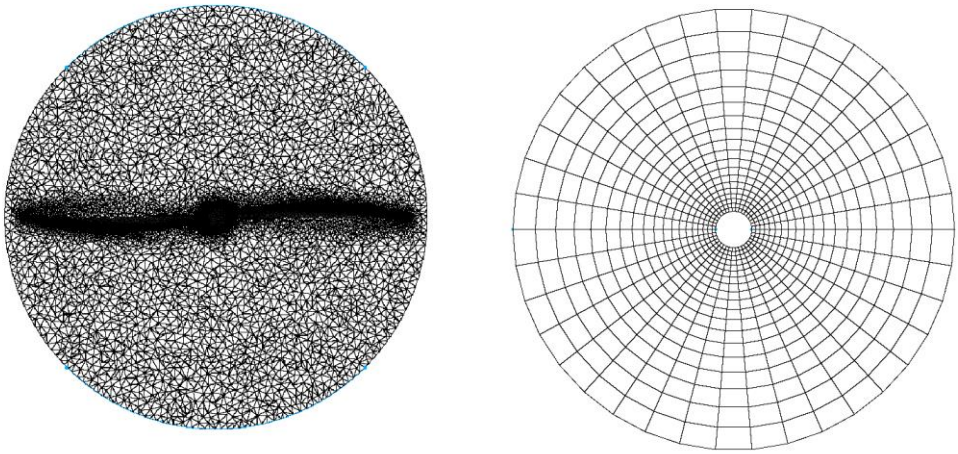

Figure 3.25. Comparison of spatial domain representations used in different approaches: (left) Rotating frame and sliding mesh approach, and (right) Actuator disc model.

Instead of relying on classical momentum theory, the axial and tangential velocities are now computed using CFD equations. The resulting forces on the domain are incorporated into the Navier-Stokes equations through the use of momentum sources. This modification leads to a slight change in the workflow, transitioning from the original Figure 3.9 to a modified version depicted in Figure 3.26. Instead of initialization induction factors, now a standard CFD initialization through the domain is used. In Figure 3.26, V_x, V_y, and V_z corresponds to velocities in x, y, and z directions obtained from each node. They are converted into axial and tangential velocities by using geometrical properties and rotation rate of the blades. Once the effective angle of attack, induced flow angle, and total velocity obtained, resultant forces (F_x, F_y and F_z) in each node can be computed and transformed into momentum sources. Convergence is checked by the CFD solvers by observing residuals in continuity, momentum and energy. If the convergence is not reached yet, the same circle is repeated as an iteration.

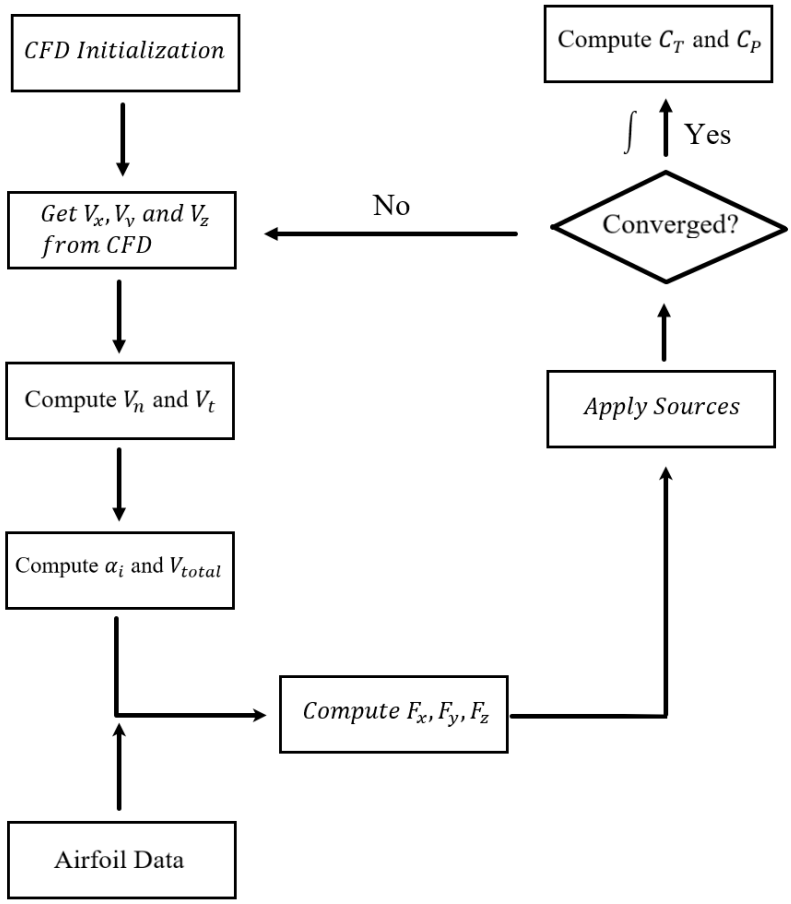

Figure 3.26. Representation of the coupling of blade element theory and CFD

Implementation of the BET to SU2 software requires modifications in several parts of the source code. In order to proceed, an understanding of the certain equations solved within the solver was necessary.

3.5.1 A CFD Specific Overview of the SU2 Code Architecture

The core components of the SU2 software are the C++ executables, which have been designed with specific functionalities and take advantage of modern programming language features like class inheritance and polymorphism. This design promotes code reuse and allows for the efficient implementation of new algorithms and numerical methods within the existing framework. All modules

share a common C++ class structure, enabling easy integration of capabilities across different modules. (Economan, 2016)

SU2 offers various core capabilities, including SU2_CFD for solving steady or unsteady Euler, Navier-Stokes, and RANS equations, as well as SU2_DEF for considering mesh deformation, among others. In this study, our primary focus is on the SU2_CFD module, which is commonly utilized for fluid flow simulations. A simplified overview of the SU2_CFD module is given in Figure 3.27.

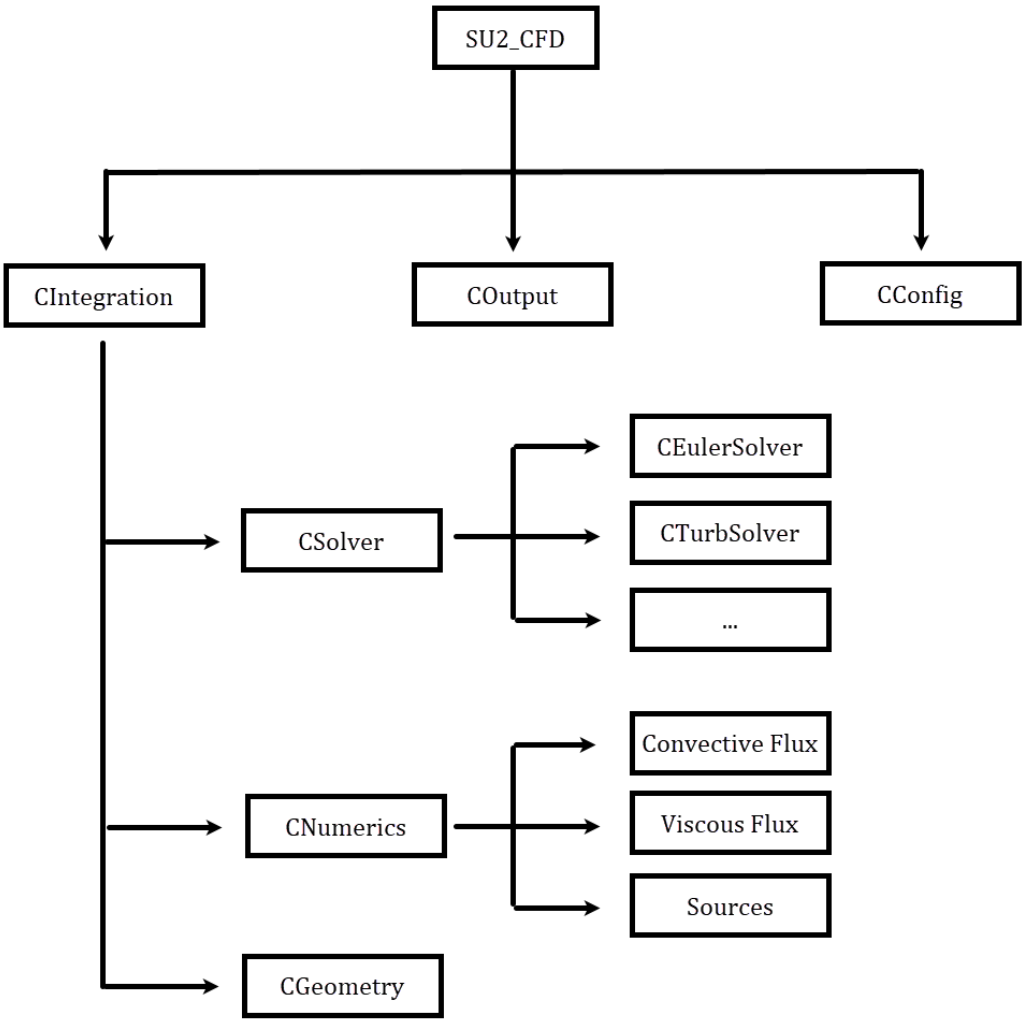

Figure 3.27. Overview of the SU2_CFD module in SU2 software

Figure 3.27 illustrates the SU2_CFD module, which consists of three primary classes: CIntegration, COutput, and CConfig. In CIntegration, the governing equations are integrated, while COutput is responsible for organizing and preparing the solution fields and numerical outputs. The CConfig class reads the necessary input file (configuration file) and gathers information to be passed on to the other classes.

The SU2 module CIntegration connects three subclasses: CSolver, CNumerics, and CGeometry. In the CGeometry subclass, the input geometry is processed and prepared for computations based on its format. The CSolver class implements solver methodologies and computes variables for the next iteration by iterating over the nodes. It includes different solver types like CEulerSolver and CTurbSolver, which communicate with each other through the solution. For instance, the rotating frame approach is embedded in the CEulerSolver child class and is activated when the solution is chosen as turbulent as well. The CNumerics subclass provides methods for computing convective and viscous fluxes, as well as additional source terms. Various flux splitting methodologies are available within this class to calculate fluxes.

In implementing a new actuator disc model using blade element momentum theory, the main classes of interest are CConfig, CEulerSolver, and CNumerics, following the given methodology for the rotating frame.

3.5.1.1 CConfig: Configuring the Model

SU2 software uses configuration files with the ".cfg" extension as input files. These files contain information about the operating conditions, mesh settings, and computational methods. The solver reads and interprets these files before starting the iterations. By using configuration files, the software becomes more user-friendly, allowing users to easily access and apply different methodologies. This enhancement simplifies the process of defining and utilizing new methodologies.

When using SU2 software, users have the flexibility to utilize multiple configuration files. These files allow users to define different methodologies and operating conditions for each mesh domain separately. In the case of the new actuator disc model, multiple configuration files are used to enhance the process and provide a clear distinction between the stationary and actuator disc zones. To effectively use this model, it is recommended for users to create a main configuration file where global methodologies are defined, along with two additional sub configuration files. These sub files can be used to specify the specific characteristics of the stationary and actuator disc domains, respectively.

The CConfig file, along with its headers, can be found in the Common folder within the SU2 software. To create a new methodology that can be defined using a configuration file, the method name should be specified in the option_structure.hpp header file. This header file contains the definitions of all character variables corresponding to inputs in the configuration file.

In this case, the new methodology is defined as "AEDISC" under the Grid Movement option in the option_structure.hpp file. Although the methodology itself is not related to grid motion, it is classified as Grid Movement to align it with other rotating part solver capabilities in SU2. Users who wish to utilize this model should specify "Grid Movement = AEDISC" in their sub-configuration file representing the actuator disc domain. Multiple actuator disc zones can be defined by using multiple sub-configuration files for these computations. Stationary domains can be initialized with a Grid Movement option of "None". Then the AEDISC method is defined as a kind of grid movement in CConfig.cpp file, where a boolen is generated for this flag as “True” in case it is enabled in the configuration file, and as “False” in case it’s not activated in the configuration file. Once this boolen is generated, it will be sent to CSolver where it will be activated or deactivated depending on the boolen type.

Once the AEDISC model is enabled in the configuration file, two additional inputs need to be added to the sub-configuration file. These inputs are introduced and

defined in both the option_structure.hpp and CConfig.cpp files. The first input is used to specify the global characteristics of the blades, and it should be added to the sub-configuration file as "AEDISC Blade File Name = X.dat". The X.dat file mentioned in this line should include the following lines:

AE Center of Rotation: As the name suggest the coordinates of the rotation center of the actuator disc should be defined properly as in three directions. Three inputs should contain at least one space between them.

AE Rotation Axis: A direction vector should be defined, in order to account for the rotation direction. The vector doesn't necessarily have to be a unit vector. It will be normalized in case it's not unit vector by the solver.

AE Radius: Radius of the rotating part should be defined here. This information is used to integrate resultant coefficients through the domain.

AE Rotation Rate: Magnitude of the rotational velocity should be defined here in units rad/s. This input is used to actuate the rotating flow inside the domain.

AE Number of Blades: Number of blades of the rotating parts should be defined here. This input is used to calculate the solidity of the rotating parts.

AE Number of Sections: Number of sections that will cut through the blade to perform the blade element methodology should be defined here. Users should provide the same number of inputs whatever the number they give here.

AE Section Properties: In this section, we will provide the geometric properties of the blades. For each section, we need to enter three properties next to each other, with at least one space between them. These properties are the local radius r/R, the chord length (in meters), and the pitch angle (in degrees). It is important to ensure that the units you use for these properties are consistent with the units used in the flow domain. Additionally, the pitch value you specify here represents the total pitch of the blade starting from the 0-degree angle of attack condition.

It is important to ensure that the inputs provided in this section are consistent with the properties of the actuator disc domain. Using mismatched inputs may result in inaccurate results. Appendix B provides a representation of the blade input file to guide users in specifying the correct inputs.

The second input file required for utilizing the AEDISC model is the aerodynamic database of the sections. In the sub-configuration file, users should include the input file as "AEDISC Section File Name = X.dat". The specified dat file should contain the following lines:

nSection: Number of sections that aerodynamic properties are provided. This value doesn't necessarily have to be matching with the **AE Number of Sections** in the blade input file. Both input files undergo their own interpolation process.

nMach: Number of Mach Number computing points provided in the database.

nReynolds: Number of Reynolds Number computing points provided in the database.

nAoa: Number of Angle of Attack computing points provided in the database.

Aerodynamic Database: This section should include lift and drag coefficients provided in each section, Mach Number, Reynolds Number and Angle of Attacks. They should be given side by side for each point, and they should include at least one spacing between them. A representation of the section input file is given in Appendix C.

One important note is that all inputs presented inside .dat files doesn't have to be defined in option_structure.hpp and CConfig.cpp files, as they are only read in case the AEDISC model is enabled. Therefore, these input files are read in the solver part. However, the file names should be already defined in header and source file as mentioned before.

Once the necessary inputs are defined and the model is enabled by using a boolen, the model will be activated inside the solver part where we can perform node-based operations.

3.5.1.2 CEulerSolver: Computing the Blade Forces

CEulerSolver is a very important class within the SU2 software that handles the implementation of boundary conditions in the flow domain and conducts the solution computation by iterating over each node. It encompasses various flow variables essential for the simulation, including velocity, density, temperature, dynamic viscosity, and more. This class specifically focuses on non-viscous operations, distinguishing it from CTurbSolver. Since the outputs of the new model do not directly influence the viscosity, a significant portion of the computations related to blade element theory is incorporated within CEulerSolver, similar to the rotating frame approach.

In CEulerSolver, there is an added advantage of being able to iterate over the nodes, which is beneficial for computing resultant forces by using blade element theory. Since blade element theory considers flow characteristics to be unique and independent in each section, the ability to perform computations based on individual nodes is precisely what we need.

Once the AEDISC model is enabled in the configuration file, necessary computations will be performed to utilize the disc model. For the sake of efficiency, certain operations such as determining the radial location of the points inside the disc domain, are only performed only once at iteration 0.

At iteration 0, computations start by allocating memory for geometrical properties of each node inside the domain, by using nPointDomain variable which was already defined in the solver. Input file given for the global properties of the blade is also read only once at iteration 0, and geometrical properties of the blade is obtained. First, we need to compute the radial location of each node in CFD

domain which will naturally remain constant during throughout the computation. GetCoord function in the class is used to obtain the x, y, and z coordinates of the nodes, which will be $\vec{p} = (p_x, p_y, p_z)$. Radial location of the nodes, from the rotation center which was obtained from blade input file, $q = \left(q_x, q_y, q_z\right)$, will be normalized with respect to blade radius and be represented as $r' = r/R$, where r is the absolute radial distance of the node from rotation center, and R is the blade radius obtained from blade input file as well. We can use the formula that compute the distance between a point and a line, after we obtained and converted the rotation axis of the blades, $\overrightarrow{n_\omega} = (n_{\omega_x}, n_{\omega_y}, n_{\omega_z})$ from blade input file into a unit vector, by using Equation 3.33 and Equation 3.34.

$$r = \frac{(\overrightarrow{pq}\ x\ \vec{n})}{||\vec{n}||} \tag{3.33}$$

$$r' = \frac{r}{R} \tag{3.34}$$

A unit vector to represent the radial direction of each node, $\overrightarrow{n_r}$ is computed by using the following Equation 3.35.

$$\overrightarrow{n_r} = \frac{p - q}{r} \tag{3.35}$$

Based on the axis of rotation of the blade, and radial direction of each node, a tangential unit vector, $\overrightarrow{n_t}$ for each node can be computed by the cross product of axis of rotation and radial direction of the node. This is an important parameter to accurately compute the effective angle of attack at all locations inside the blade, and the cross product is shown in Equation 3.36.

$$\overrightarrow{n_t} = \overrightarrow{n_\omega}\ x\ \overrightarrow{n_r} \tag{3.36}$$

After the necessary directions are obtained at iteration 0, geometrical properties such as chord and pitch should be interpolated in each node. In order to do that, a linear interpolation is used based on the radial location of each node and the data

provided in the blade input file. The nodes that are located outside of the bounds of data provided in the input file, are extrapolated by using the closest bound values.

Finally, the solidity, ε in each node is calculated based on the Equation 3.14. at iteration 0.

From this point, each calculation is performed in each iteration rather than only performing at iteration 0, since flow properties will be included in the calculation now and they should be updated in each iteration. To assess the flow velocity on a specific node, GetPrimitive function is used where 0 index corresponds to mass, and 1-3 indices correspond to velocity components in x, y, z directions, $\vec{v} = (v_x, v_y, v_z)$. Flow speed calculated in axial direction on the node is obtained by using Equation 3.37,

$$v_a = \vec{v} \cdot \overrightarrow{n_\omega} \tag{3.37}$$

and flow speed calculated in tangential direction on the node is obtained by using Equation 3.38 as follows:

$$v_t = \vec{v} \cdot \overrightarrow{n_t} \tag{3.38}$$

Once the tangential speed is obtained, total flow speed experienced by the blade in tangential direction can be computed by using Equation 3.39.

$$v_{t_{total}} = v_t + \omega r' R \tag{3.39}$$

Using findings from Equation 3.34 and Equation 3.36, total flow speed on the node is obtained by using the following Equation 3.40.

$$v_{total} = \sqrt{v_a^2 + v_{t_{total}}^2} \tag{3.40}$$

As we progress into calculating the angle of attacks experienced by the blade section that corresponds to the specific node, we first need to calculate the angle of attack induced by the flow, which is presented in Equation 3.41.

$$\alpha_i = -\tan^{-1}\left(\frac{v_a}{v_{t_{total}}}\right) \tag{3.41}$$

Hence, the corresponding angle of attack experienced by the blade can be computed by subtracting the pitch value, θ which was obtained from the blade input file, and was after interpolated for the specific node, from the induced angle of attack as shown in Equation 3.42.

$$\alpha = \alpha_i - \theta \tag{3.42}$$

Mach Number can be calculated based on the total flow speed on the node, and temperature, T by using Equation 3.43.

$$M = \frac{v_{total}}{\sqrt{\gamma RT}} \tag{3.43}$$

Where γ is the specific heat ratio, and obtained within the solver by using GetGamma function, R is the universal gas constant, and T is obtained from the 4th index of the GetPrimitive function.

Reynolds Number on the node is calculated based on the total flow speed by using the Equation 3.44.

$$Re = \frac{\rho v_{total} c}{\mu} \tag{3.44}$$

In Equation 3.41 ρ is the density and it's gathered by using function GetDensity, c is the local chord of the blade section that corresponds to the specific node, μ is the total viscosity and obtained by using function GetViscosity.

Once all four independent variables, Mach Number, Reynolds Number and Angle of Attack are obtained, we can use the input file given to represent the airfoil aerodynamic database of each section to obtain lift coefficient $C_l(r', M, Re, \alpha)$ and drag coefficient $C_d(r', M, Re, \alpha)$. A multiple linear interpolation is used to obtain lift and drag coefficient experienced on the specific node, and then they are

transformed into axial forces, F_a and tangential forces, F_t by using Equation 3.45 and Equation 3.46.

$$F_a = \frac{1}{2}\rho v_{total}^2 c(C_l \cos(\alpha_i) - C_d \sin(\alpha_i)) \tag{3.45}$$

$$F_t = \frac{1}{2}\rho v_{total}^2 c(-C_l \sin(\alpha_i) - C_d \cos(\alpha_i)) \tag{3.46}$$

Then finally, forces exerted on each node by the blade section in cartesian coordinates can be calculated as:

$$F_x = F_a n_{\omega_x} + F_t n_{t_x} \tag{3.47}$$

$$F_y = F_a n_{\omega_y} + F_t n_{t_y} \tag{3.48}$$

$$F_z = F_a n_{\omega_z} + F_t n_{t_z} \tag{3.49}$$

As the computation of the forces are completed, we can proceed to send the computed forces to CNumerics class to be implemented as momentum sources.

3.5.1.3 CNumerics: Implementing Blade Forces as Momentum Sources

The forces computed in cartesian coordinates in CEulerSolver is sent to CNumerics class by using a custom SendAeDiscForces function defined in header file of CNumerics.

Implementation of the forces as momentum sources first requires an understanding of the units and non-dimensionalization of the sources inside the CNumerics class. After the forces are computed in CEulerSolver, the source term presented in Equation 3.5 becomes to Equation 3.50.

$$Q = \begin{pmatrix} 0 \\ \vec{F} \\ 0 \end{pmatrix} \tag{3.50}$$

We can not directly apply the forces as momentum sources in this case, as they are obtained in each node, and each node has a unique cell volume that contains an

amount of mass. Hence, we should consider the forces applied to the whole domain volume, and scale the forces with respect to their corresponding node-cell volume. This can be enhanced by using Equation 3.51.

$$\vec{F}' = \frac{\vec{F}\varphi_i}{\varphi} \tag{3.51}$$

Where φ_i is the volume of the node-cell, which is obtained by using Volume variable inside CNumerics class, and φ is the volume of the actuator disc domain obtained by using the function GetDomainVolume inside the class.

SU2 offers several non-dimensional based solvers, as well as a dimensional one. (Economon, 2016) In case a non-dimensional option is used all variables including the forces should be non-dimensionalized by a reference value. For the force, the reference value is given with a name Force_Ref inside the CNumerics class.

This study assumes that there is no additional mass or heat transfer caused by blade rotation. Therefore, the source term corresponding to the first and fifth indices should be set to zero. Taking into account force scaling and non-dimensional solver options, the source term to be applied to the flow_sources.cpp file, which is a subclass of CNumerics, is given by Equation 3.52.

$$Q = \begin{pmatrix} 0 \\ \dfrac{\overrightarrow{F'}}{Force\_Ref} \\ 0 \end{pmatrix} \tag{3.52}$$

As the momentum sources are successfully implemented into equations, the next part would be to obtain the relevant numerical outputs such as thrust and power coefficients, and this computation requires a parallel computation which is discussed in the following section.

3.5.2 Parallel Performance of the Model and Numerical Outputs

One of the main advantages of SU2 software is its ability to perform parallel computations using MPI. When implementing new models, it is important to ensure that the code's performance is not negatively affected.

In the case of the CEulerSolver, where computations are performed on each node within the domain, parallelization can be achieved by distributing the nodes and their corresponding computations among multiple processors. This can be done using a built-in function in SU2 called SU2_OMP_FOR_DYN, which facilitates parallel execution of computations. SU2_OMP_FOR_DYN is a function that enables dynamic load balancing and workload distribution across processors in parallel computing.

To obtain the resultant power and thrust coefficients on the blade, parallel computation is required to some extent. This involves gathering all the resultant forces from each processor and performing the necessary computations. In SU2, this is achieved through functions such as SU2_OMP_FOR_STAT, SU2_Reduce, SU2_OMP_CRITICAL, and SU2_OMP_BARRIER. The process involves looping over each processor to sum up the total forces exerted on the blade and gathering them on a single processor, typically the master processor. Then, using the node-cell volumes, the master processor performs integration across the domain to calculate the power and thrust coefficients, consequently printing them on the screen as the solver progress.

The SU2 software includes the SU2_MPI_ERROR functionality, which is useful for generating meaningful error messages in case of issues or mistakes. It is important to create a user-friendly code that provides clear error messages when users make mistakes, such as incorrect input definitions in the configuration file. To achieve this, multiple SU2_MPI_ERROR functions have been implemented throughout the code, ensuring that users are informed about the specific details of any errors that occur.

Total computation time is measured with and without the AEDISC model inside a test model that has a total mesh size of 250,000 cells, as can be seen in Figure 3.28.

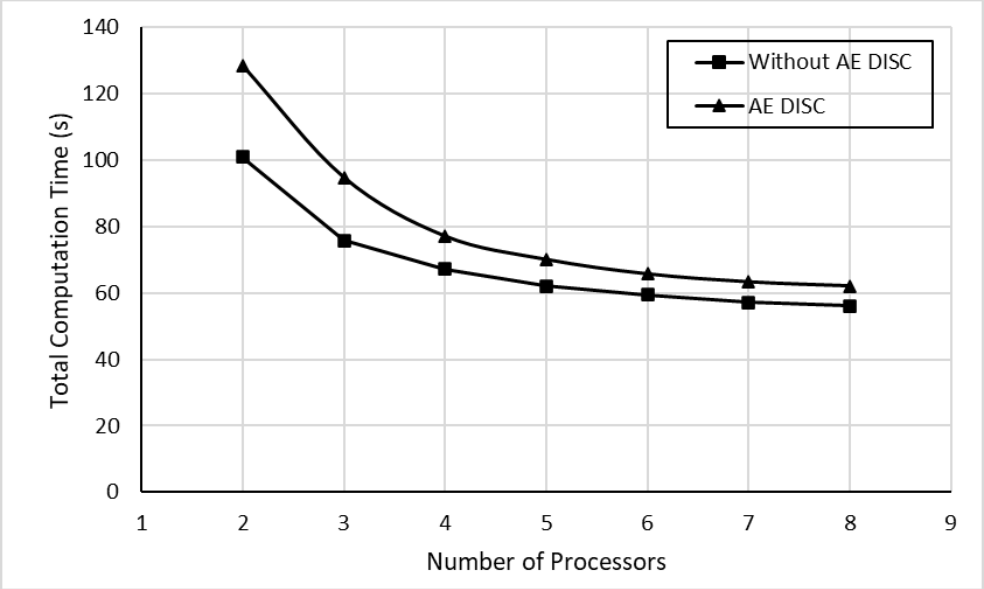

Figure 3.28. Number of processors vs total computation time in two computations with and without AEDISC enabled.

Activation of the AEDISC model inevitably leads to an increase in the total computation time. This outcome is expected since the model involves solving additional equations and a significant portion of the increase can be attributed to the interpolation methodologies employed within the AEDISC model. In each iteration, multiple equations are solved to interpolate intermediary values. Although the interpolation is implemented in its simplest form, it still poses challenges and makes the implementation of higher-order interpolation methodologies more complex.

In both computations, a similar trend is observed as they approach a converging point that is directly influenced by the mesh size and the number of processors employed. As the number of processors increases beyond a certain threshold, the communication time between processors begins to extend, limiting further acceleration of the computation. Overall, the computational time increases by approximately ten percent, which is considered acceptable in order to maintain the

accuracy of the methodology and considering the advantages of the BET-CFD hybrid approach in terms of reduction in computational resources compared with other methodologies such as rotating frame or sliding-mesh.

In the upcoming chapter, we present and compare the results obtained from the BET-CFD coupling strategy and the steady-state rotating frame approach with experimental data. The thrust and power coefficients serve as the primary indicators for evaluation. Additionally, pressure coefficient plots are generated on the blade surfaces to ensure the model delivers accurate solutions.

CHAPTER 4

RESULTS

The validation process involved the comparison of the AEDISC models results with experimental data and results obtained from the 3D rotating frame approach. Two RPM values were selected as test points, and computations were performed at various advance ratio points using both the AEDISC model and the 3D rotating frame approach. Experimental data for thrust and power coefficients were available for all these points (Brandt et al., 2023), hence comparisons with experimental results and rotating frame approach were made by using these outcomes. Additionally, a comparison of the velocity distribution in the wake region was conducted between the AEDISC and rotating frame approach. This facilitated a clearer understanding of the wake structure generated by each model.

One important factor to consider when comparing the AEDISC model and the rotating frame approach is the computational time. Figure 3.25 demonstrates a significant disparity in the number of cells utilized between the two methods. The AEDISC model employs a relatively low number of cells, approximately 76,000, comprising solely hexahedron and tetrahedral elements. Conversely, the rotating frame approach employs around 3.2 million cells, incorporating tetrahedral and prism layer elements for boundary layer resolution. Consequently, the execution time differs substantially between the two approaches. In the case of AEDISC, each run is completed in a mere 1.58 minutes, while the rotating frame approach necessitates 102 minutes for each run to conclude with 2000 iterations on an 8-core machine.

4.1 Comparison of Thrust and Power Coefficients

Thrust and power coefficients obtained from each study are compared with experimental data and rotating frame approach. Thrust and power coefficients represent the forces occurring on the blade, and they can be also used to anticipate the wake behind rotating parts at some extend. In Figure 4.1 change of thrust coefficient, power coefficient and efficiency factor with respect to advance ratio is presented in 3000 RPM operating condition.

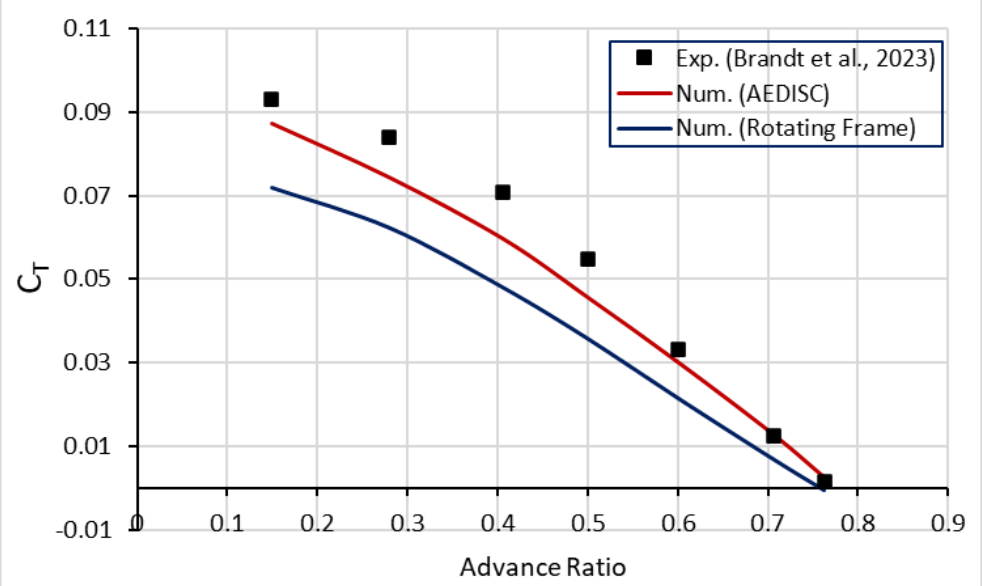

(a) Change of thrust coefficient

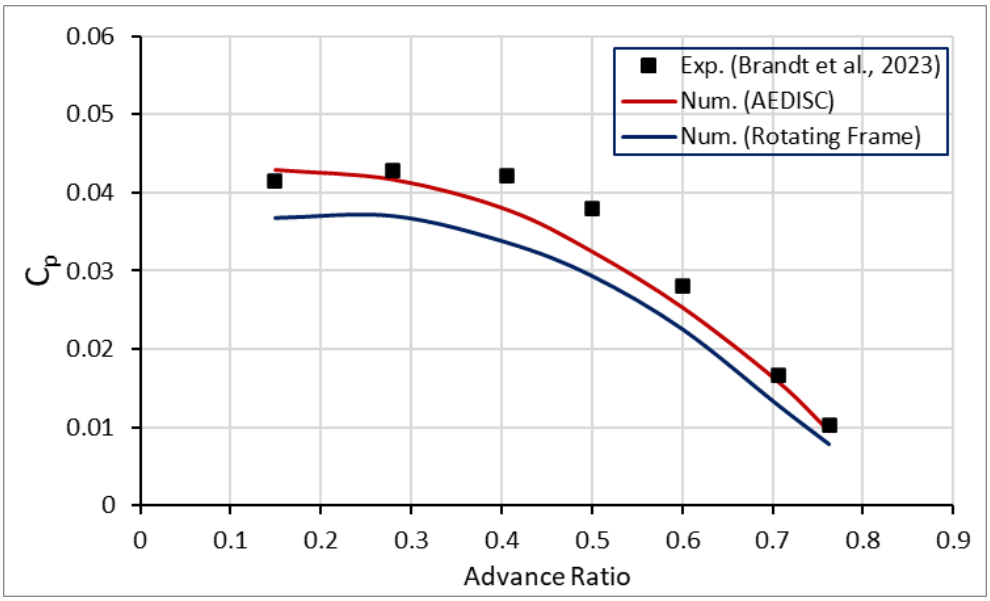

(b) Change of power coefficient

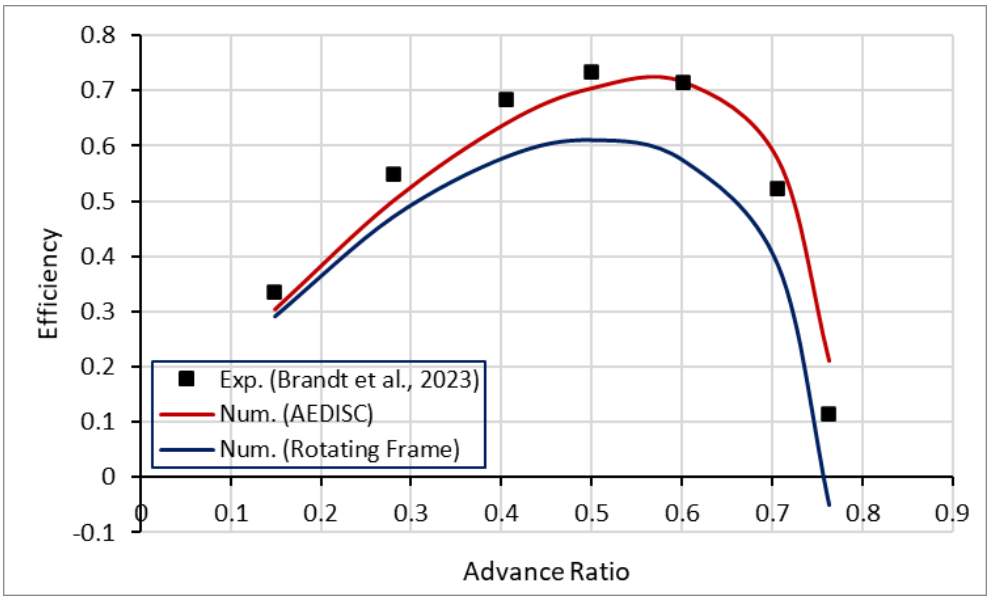

(c) Change of efficiency factor

Figure 4.1. (a) Thrust coefficient, (b) Power coefficient and (c) Efficiency factor variation with respect to advance ratio of APC 19x12 thin electric propeller at 3000 rpm.

In Figure 4.1, the trends such as slopes shown in the experimental data are captured by both methods that aligns with studies from Oktay et al. (2020). Consistently

decreasing thrust coefficient values are observed as the advance ratio decreases, while the power coefficient remains mostly constant between advance ratios 0.2 and 0.4 before further decreasing. Changes in the effective angle of attack as the advance ratio increases primarily contribute to this decrease in thrust coefficient. The decrease in lift coefficient, which significantly affects the thrust coefficient, is associated with the decrease in the effective angle of attack. The constancy in power coefficients between advance ratios 0.2 and 0.4 can be explained by the dominance of pressure drag components in these regions with higher effective angles of attack that matched with studies of Silvestre et al., (2015). However, as the advance ratio and effective angle of attack decrease, the power coefficient decreases due to reductions in both pressure and friction drags, as well as a decrease in the lift coefficient. Both methods exhibit a similar trend in the efficiency factor, calculated based on the thrust and power coefficients. A peak is observed in both coefficients at approximately the same advance ratio, although noticeable differences between the two methods exist.

In terms of accuracy, the overall error between the AEDISC model and experimental data was found to be lower than the overall error between the rotating frame approach and experimental data as stated in Table 4.1.

Table 4.1 Average error obtained from AEDISC model and rotating frame approach comparing with experimental data at 3000 RPM.

Method	Average error, ε_{C_T}	Average error, ε_{C_P}	Average error, ε_{C_n}
AEDISC	9.02%	6.46%	2.99%
Rotating Frame	32.24%	18.54%	17.28%

The maximum absolute relative percentage error between the AEDISC and experimental results was found to be $\varepsilon_{C_T} = 16.52\%$ at J=0.5, $\varepsilon_{C_P} = 14.33\%$ at $J = 0.5$, and $\varepsilon_n = 10.09\%$ at $J = 0.706$. The maximum absolute relative percentage error between the rotating frame and experimental results was found to

be $\varepsilon_{C_T} = 42.94\%$ at $J = 0.706$, $\varepsilon_{C_P} = 22.67\%$ at $J = 0.5$, and $\varepsilon_n = 26.18\%$ at $J = 0.706$. Average absolute relative percentage error in AEDISC model comparing with experimental data was found to be $\varepsilon_{C_T} = 9.02\%$, $\varepsilon_{C_P} = 6.46\%$, and $\varepsilon_n = 2.99\%$, and the average absolute relative percentage error in rotating frame approach comparing with experimental data was found to be $\varepsilon_{C_T} = 32.24\%$, $\varepsilon_{C_P} = 18.54\%$, and $\varepsilon_n = 17.28\%$. Maximum and average errors being lower in AEDISC model can be attributed to the high-quality data obtained from the airfoil database and the assumption of an infinite number of blades inside the domain, enabling accurate consideration of blade forces at each node. The absolute error in both methodologies comparing with the experimental data was found to be lower at higher advanced ratios. This could be explained by the decrease in effective angle of attack at higher advanced ratios, which cause lower forces on blade sections.

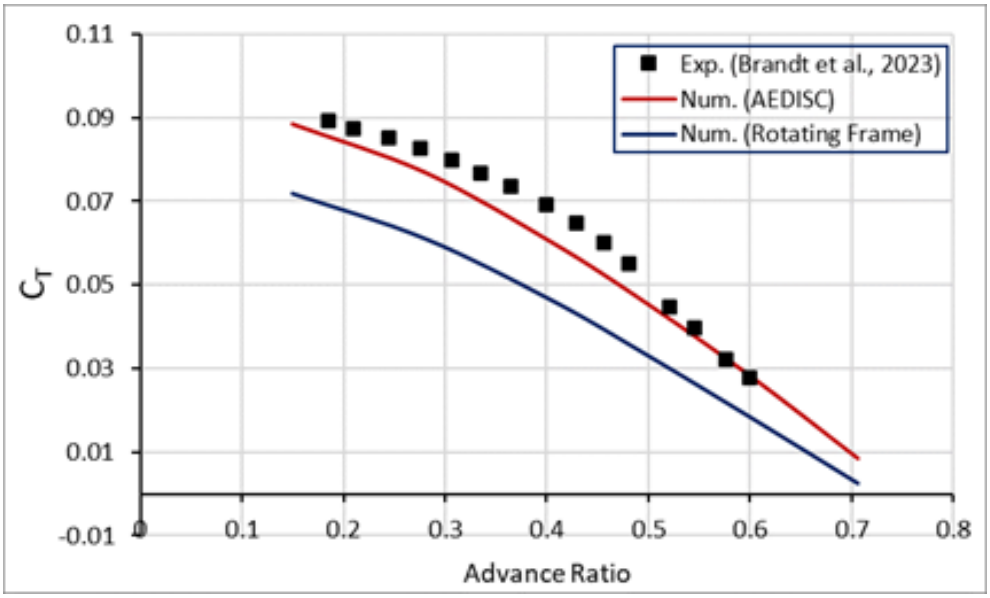

(a) Change of thrust coefficient

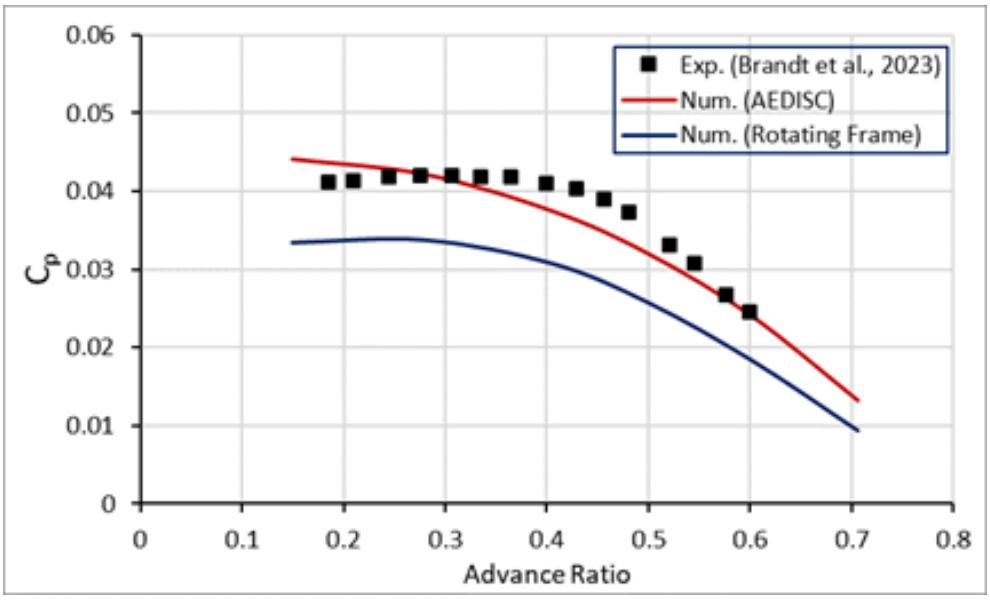

(b) Change of power coefficient

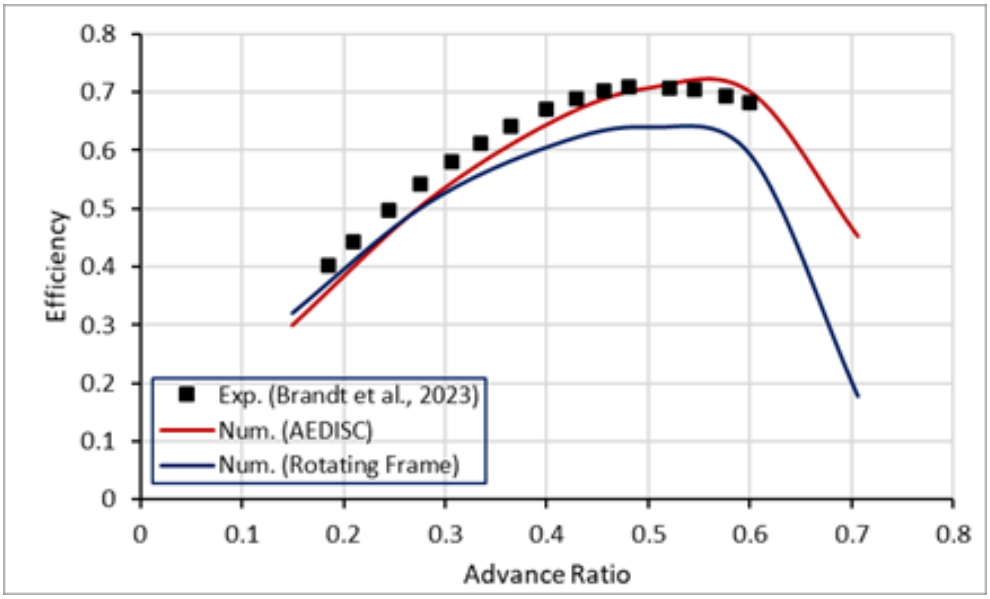

(c) Change of efficiency factor

Figure 4.2 (a) Thrust coefficient, (b) Power coefficient and (c) Efficiency factor variation with respect to advance ratio of APC 19x12 thin electric propeller at 2500 rpm.

The thrust coefficient, the power coefficient, and the efficiency factor for various advance ratios at RPM = 2500, as depicted in Figure 4.2, exhibit similar patterns to those presented in Figure 4.1. AEDISC model at this rpm presents lower relative percentage error comparing with experimental data, than the case with RPM = 3000. Average relative percentage error decreases from 9.02% to 6.86% in thrust coefficients, from 6.46% to 2.01% in power coefficients, and from 2.99% to 2.69% in efficiency factor within AEDISC model as depicted in Table 4.2.

Table 4.2 Average error obtained from AEDISC model comparing with experimental data at 2500 RPM and 3000 RPM.

RPM	Average error, ε_{C_T}	Average error, ε_{C_P}	Average error, ε_{C_n}
2000	6.86%	2.01%	2.69%
3000	9.02%	6.46%	2.99%

The absolute error in values obtained by both methods at high advance ratios comparing with experimental data indicates their success in situations where the flow remains attached to the blade surfaces, resulting from a low effective angle of attack, that matches with the findings of Shamsia et al. (2017).

Another common observation in Figures 4.1 and 4.2 is that the percentage error in thrust and power coefficients between AE DISC model tends to get smaller as the advanced ratio is reduced further from 0.406. Absolute relative percentage errors at $J = 0.406$ and 3000 RPM are found to be $\varepsilon_{C_T} = 15.74\%$, $\varepsilon_{C_P} = 10.23\%$, and they are reduced to $\varepsilon_{C_T} = 6.07\%$, $\varepsilon_{C_P} = 3.34\%$ at $J = 0.149$. Similarly in 2500 rpm, absolute relative percentage errors at $J = 0.406$ are found to be $\varepsilon_{C_T} = 12.97\%$, $\varepsilon_{C_P} = 9.83\%$, and they are reduced to $\varepsilon_{C_T} = 3.36\%$, $\varepsilon_{C_P} = 8.22\%$ at $J = 0.149$. This behaviour could potentially be attributed to the utilization of the stall delay model in the aerodynamic database. The stall delay model has a greater influence at lower advance ratios, where the effective angle of attack is relatively higher. Figure 3.23 demonstrates that the stall delay model primarily affects

regions where the angle of attack is equal to or greater than 6 for the specific airfoil section. Although the specifics may vary for each section analysis, the general trend is to increase the lift coefficient at higher angles of attack to delay the occurrence of stall.

Figure 4.3 illustrates the variations in thrust coefficient, power coefficient, and efficiency factor with respect to the advance ratio in the 3000 RPM operating condition. The data presented in this figure specifically pertains to the AEDISC model but showcases two different airfoil databases: one including the stall delay model and another without it.

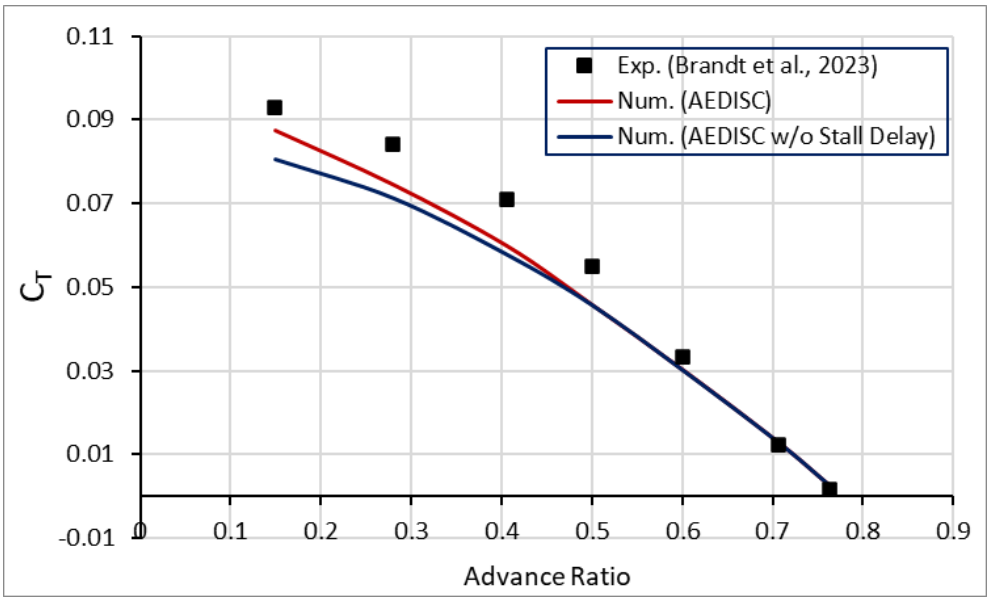

(a) Change of thrust coefficient

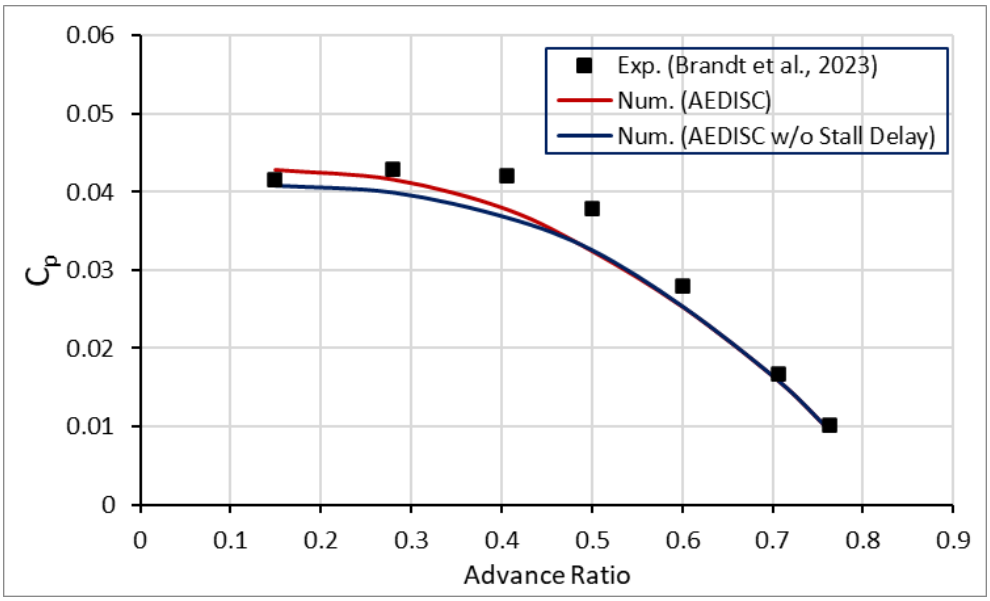

(b) Change of power coefficient

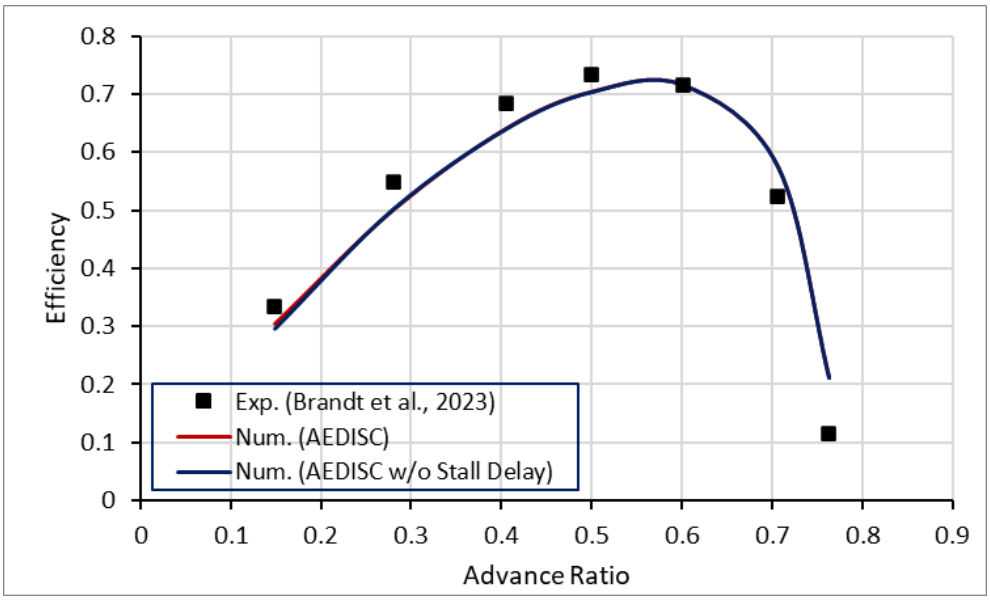

(c) Change of efficiency factor

Figure 4.3. (a) Thrust coefficient, (b) Power coefficient and (c) Efficiency factor variation with respect to advance ratio of APC 19x12 thin electric propeller at 3000 rpm with and without the stall delay model.

In Figure 4.3, it can be observed that, in terms of thrust coefficient, the absolute relative percentage error is reduced by 2.9% at $J = 0.406$, 3.62% at $J = 0.28$ and

7.18% at $J = 0.149$. In terms of power coefficient, this reduction can be found as 2.73% at $J = 0.406$, 4.14% at $J = 0.28$ and 5.14% at $J = 0.149$ when the stall delay model is employed to the aerodynamic database. The efficiency factor, on the other hand, remains relatively unaffected, with a slight increase observed in the lowest advance ratios, although this increase is not significant.

Table 4.3 Percentage of error reduced when a stall delay model is employed to AEDISC model comparing with experimental data.

Advance Ratio	Error Reduction, ε_{C_T}	Error Reduction, ε_{C_P}
0.149	7.18%	5.14%
0.280	3.62%	4.14%
0.406	2.90%	2.73%

Overall results in comparisons between the AEDISC, rotating frame and experimental data proves that the errors in AEDISC model compared to experimental data is lower than the ones obtained with rotating frame and experimental data comparisons. The fact that the overall error is reduced in AEDISC model when the rpm is reduced from 3000 to 2500 proves that the aerodynamic database and the model is applicable to varying operating conditions. Another important finding is the significance of the quality of the aerodynamic database. The reduction in error values when the stall delay model is employed is the proof of the significance of the aerodynamic data, as well as the necessity of the 3D correction methodologies.

4.2 Comparison of Pressure Distribution on Blade Sections

In addition to examining thrust and power coefficients, it is also important to understand the forces generated by the AEDISC model and assess the accuracy of the resulting flow quantities. To determine the model's applicability in terms of thrust and power coefficients, it is necessary to conduct further investigations into

the forces applied to the blade. To gain insights into the differences in flow coefficients between the two methodologies discussed earlier (AEDISC and rotating frame), we will examine the pressure values on blade sections in each approach. This will involve applying a reverse transformation to match the operational conditions.

In this section, the comparison between the AEDISC model and the rotating frame approach serves as the primary means of understanding the model's performance in capturing the flow characteristics in only RPM = 3000 condition. Since the experimental data does not provide specific information about the solution fields other than thrust and power coefficients, the comparison between the two models allows for insights into the suitability and accuracy of the AEDISC model.

In the case of the 3D CFD rotating frame approach, we will generate three slices on the blade surfaces at specific locations: r/R = 0.2, r/R = 0.5, and r/R = 0.5. By doing so, we can obtain the pressure distribution on these slices. However, obtaining the pressure distribution in the AEDISC model is not as straightforward since it does not involve actual blades in the simulation. Nonetheless, we can extract the resultant flow quantities at each node that are Mach number, Reynolds number and angle of attack, from the source code corresponding to the locations r/R = 0.2, r/R = 0.5, and r/R = 0.5. Then, we can perform 2D airfoil simulations to obtain the pressure distributions. The main objective here is to compare the effective angles of attack between the two methodologies, as we do not have precise information about the induced and effective angles of attack in the rotating frame simulations.

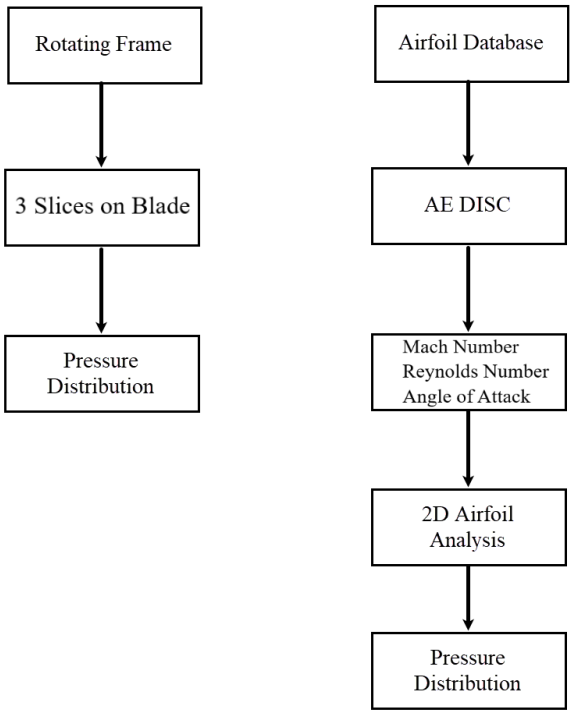

Figure 4.4. Reverse transformation to match operating conditions in rotating frame and AEDISC.

Figure 4.4. shows the process to obtain the pressure distribution in three different sections of the blade in both methodologies. Please note that the comparisons are made by using the gauge pressure values, instead of pressure coefficients. The purpose is to reflect the order of magnitude of the forces occurring on the blades.

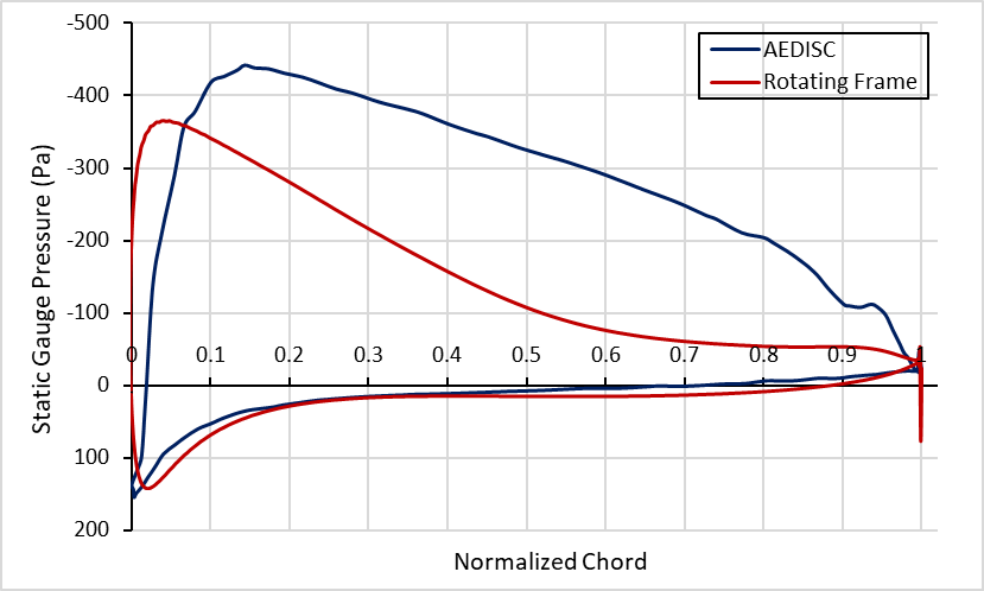

(a) Pressure distribution over section r/R = 0.2

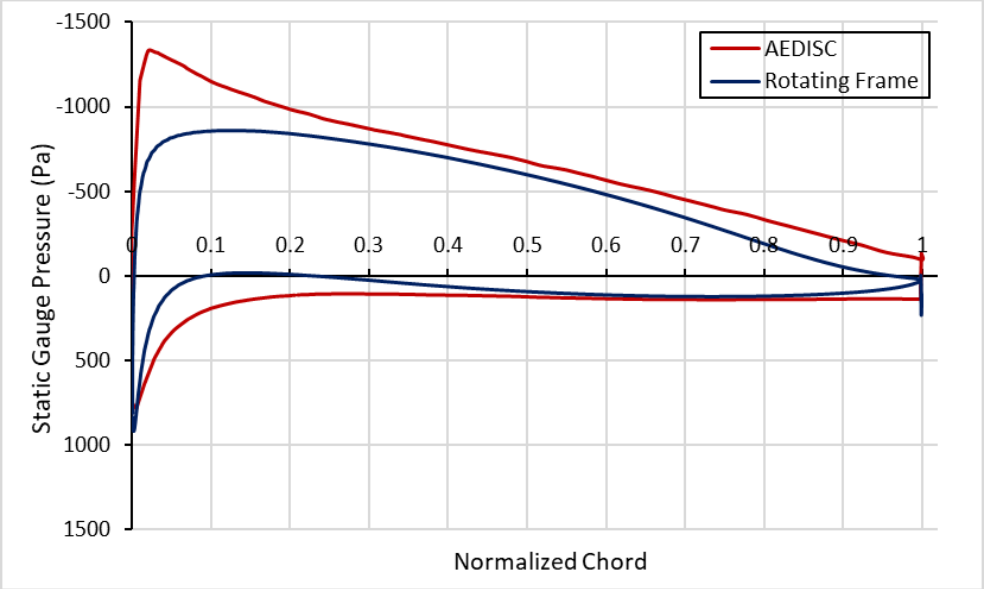

(b) Pressure distribution over section r/R = 0.5

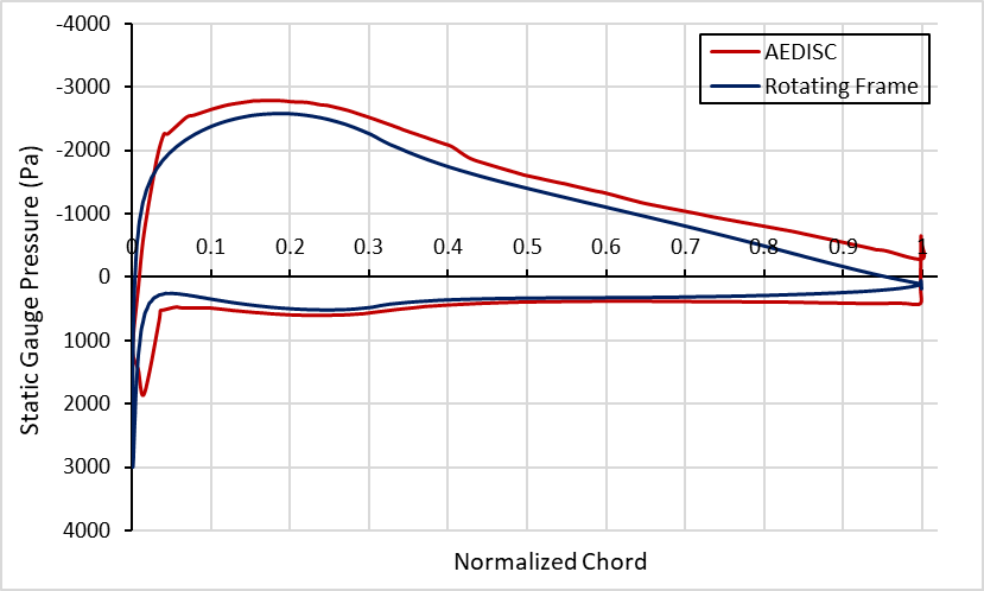

(c) Pressure distribution over section r/R = 0.9

Figure 4.5. Rotating frame and AEDISC Pressure distribution over normalized chord of three different sections on the blade at advance ratio = 0.28

In Figure 4.5, the pressure distribution over three sections of the blades in each methodology are depicted and compared. The most noticeable difference between the two methodologies is observed near the hub, specifically at r/R = 0.2. One reason for the high difference in this region is the low dynamic pressure caused by the lower velocity near the hub. As a result, the difference becomes more apparent compared to other regions. Another possible reason for the clear difference near the hub is related to the geometry of the hub itself. In the rotating frame approach, the computations include a hub and spinner parts, and although their effects are removed from the thrust and power coefficients, they may still influence the flow pattern near these regions (Matveev et al., 2023).

Examining the pressure distribution in other sections at an advance ratio of 0.28, it is evident that these sections experience a higher angle of attack in the AEDISC model compared to the rotating frame approach. The peak near the leading edge, which creates a high suction zone, can be clearly observed in both Figure 4.4.b and Figure 4.4.c. This observation aligns with our expectations, as we anticipate the

AEDISC model to generate higher pressure forces in general, based on the thrust and power coefficient results (Figure 4.1).

The overall trend of increasing pressure as we move from the hub to the tip is another expected behavior, as higher dynamic pressures near the tip regions result in greater pressure differences. Although the flow speed is highest near the tip regions, we do not observe a peak behavior in pressure similar to the one at r/R = 0.5. This is because blade tips are usually less twisted or pitched compared to the middle section, as they are designed to accommodate higher velocities. This optimization of the blade shape for different rotation rate conditions explains the absence of a peak pressure behavior near the tip.

To provide a comprehensive view, the pressure distributions in each section are further examined at two additional advance ratios: 0.5 and 0.768. Figure 4.6 displays the pressure distribution over the blade for three different sections, comparing the results obtained from the AEDISC model and the rotating frame approach at advance ratio 0.5.

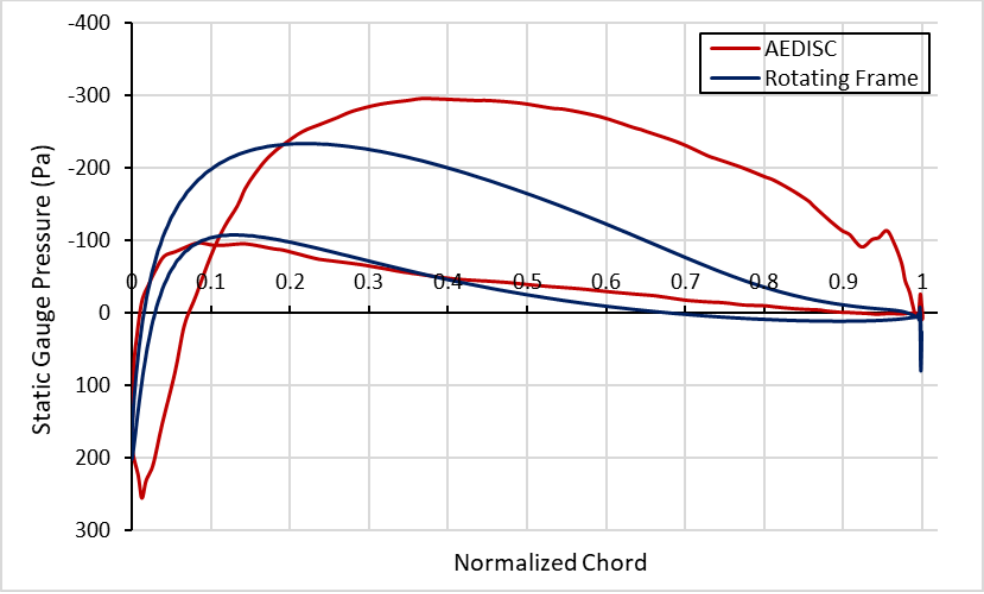

(a) Pressure distribution over section r/R = 0.2

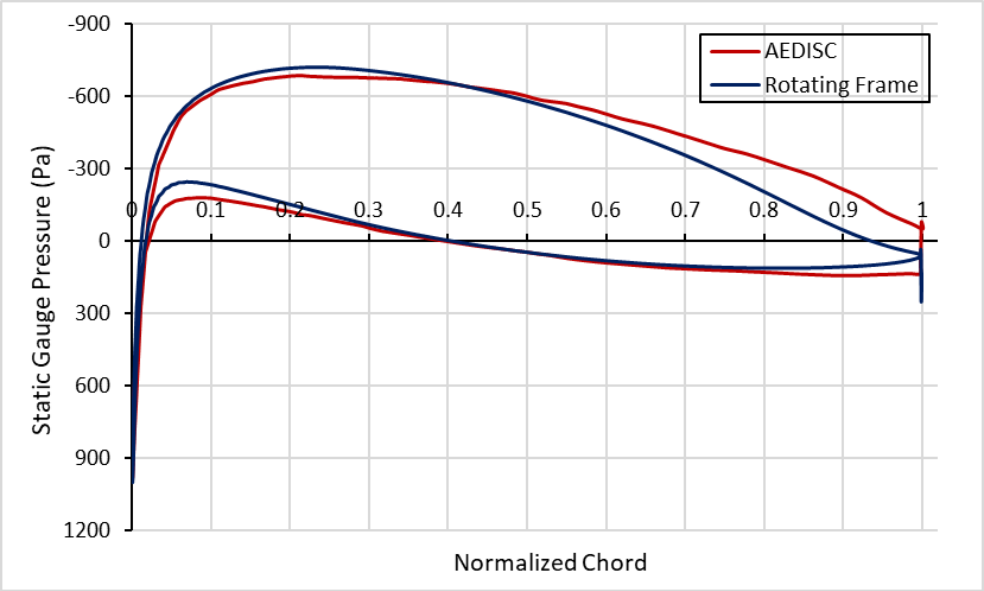

(b) Pressure distribution over section r/R = 0.5

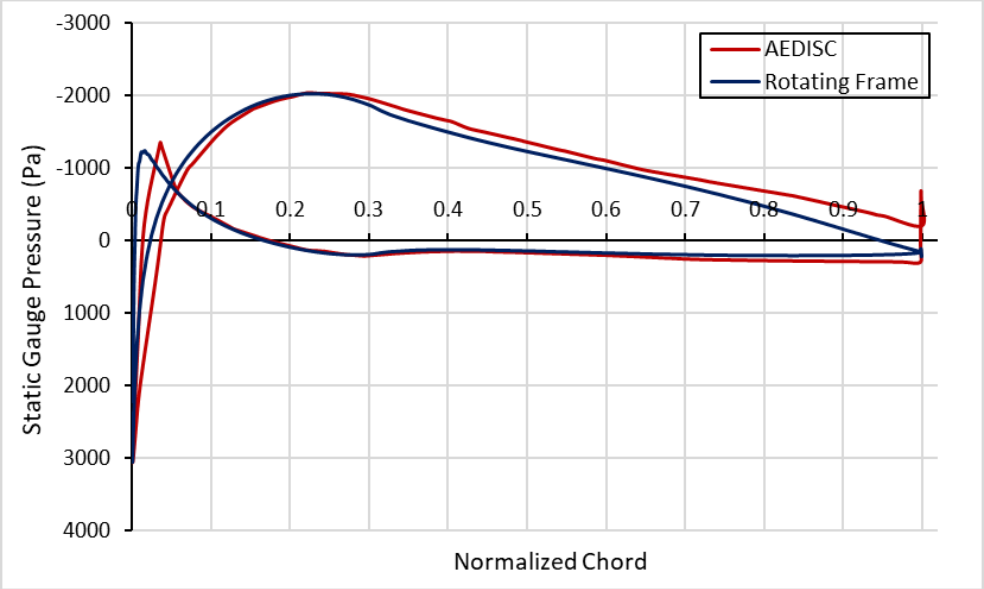

(c) Pressure distribution over section r/R = 0.9

Figure 4.6. Rotating frame and AEDISC Pressure distribution over normalized chord of three different sections on the blade at advance ratio = 0.5

In the case of the advance ratio 0.5, the comments made for the advance ratio 0.28 case, specific to each section, remain valid. However, the notable difference lies in

the magnitude of the pressure values. As the advance ratio increases, the effective angle of attack experienced by the blade sections decreases due to the higher freestream velocity.

Similar to the advance ratio 0.28 case, we observe a similar behavior near the hub in the advance ratio 0.5 case, where the most significant difference between the two methodologies is observed. Moving towards the tip section of the blade, we notice that the pressure distributions start to align further.

Another noteworthy observation from Figure 4.6.b and Figure 4.6.c is that the suction on the upper surface of the airfoil is more pronounced in the AEDISC model compared to the rotating frame approach. This could potentially be explained by the delay of separation caused by the implementation of the stall delay model.

In the last case, where the advance ratio is increased to 0.768, representing the highest freestream velocity, the pressure distribution on three blade sections obtained from each methodology is displayed in Figure 4.7. This advance ratio corresponds to a significantly reduced effective angle of attack experienced by the blade sections due to the much higher freestream velocity.

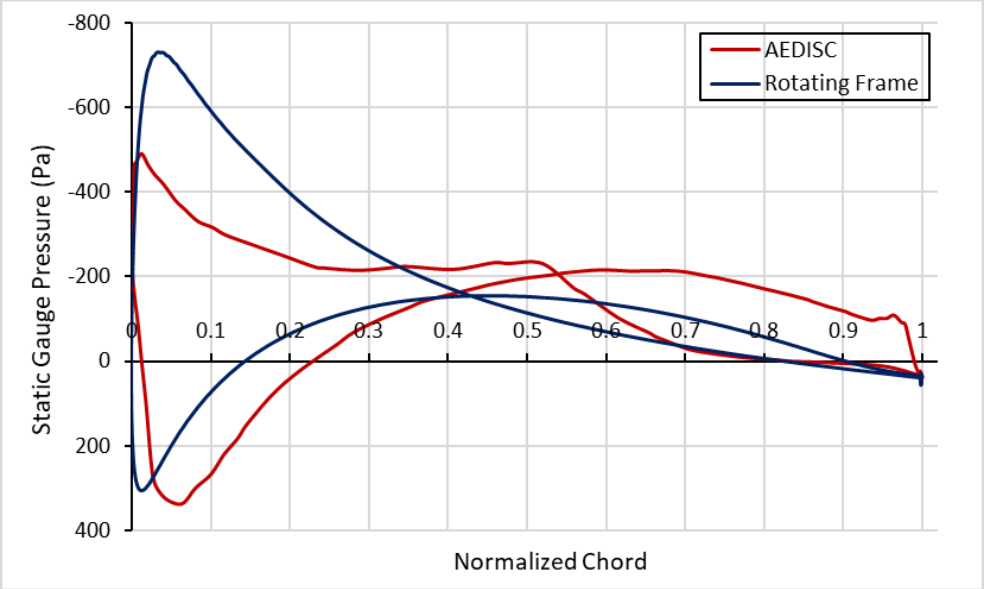

(a) Pressure distribution over section r/R = 0.2

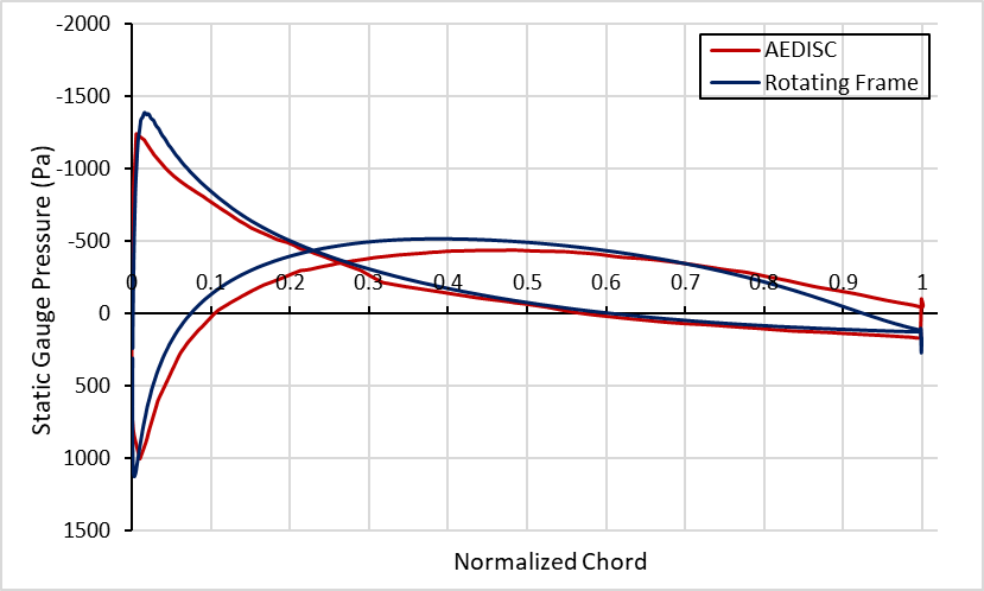

(b) Pressure distribution over section r/R = 0.5

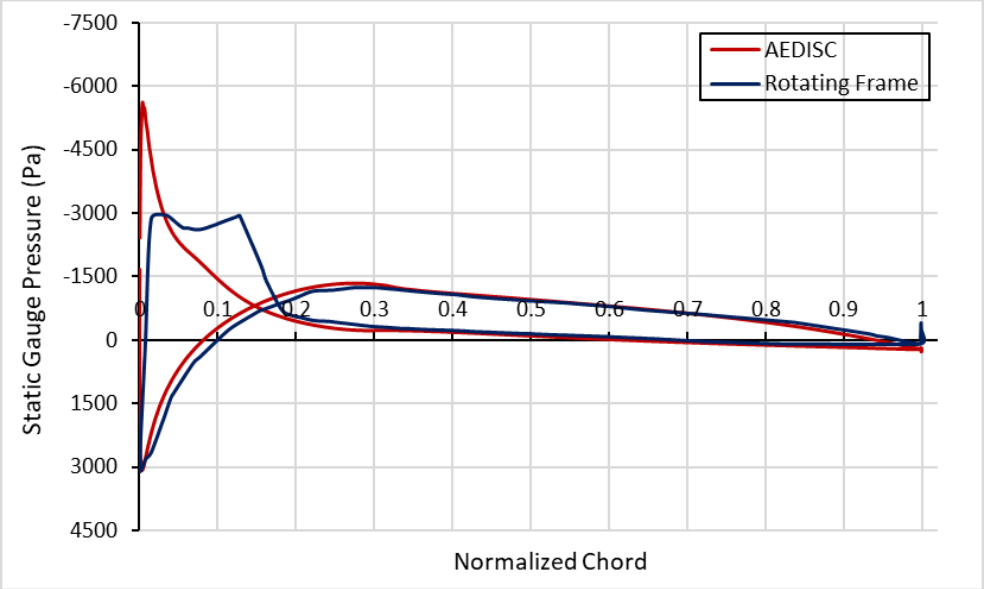

(c) Pressure distribution over section r/R = 0.9

Figure 4.7. Rotating frame and AEDISC Pressure distribution over normalized chord of three different sections on the blade at advance ratio = 0.768

In the case of the 0.768 advance ratio, the freestream velocity is at its highest, resulting in the highest dynamic pressure. As a result, we observe the highest

pressure peaks in this case, as shown in Figure 4.7.c. However, it's important to note that the pressure values decrease and approach zero after the peak, indicating a significant reduction in the effective angle of attack in all three sections. In fact, the effective angle of attack is nearly at angles of zero lift in Figure 4.7a and even exhibits negative lift in Figure 4.7.c. The highest-pressure peaks occur due to the curvature of the leading edges of these sections, which gradually stabilize to smaller pressure values as they approach the trailing edge. This behavior is observed in both methodologies and aligns with our expectations based on the thrust and power coefficients (Figure 4.1). Considering the experimental data and the previous results shown in Figure 4.1, we can conclude that the obtained low flow coefficients are reasonable due to the low angle of attacks in this operating condition.

In summary, the findings from the studies conducted in this section show that the overall behavior in pressure distributions aligns with the observations made for thrust and power coefficients. The general trends in both models, such as the decrease in pressure forces with increasing advance ratio, the increase in pressure peaks with increasing advance ratio, the pressure loadings on the blade moving from the hub to the tip, the highest angle of attacks occurring near the middle section of the blade, and the delay in separation due to the stall delay model in AEDISC model, are successfully captured. This serves as further validation for the implemented actuator disc model in comparison to the rotating frame approach.

4.3 Comparison of Downstream Velocities

One of the main motivations for the addition of a new actuator disc model to SU2 software was the study of flow patterns downstream of rotating components, such as aircraft propeller slipstream effects. To assess the performance of the AEDISC model, a comparison of velocities downstream of the rotating component was conducted using two types of lines in both the AEDISC model and the rotating

frame approach. These comparisons were performed at an rpm value of 3000, with three different advance ratios ($J = 0.28, 0.5, \text{and } 0.768$).

The lines employed for plotting the downstream velocities are depicted in Figure 4.8. A y-line was generated, positioned behind the rotating component and parallel to the y-axis, with a distance of 0.1 m. Similarly, a z-line was created, located behind the rotating component and parallel to the z-axis, also at a distance of 0.1 m. Velocities in the x-direction were recorded on both lines to analyze the axial progression of the flow behind the rotating component by using the solution fields from both methodologies: AEDISC and rotating frame. On the z-line, velocities in the y-direction were plotted, while on the y-line, velocities in the z-direction were plotted, enabling examination of the tangential components of the flow. In an ideal operational scenario for rotating components, it would be expected that velocities in the x-direction on both lines would be similar due to the movement of the propeller. Likewise, the velocity in the y-direction on the z-line and the velocity in the z-direction on the y-line would be expected to be as similar as possible. In other words, flow is expected to be almost axisymmetric behind the rotating component. (Stergiannis et al., 2016)

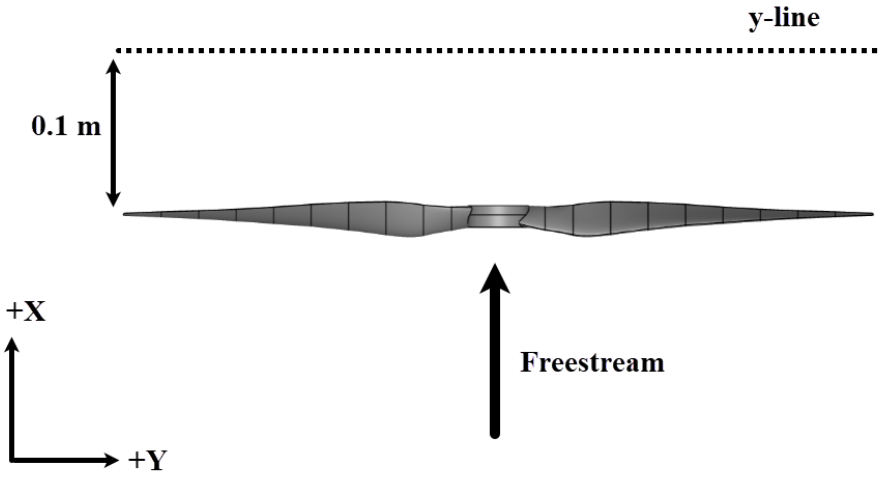

(a)

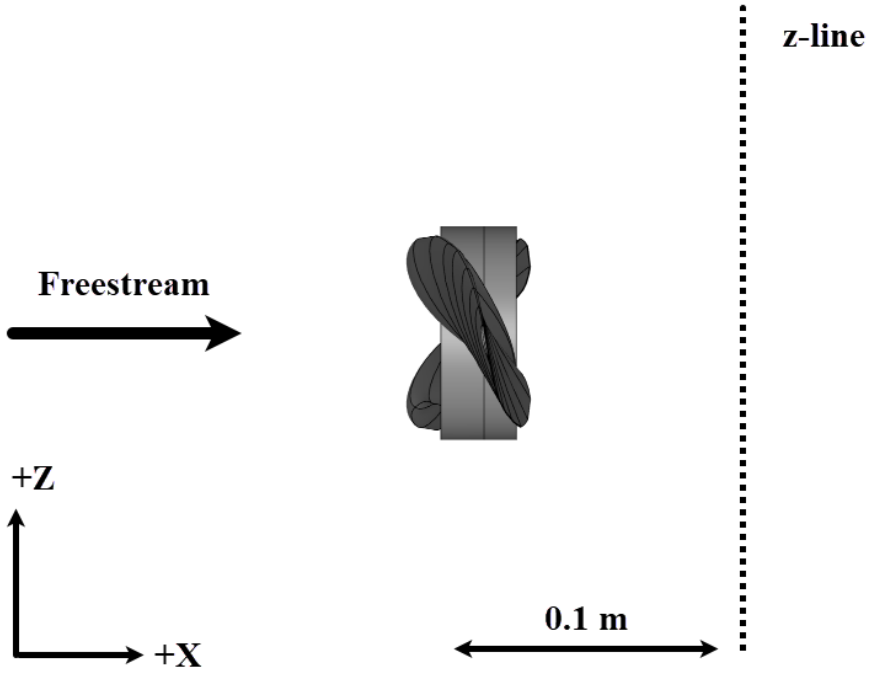

(b)

Figure 4.8. Definition of the (a) z-line and (b) y-line (highlighted in dashed lines) that are used to plot velocities, located behind the rotating component.

Since the test case is a propeller one, an overall increase in the forward velocities downstream of the propeller is anticipated as depicted by Posa et al. (2021). Additionally, a swirling motion of the velocity caused by the tangential forces acting on the blade sections is expected. (Posa et al., 2021) In Figure 4.9, the velocity components in the x, y, and z directions along z-line (see Figure 4.8a) and y-line (see Figure 4.8b) at an advance ratio of 0.28 are examined.

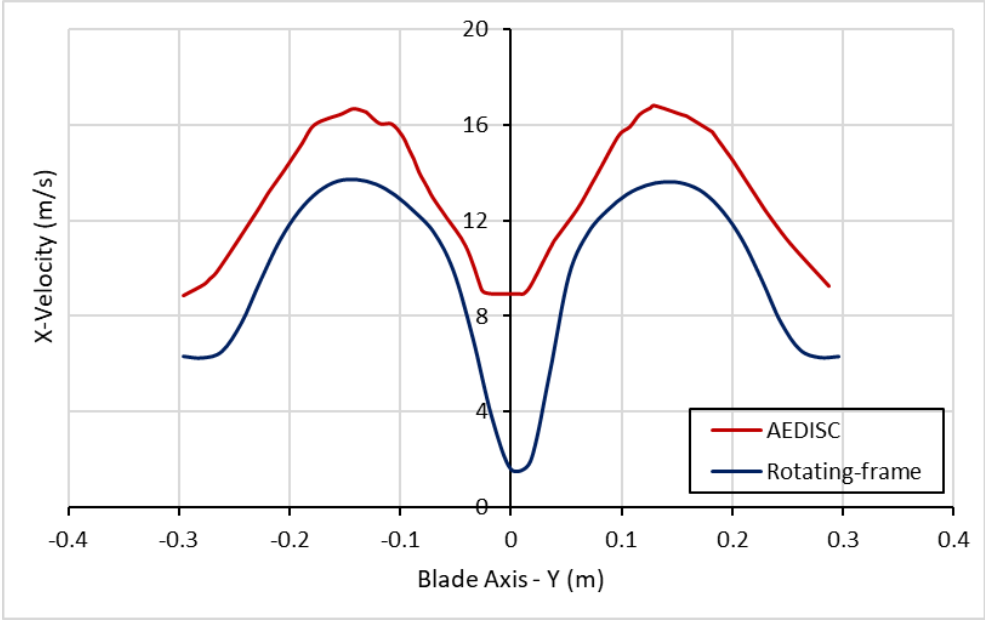

(a) x-velocity on a line aligned in y-axis

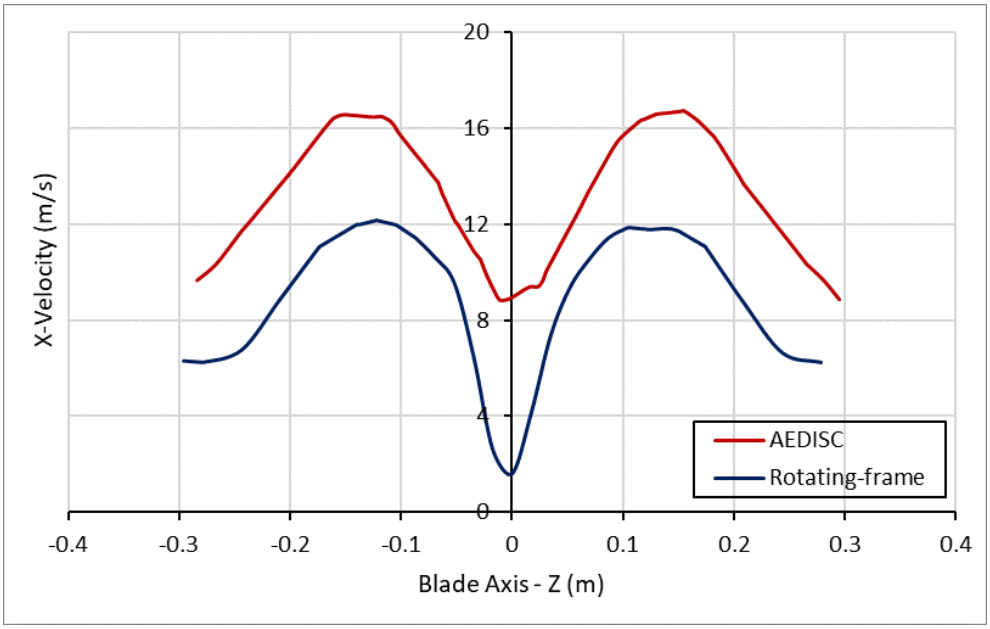

(b) x-velocity on a line aligned in z-axis

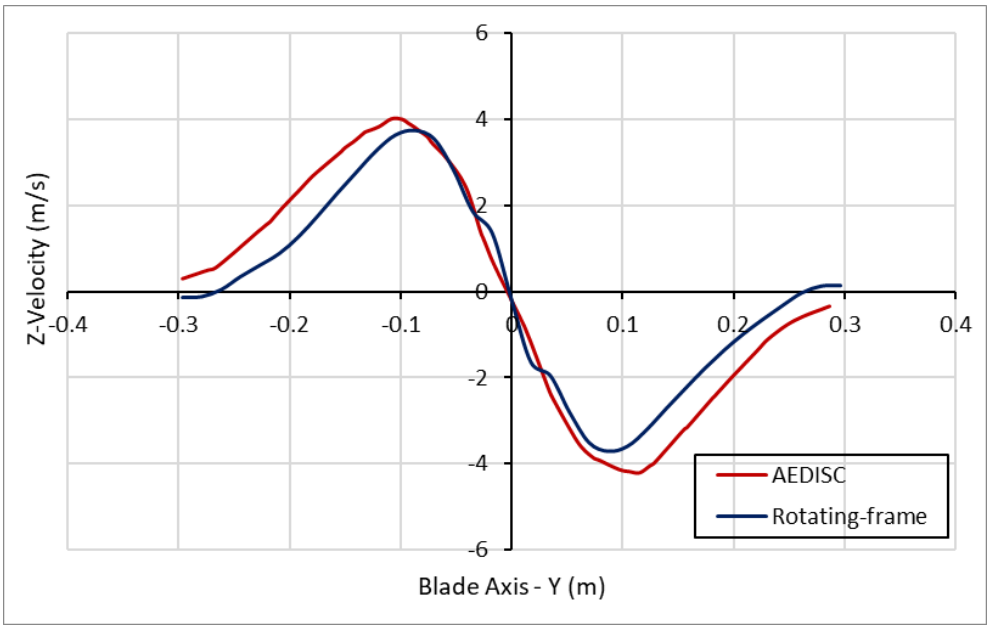

(c) z-velocity on a line aligned in y-axis

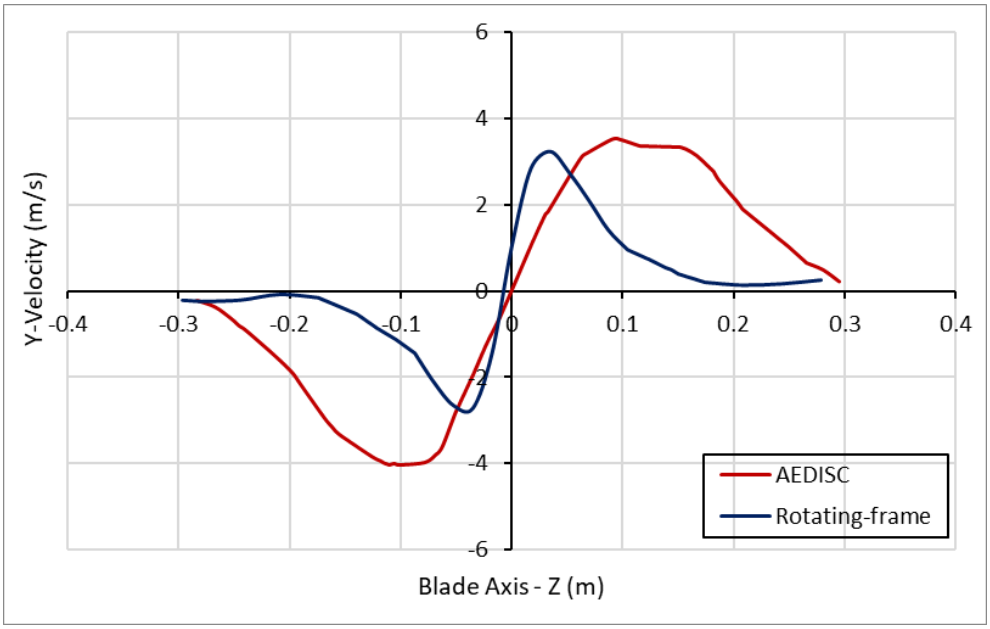

(d) y-velocity on a line aligned in z-axis

Figure 4.9 (a) x velocity along y-line, (b) x velocity along z-line and (c) z velocity along y-line and (d) z velocity along z-line at 0.1 m downstream of the Rotating Component at advance ratio of 0.28 and RPM = 3000.

In Figure 4.9a, the velocity in x direction can be seen as accelerated from the freestream velocity further in both methodologies AEDISC and rotating frame. However, the AEDISC methodology exhibits a higher velocity increase compared to the rotating frame approach. The maximum velocity plotted on the y-line behind the propeller in AEDISC is obtained as 16.82 m/s, whereas in rotating frame it is obtained as 13.71 m/s. This observation aligns with the expectations derived from the thrust and power coefficients presented in Figure 4.1. Given the higher thrust coefficient, a greater downstream acceleration is expected in the AEDISC model.

The differences between the two methodologies become apparent when comparing Figure 4.9a and Figure 4.9b. In an ideal scenario as previously mentioned, it is expected that the velocity profiles on both lines would be similar or identical, as the propeller loads are evenly distributed across sections located at the same radius when the freestream velocity is fully axial, as suggested by Di Mascio et al. (2014). On the z-line, the maximum velocity in x direction is obtained as 16.75 m/s in AEDISC, and 12.18 m/s in rotating frame approach. A relative difference can be defined based on the expected axisymmetric outcome between the maximum velocities on y and z line. The absolute relative percentage difference in AEDISC model then becomes, $\varepsilon_{V_{max}} = 0.42\%$, and it becomes $\varepsilon_{V_{max}} = 11.61\%$ in rotating frame. This discrepancy in rotating frame approach is attributed to the assumption of a frozen rotor scenario assumed in rotating frame approach, that aligns with the findings of Stergiannis et al. (2016). Based on the solution fields from the rotating frame, the velocity in x direction plotted on y line demonstrate higher values than the ones plotted on the z line. This is due to frozen rotor assumption in rotating frame. The forces exerted in y line direction is higher since the propeller is aligned in y direction as well. Hence the difference in velocities in x direction between rotating frame approach and AEDISC approach is higher on the y line. Specifically, the maximum velocity in x direction difference between two methodologies is 3.11 m/s on the y line, whereas it's 4.57 m/s on the z line. Developed x-velocity field in the AEDISC model demonstrates an almost axisymmetric behavior when comparing axial velocities on both lines.

Similar observations can be made when comparing the tangential velocities on both the y-line and z-line using both methodologies in Figure 4.9c and 4.9d. The overall discrepancies between the two models can be justified by the difference in power coefficients mostly presented in Figure 4.1b, since the effect of the power coefficient is mostly in tangential direction. However, the disparity in tangential velocities on the y-line and z-line, which contribute to the swirling motion behind the rotating component, is more pronounced in the rotating frame approach.

In Figure 4.9c, where the tangential velocities are plotted along the y-line, the difference in maximum tangential velocity is obtained as 0.265 m/s. The difference in tangential velocities becomes even less near the hub region. This suggests that the hub has minimal impact on the simulation when the advance ratios are relatively low. When comparing the tangential velocities plotted on the z-line in Figure 4.9c and Figure 4.9d, it can be seen that the maximum tangential velocity obtained from rotating frame approach is reduced from 3.74 m/s to 3.22 m/s, which results in an absolute relative percentage difference of $\varepsilon_{V_{max}} = 13.9\%$. The axisymmetric behaviour in AEDISC model is again proved by obtaining an absolute relative percentage difference in maximum tangential velocities of $\varepsilon_{V_{max}} = 0.876\%$.

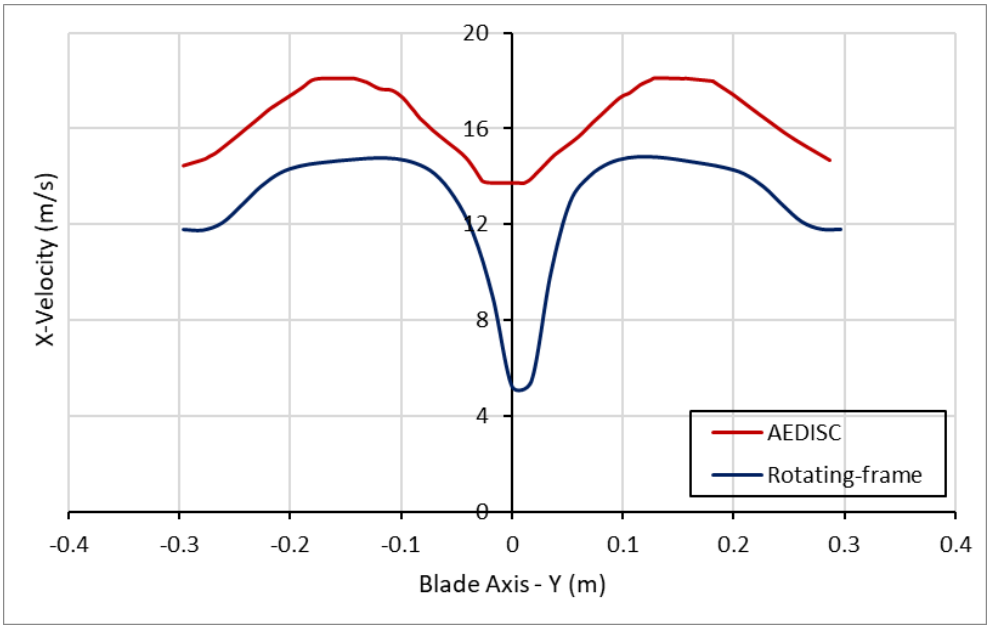

(a) x-velocity on a line aligned in y-axis

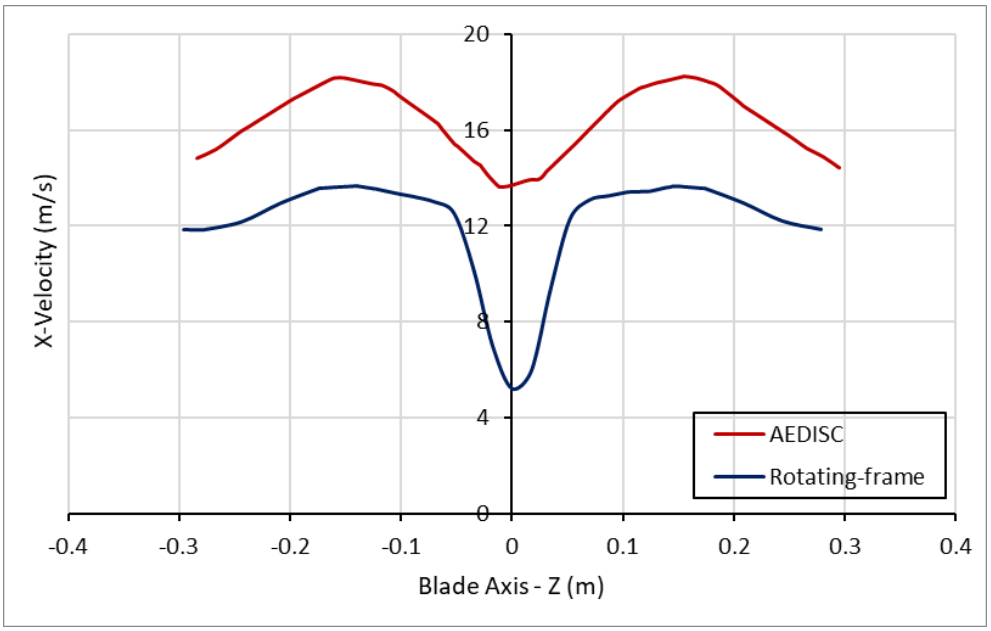

(b) x-velocity on a line aligned in z-axis

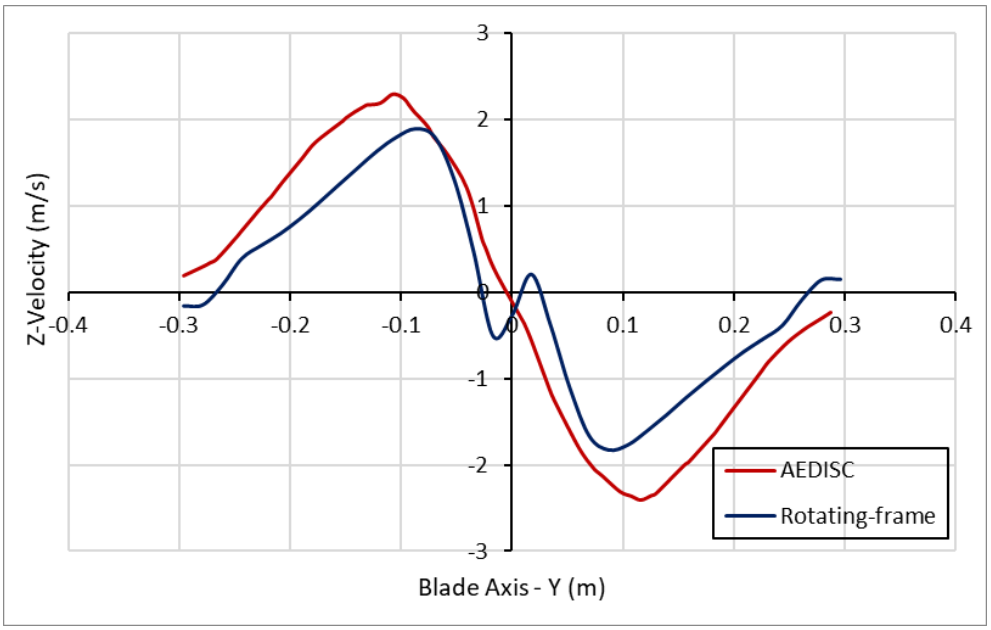

(c) z-velocity on a line aligned in y-axis

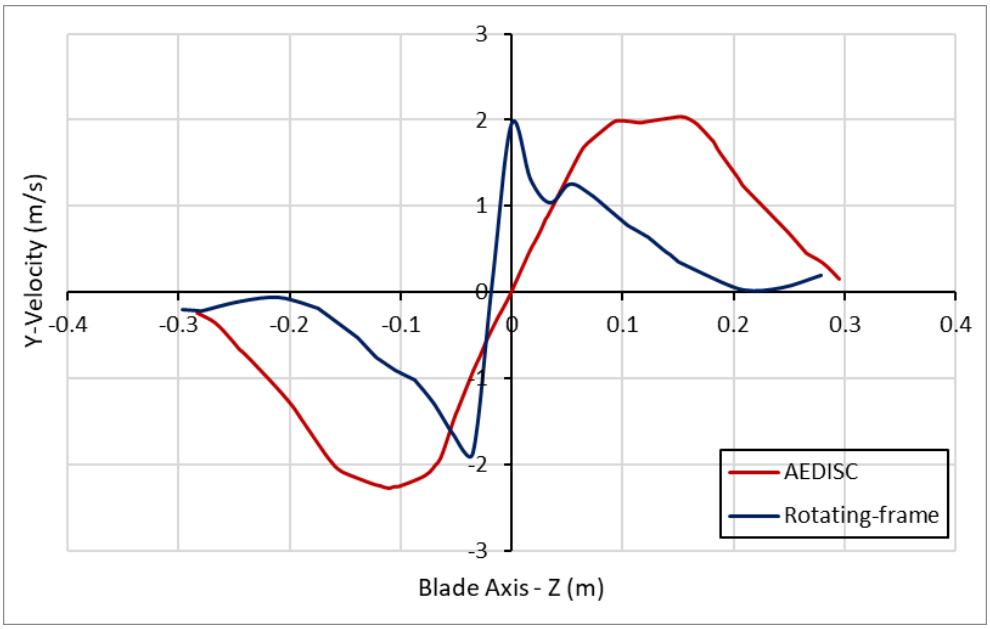

(d) y-velocity on a line aligned in z-axis

Figure 4.10 (a) x velocity along y-line, (b) x velocity along z-line (c) z velocity along y-line and (d) z velocity along z-line at 0.1 m downstream of the Rotating Component at advance ratio of 0.5 and RPM = 3000.

The progression of axial and tangential velocities downstream of the rotating components on the y-line and z-line at an advance ratio of 0.5 and 3000 RPM is illustrated in Figure 4.10. When compared to Figure 4.9, the most noticeable difference in the plots is the behavior of induced axial and tangential velocities near the hub in the rotating frame approach, which can be attributed to the absence of the spinner geometry in the AEDISC model (Matveev et al., 2023).

Apart from the velocity profiles near the hub region, similar observations made for the advance ratio 0.28 case can be applied when analyzing Figure 4.10 as a whole. The difference obtained by comparing y line and z line, based on the axisymmetric assumption in maximum axial velocity in AEDISC model becomes $\varepsilon_{V_{max}} = 0.702\%$. This difference becomes $\varepsilon_{V_{max}} = 8.102\%$. The error in AEDISC based on the maximum tangential velocities become $\varepsilon_{V_{max}} = 0.872\%$, and the difference in rotating frame based on the maximum tangential velocities becomes $\varepsilon_{V_{max}} =$

1.714% as can be obtained from Figure 4.10c and Figure 4.10d. It should be noted that the overall tangential velocity distribution in y and z lines obtained from rotating frame approach demonstrates a significant change. The ability to demonstrate axisymmetric behavior of the AEDISC model is evident when the rotating frame approach fails to do so, as can be observed by comparing Figures 4.10a – 4.10b, and Figures 4.10c-4.10d.

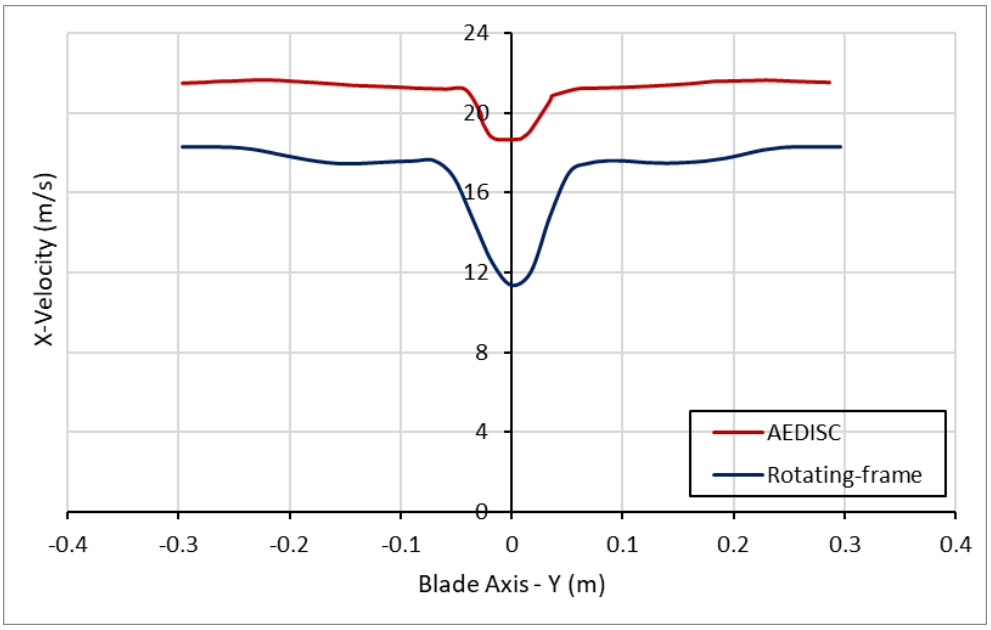

(a) x-velocity on a line aligned in y-axis

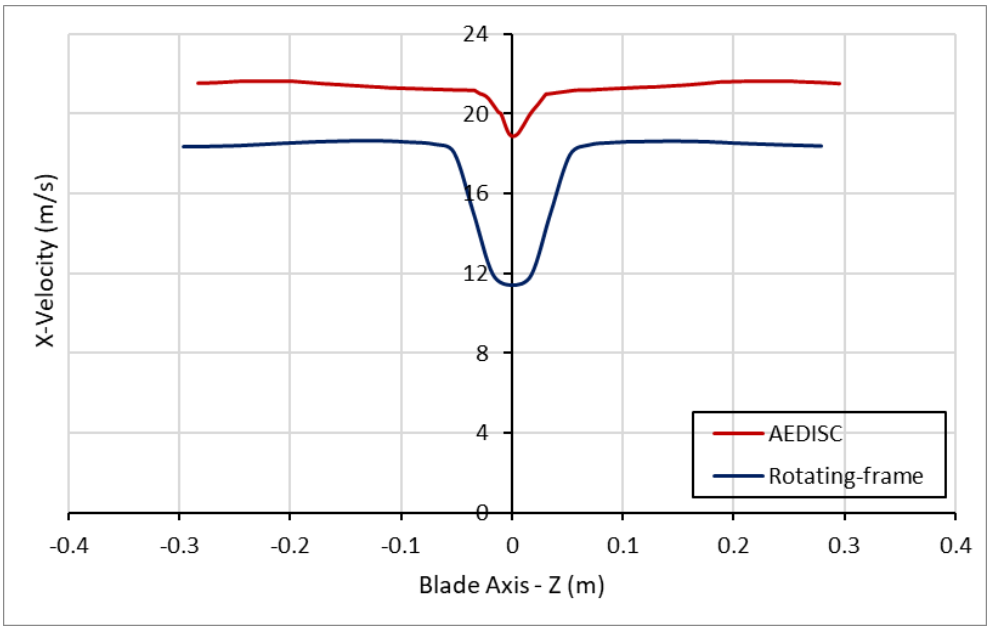

(b) x-velocity on a line aligned in z-axis

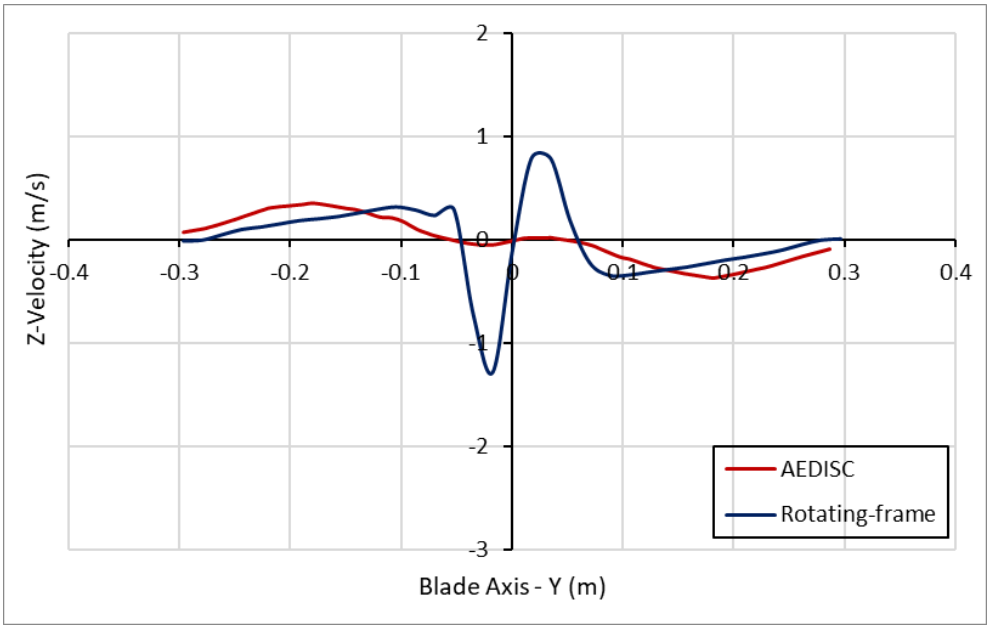

(c) z-velocity on a line aligned in y-axis

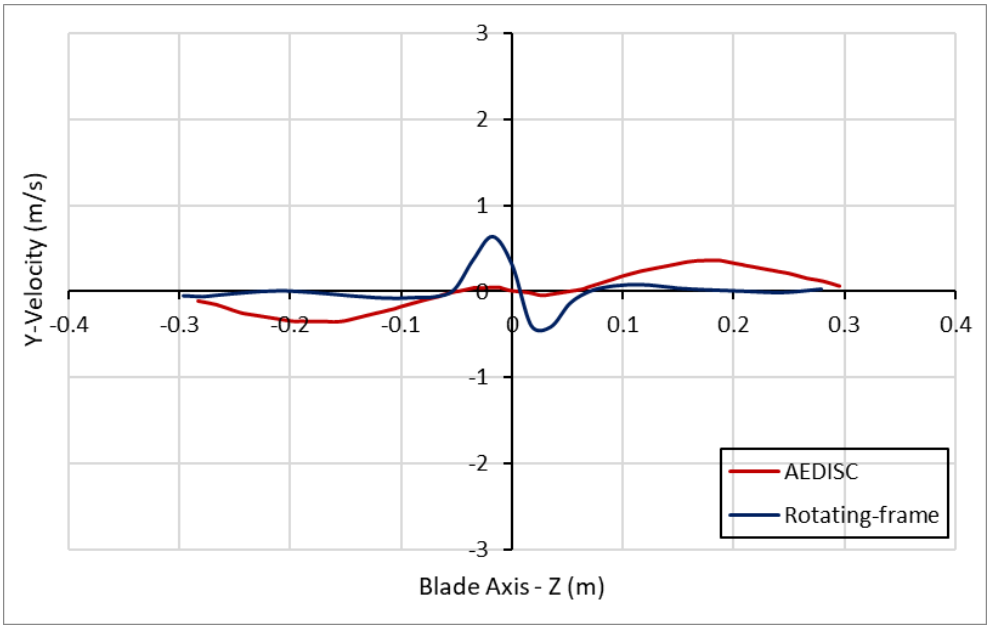

(d) y-velocity on a line aligned in z-axis

Figure 4.11. (a) x velocity along y-line, (b) x velocity along z-line (c) z velocity along y-line and (d) z velocity along z-line at 0.1 m downstream of the Rotating Component at advance ratio of 0.763 and RPM = 3000.

Figure 4.11 presents the progression of flow velocities downstream of the rotating components on the y-line and z-line at an advance ratio of 0.768 and 3000 RPM. The highest velocities in the domain are observed at this advance ratio. When Figure 4.11a and Figure 4.11b are examined, it can be observed that the maximum axial flow velocity behind the propeller is relatively higher than the ones presented for $J = 0.28$ (Figure 4.9) and $J = 0.5$ (Figure 4.10) making it challenging to predict the effects of the rotating component on axial velocities.

The difference between maximum axial velocities in AEDISC and rotating frame approach is obtained as 3.344 m/s on the y line, whereas this difference becomes 3.002 m/s on the z line. Although the difference between the thrust coefficients is observed relatively smaller in $J = 0.768$ between AEDISC and rotating frame

based on Figure 4.1, relatively higher dynamic pressures in this advance ratio proves to have a significant effect on the flow velocities behind the propeller.

Following the previous difference definition based on the axisymmetric expectations, the absolute relative percentage difference in maximum axial velocities between the AEDISC and rotating frame is calculated as $\varepsilon_{V_{max}} = 0.097\%$, and the same difference is calculated as $\varepsilon_{V_{max}} = 1.753\%$, examining Figure 4.11a and Figure 4.11b. The absolute relative percentage difference in maximum tangential velocities in AEDISC method becomes $\varepsilon_{V_{max}} = 0.325\%$, whereas in rotating frame this difference is computed as $\varepsilon_{V_{max}} = 67.75\%$ due to hub interaction demonstrating a significant non-axisymmetric behavior.

In summary, the overall shift in velocity profiles between the AEDISC and rotating frame approaches in three different advance ratios aligns with the results obtained for the flow coefficients (Figure 4.1). Generally, at 3000 RPM, the AEDISC model yields slightly higher thrust and power coefficients compared to the rotating frame approach. Consequently, the axial and tangential velocity distributions downstream are also higher in the AEDISC model. The increased flow coefficients lead to higher momentum sources and increased velocities in the downstream.

The primary difference between the two models becomes apparent when comparing the axial and tangential velocities along both the y-line and z-line, where similar distributions are expected in an ideal scenario. The AEDISC model confirms these expectations by displaying nearly identical axial and tangential velocity distributions on both lines, while the rotating frame approach fails to do so. In fact, the axial and tangential velocities on the z-line are lower than those on the y-line, indicating the significant impact of the frozen rotor assumption in the rotating frame approach on the downstream flow of rotating components.

CHAPTER 5

CONCLUSION

The current study presents a comprehensive study on a new actuator disc model called AEDISC, which has been incorporated into the SU2 software. The need for this new model arises from the high computational resources required by other methods, such as sliding mesh approaches, and the limitations of the rotating frame approach and blade element momentum theory in effectively calculating flow characteristics downstream of rotating components without a significant computational demand.

To validate the implementation of the model, a high-fidelity 2D aerodynamic database is generated. Modifications are made to account for 3D rotational effects, such as implementing a stall delay model and modelling high angles of attack. The results show that the accuracy of the aerodynamic database significantly influenced the comparisons given for the thrust and power coefficients with different methodologies. Based on the comparisons given for with and without the stall delay model, it is proved that the 3D correction methodologies have significant effects on the thrust and power coefficients as well.

The comparisons of flow coefficients showed that the AEDISC model closely approximated the experimental data, particularly at lower rotational velocity. The rotating frame approach performed less accurately in terms of flow coefficients, but still produced results that follow similar trends with the experimental data. The main differences between the two approaches were attributed to the coarser surface meshes used in the rotating frame approach due to computational limitations, as well as the AEDISC models' ability to uniformly obtain flow coefficients across all sections at the same radial position. This is enhanced by the AEDISC model assuming an infinite number of blades within the actuator disc domain.

The comparisons were made in terms of downstream velocities between the AEDISC model and rotating frame approach. The results demonstrated that the rotating frame approach failed to provide an axisymmetric velocity distribution at the same radius. This was primarily attributed to the frozen rotor assumption in the rotating frame approach, where the blades were assumed to be fixed in one constant position. The velocity values downstream exhibited differences when examining the distribution along horizontal and vertical lines. However, AEDISC model accurately captured the axisymmetric behavior induced velocities downstream.

Three main advantages of the AEDISC model have been highlighted in the current study which shows that AEDISC model can be an option for the CFD computations of the rotating blades. The reduction is obtained in computational resources and time, when one used the AEDISC model. The aerodynamic databases generated only once can be used to perform computations in several operating conditions or existing databases such as experimental results can be used for the analysis. AEDISC also proved to produce less error in the thrust and the power coefficients when compared to experimental data than the rotating frame approach, by applying 3D correction methodologies to the aerodynamic database. The axisymmetric flow distribution behind the rotating blades could be assessed by the AEDISC model more accurately than the rotating frame approach, which makes the AEDISC model an efficient method for evaluating the phenomena such as slipstream effect of the propeller and wake interaction.

As a future work, momentum sources can be modified in such a way that the effect of the spinner geometry can be included more efficiently. This can be enhanced by reducing the velocity values between the origin point of the blade and the hub. Another improvement could be to include the effect of turbulence that increases when blades are physically included in the computation. This can be done by adding turbulence sources such as to increase the turbulent kinetic energy.

REFERENCES

Adjiri, S., Dobrev, I., Benzaoui, A., Nedjari-Daaou, H., & Massouh, F. (2022). New Actuator Disc Model for the Analysis of Wind Turbines Wake Interaction with the Ground. *Journal of Applied Fluid Mechanics, 16(1), 75-88.*

Akay, B., Kurtulus, D.F., Alemdaroglu, N. (2007) Unsteady Aerodynamics of Different Wing Profiles at Low Reynolds Number. RTO-MP-AVT-146, NATO AVT-146 *Symposium on Platform Innovations and System Integration for Unmanned Air, Land and Sea Vehicles*, 14-17 May 2007, Florence, Italy.

Balduzzi, F., et al. (2018). A hybrid BET-CFD model for effective numerical siting analyses of wind turbines in the urban environment. *Journal of Physics: Conference Series, 1037, 072029.*

Bak, C. (2010). Aerodynamic design of wind turbine rotors. *Risø-I-Report.*

Branlard, E. (2017). Wind Turbine Aerodynamics and Vorticity-Based Methods: Fundamentals and Recent Applications. *Springer. doi:10.1007/978-3-319-55164-7.*

Chen, H. C., & Koop, A. (2023). High-fidelity CFD simulations for the wake characteristics of the NTNU BT1 wind turbine. *Energy, 265, 126285.*

Corrigan, J. J., & Schillings, J. (1994). Empirical model for stall delay due to rotation. *In American Helicopter Society Aeromechanics Specialists Conference, San Francisco, CA.*

Critzos, C. C., Heyson, H. H., & Boswinkle, R. W. Jr. (1955). Aerodynamic characteristics of NACA 0012 airfoil section at angles of attack from 0 degrees to 180 degrees. *NACA Technical Report 3361.*

Deters, R.W., Ananda, G.K., and Selig, M.S., Reynolds Number Effects on the Performance of Small-Scale Propellers, *AIAA Aviation and Aeronautics Forum and Exposition (Aviation 2014), AIAA Paper 2014-2151, Atlanta, GA, June 2014.*

Di Mascio, A., Muscari, R., & Dubbioso, G. (2014, July 31). On the wake dynamics of a propeller operating in drift. *Journal of Fluid Mechanics, 754, 1-19.*

Đurasević, S., Gatin, I., & Jasak, H. (2022). Partially Rotating Grid Method for Prediction of Self-Propulsion Characteristics. *In Proceedings of the 25th Symposium on the Theory and Practice of Shipbuilding.*

Durmaz, O., Karaca, H.D., Ozen, G.D., Kasnakoglu, C., Kurtulus, D.F. (2013) Dynamical Modeling of the Flow over a Flapping Wing using Proper Orthogonal Decomposition and System Identification Techniques, *Mathematical and Computer Modelling of Dynamical Systems, Volume 19, Issue 2, pp.133-158.*

Economon, T. D., Palacios, F., Copeland, S. R., Lukaczyk, T. W., & Alonso, J. J. (2016). SU2: An Open-Source Suite for Multiphysics Simulation and Design. *AIAA Journal, 54(3).*

Froude, W. (1878). On the elementary relation between pitch, slip and propulsive efficiency. *Trans. Roy. Inst. Naval Arch., 19(47), 47-57.*

Galimberti, L., Morelli, M., Guardone, A., & Zhou, B. Y. (2023). Propeller Noise Prediction Capabilities within SU2. *In AIAA 2023-1548, Propeller, Open Rotor, and Rotorcraft Noise.*

Glauert, H. (1935). Airplane Propellers. In W.F. Durand (Ed.), *Aerodynamic Theory, Vol. IV, Division L (pp. 169-360). New York: Springer.*

Gray, V. H. (1941). Wind-Tunnel Tests of Two Hamilton Standard Propellers Embodying Clark Y and NACA 16-Series Blade Sections *(NACA Report No. 530).*

Gunaydinoglu, E., Kurtulus, D.F. (2020) Pressure–velocity coupling algorithm-based pressure reconstruction from PIV for laminar flows, *Experiments in Fluids, 61: 5, https://doi.org/10.1007/s00348-019-2831-1.*

Guo, Q., Zhou, L., & Wang, Z. (2015). Comparison of BEM-CFD and full rotor geometry simulations for the performance and flow field of a marine current turbine. *Renewable Energy, 76, 177-186. DOI:10.1016 2014.10.047.*

Gur, O., & Rosen, A. (2005). Propeller performance at low advance ratio. *AIAA Journal of Aircraft, 42(2), 435-441.*

Hansen, M. O. L. (2008). Aerodynamics of Wind Turbines - *Second Edition. London, UK: Earthscan.*

Hansen, M. O. L., Sørensen, J. N., Voutsinas, S., Sørensen, N., & Madsen, H. Aa. (2006). State of the art in wind turbine aerodynamics and aeroelasticity. *Progress in Aerospace Sciences, 42(4), 285-330.*

Himmelskamp, H. (1947). Profile investigations on a rotating airscrew. MAP Volkenrode, *Reports and Translation, (832).*

Iannini, A. (2022). CFD investigation of a tandem propellers configuration for eVTOL aircraft in airplane mode flight condition (Publication No. 963949). [*Master's thesis, Politecnico Milano*].

ISO/IEC. (2020). ISO/IEC Standard 14882: *Programming Language C++* [Standard]. Retrieved from https://www.iso.org/standard/79358.html.

J.B. Brandt, R.W. Deters, G.K. Ananda, O.D. Dantsker, and M.S. Selig (2023) *UIUC Propeller Database, Vols 1-4*, University of Illinois at Urbana-

Champaign, Department of Aerospace Engineering, retrieved from https://m-selig.ae.illinois.edu/props/propDB.html.487

Jones, W. P., & Launder, B. E. (1972). The prediction of laminarization with a two-equation model of turbulence [*Model*]. Retrieved from https://www.cambridge.org/9780521309769.

Kaya, D., Kutay, A. T., Kurtulus, D.F., Tekinalp, O., Simsek, I., Soysal S., Hosgit, G. (2016), Propulsion System Selection and Modeling for a Quadrotor with Search and Rescue Mission, 54th AIAA Aerospace Sciences Meeting San Diego, California, USA, 4-8 January 2016, AIAA 2016-1528.

Kurtulus, D.F. (2022) Critical Angle and Fundamental Frequency of Symmetric Airfoils at Low Reynolds Numbers, Journal of Applied Fluid Mechanics, Volume 15, Number 3, May 2022, pp.723-735, 10.47176/JAFM.15.03.33099.

Kurtulus, D. F. (2021) Vortex flow aerodynamics behind a symmetric airfoil at low angles of attack and Reynolds Numbers, International Journal of Micro Air Vehicles, doi: 10.1177/17568293211055653, Volume 13: 1–18

Kurtulus DF, David L, Farcy A, Alemdaroglu N (2006a) A Parametrical Study with Laser Sheet Visualization for an Unsteady Flapping Motion. AIAA-2006-3917, 36th AIAA Fluid Dynamics Conference and Exhibit, San Francisco, California USA, 5 - 8 June 2006.

Kurtulus, D. F., David, L., Farcy, A., Alemdaroglu, N. (2006b) Laser Sheet Visualization for Flapping Motion in Hover. AIAA-2006-0254, 44rd AIAA Aerospace Sciences Meeting and Exhibit, Reno, Nevada, USA, 9 - 12 Jan 2006.

Kurtulus, D.F., Farcy, A., Alemdaroglu, N. (2005) Unsteady Aerodynamics of Flapping Airfoil in Hovering Flight at Low Reynolds Numbers. AIAA-2005-1356, 43rd AIAA Aerospace Sciences Meeting and Exhibit, Reno, Nevada, USA, 10 - 13 Jan 2005.

Kurtulus, D.F., Farcy, A., Alemdaroglu N. (2004) Numerical Calculation and Analytical Modelization of Flapping Motion. Proceeding of 1st European Micro Air Vehicle Conference and Flight Competition. Braunschweig, Germany, 13-14 July 2004.

Leray, J. (1934). "Sur le mouvement d'un liquide visqueux emplissant l'espace." *Acta Mathematica, 63(1), 193-248.*

Lloyd, T., Lafeber, F. H., & Bosschers, J. (2022). Predicting cavitating propeller noise in off-design conditions using scale-resolving CFD simulations. *Ocean Engineering, 254, 111176.*

MacNeill, R., & Verstraete, D. (2017). Blade element momentum theory extended to model low Reynolds number propeller performance. *The Aeronautical Journal, 121(1240), 835.*

Mach, E. (1871). Über den Einfluss der Temperatur auf die Schallgeschwindigkeit in Gasen [On the Influence of Temperature on the Speed of Sound in Gases]. Sitzungsberichte der Kaiserlichen Akademie der Wissenschaften, *Mathematisch-Naturwissenschaftliche Classe, Abt. IIa, 63.*

Mahmuddina, F. (2016). The Effect of Flat Plate Theory Assumption in Post-Stall Lift and Drag Coefficients Extrapolation with Viterna Method. *Journal of Subsea and Offshore.*

Maalouly, M., Souaiby, M., ElCheikh, A., Issa, J. S., & Elkhoury, M. (2022). Transient analysis of H-type Vertical Axis Wind Turbines using CFD. *Energy Reports, 8, 4570-4588.*

Matveev, K., Conroy, K., & Tibbitts, S. (2023). Performance and Rotor-Body Interactions of Novel eVTOL in Moderate-Speed Cruise. *AIAA 2023-1724.*

Menter, F. R. (1994). Two-equation eddy-viscosity turbulence models for engineering applications [*Model*]. Retrieved from https://www.dlr.de/as/en/Portaldata/1/Resources/standards/archiv/sst_beitrag_paper.pdf.

Morgado, J., Silvestre, M. Â. R., & Páscoa, J. C. (2014). Validation of New Formulations for Propeller Analysis. *Journal of Propulsion and Power, DOI: 10.2514/1.B35240.*

Morellia, M., Bellostaa, T., & Guardonea, A. (2021). Development and Preliminary Assessment of the Open-Source CFD toolkit SU2 for Rotorcraft Flows. *Journal of Computational and Applied Mathematics.*

Naeem, N., Fouda, M., Guney, M., Kurtulus, D. F. (2023) Wake patterns and mode switching at low Reynolds numbers, *Progress in Computational Fluid Dynamics, An International Journal , Vol. 23, No.2, pp.87-110. https://doi.org/10.1504/PCFD.2023.129762*

Nguyen, L. T., & Eça, L. (2022). The use of azimuthal equidistribution of lifting line circulations to model flow past wind turbines in yaw. *Wind Energy Science, 7(1), 1-21.*

Ning, S. A., Hayman, G., Damiani, R., & Jonkman, J. (2015). Development and validation of a new blade element momentum skewed-wake model within AeroDyn. Preprint. Brigham Young University, National Renewable Energy Laboratory. *Presented at the AIAA Science and Technology Forum and Exposition 2015*, Kissimmee, Florida, January 5-9, 2015

Oktay, T., & Eraslan, Y. (2020). Numerical Investigation of Effects of Airspeed and Rotational Speed on Quadrotor UAV Propeller Thrust Coefficient. *Journal of Aviation. Advance online publication. https://doi.org/10.30518/jav.872627*

Palacios, F., Colonno, M. R., Aranake, A. C., Campos, A., Copeland, S. R., Economon, T. D., Lonkar, A. K., Lukaczyk, T. W., Taylor, T. W. R., & Alonso, J. J. (2013). Stanford University Unstructured (SU2): An open-source integrated computational environment for multi-physics simulation and design. *In AIAA.*

Posa, A., Broglia, R., & Balaras, E. (2021). The wake flow downstream of a propeller-rudder system. *International Journal of Heat and Fluid Flow, 87, 108765.*

Ramirez, G. R., de Oliveira, W., da Silva, E. R., & Niño Del Río, G. E. (2022). Free and Non-Free Vortex Design for Axial Fans with Circumferential Sweep through CFD Techniques. *Journal of Applied Fluid Mechanics, 15(4), 1017-1034.*

Reynolds, O. (1883). An Experimental Investigation of the Circumstances which Determine Whether the Motion of Water Shall Be Direct or Sinuous, and of the Law of Resistance in Parallel Channels. *Philosophical Transactions of the Royal Society of London, 174, 935-982.*

Sahbaz, M., Sezer-Uzol, N., Kurtulus, D. F. (2017) Computational Analysis of a Model Scale Helicopter Rotor in Ground Effect, *AIAC-2017-109, Ankara International Aerospace Conference, 20-22 September 2017, Ankara*

Shamsia, R., Ghassemi, H., & Iranmanesh, M. (2017). A Comparison of the BEM and RANS Calculations for the Hydrodynamic Performance of the PODS. *Mechanics & Industry, 18, 205.*

Silvestre, M.A.R., Morgado, J., Alves, P., Santos, P., Gamboa, P., & Páscoa, J.C. (2015). Propeller Performance Measurements at Low Reynolds Numbers. *International Journal of Mechanics*, 9.

Snel, H., Houwink, R., & Bosschers, J. (1994). Sectional prediction of lift coefficients on rotating wind turbine blades in stall. *Netherlands Energy Research Foundation (ECN) Technical Report*, ECN-C-93-052.

Stergiannis, N., Lacor, C., Beeck, J. V., & Donnelly, R. (2016). CFD modelling approaches against single wind turbine wake measurements using RANS. *Journal of Physics: Conference Series, 753, 032062*.

SU2 Team. (2023). Jekyll Doc Theme (Version 7.5.1) [*Computer software*]. Retrieved from https://su2code.github.io/

Tangler, J. L., & Selig, M. S. (1997). An evaluation of stall delay due to HAWTs. *National Renewable Energy Laboratory*, NREL/CP-440-23258.

Theodorsen, T., Garrick, I. E., & Houghton, E. L. (1937). Characteristics of Six Propellers Including the High-Speed Range (*NACA Report No. 594*).

Utkarsh Ayachit. 2015. The ParaView Guide: A Parallel Visualization Application. *Kitware, Inc*., Clifton Park, NY, USA.

Vijayanandha, R., Arul Prakash, R., Manivel, R., Kiran, P., Sudharsan, R., Raj Kumar, G., & Raffik, R. (2022). Design and Parametric Study of Counter-Rotating Propeller of Unmanned Aerial Vehicles for High-Payload Applications based on CFD-MRF Approach. *International Journal of Vehicle Structures & Systems*, 14(7), 840-848.

Viterna, L., & Corrigan, R. (1982). Fixed Pitch Rotor Performance of Large Horizontal Axis Wind Turbines. *In DOE/NASA Workshop on Large Horizontal Axis Wind Turbine Technology*.

Zou, L., & Zuo, Z. (2014). Influence of Reynolds number and angle of attack on the aerodynamic performance of propellers. *Journal of Aerospace Engineering*, 28(6), 04014109. DOI: 10.1061/(ASCE)AS.1943-5525.0000420.

APPENDICES

A. Problem Definition in the Main Configuration File Needed for AEDISC

% ---------- DIRECT, ADJOINT, AND LINEARIZED PROBLEM DEFINITION ----------%

SOLVER= RANS

KIND_TURB_MODEL= SST

MATH_PROBLEM= DIRECT

MULTIZONE=YES

MULTIZONE_MESH=NO

% ---------- Sub-configurations files for rotating and stationary zones should be provided here ----------%

CONFIG_LIST= (zone_fluid.cfg, zone_prop.cfg)

SYSTEM_MEASUREMENTS= SI

% ---------- Interface boundaries between the rotating and stationary zones should be provided here ----------%

MARKER_ZONE_INTERFACE= (Inner_Inlet, Outer_Inlet, Inner_Side_Inner, Outer_Side_Inner, Inner_Side_Outer, Outer_Side_Outer, Inner_Outlet, Outer_Outlet)

MARKER_FLUID_INTERFACE= (Inner_Inlet, Outer_Inlet, Inner_Side_Inner, Outer_Side_Inner, Inner_Side_Outer, Outer_Side_Outer, Inner_Outlet, Outer_Outlet)

B. Sub-configuration File for the Stationary Zone in General

% ---------- DYNAMIC MESH DEFINITION ----------%

% The mesh generated for the stationary fluid zone should be provided here either in su2 or cgns format

MESH_FILENAME= disc_outer.su2

MESH_FORMAT= SU2

% Type of dynamic mesh (NONE, ROTATING_FRAME, AEDISC)

% Type of dynamic mesh is set to NONE, in order to model a stationary zone in this domain

GRID_MOVEMENT= NONE

C. Sub-configuration File for the Rotating Zone in AEDISC

% ---------- DYNAMIC MESH DEFINITION ----------%

% The mesh generated for the stationary fluid zone should be provided here either in su2 or cgns format

MESH_FILENAME= disc_inner.su2

MESH_FORMAT= SU2

% Type of mesh motion (NONE, FLUTTER, RIGID_MOTION)

% Type of mesh motion is set to AEDISC to activate the model

GRID_MOVEMENT= AEDISC

% Name of the input file for AEDISC application for blade properties

AEDISC_BLADE_FILENAME= AEDISC_Blade_Info.dat

% Name of the input file for AEDISC application for section properties

AEDISC_SECTION_FILENAME= AEDISC_Section_Info.dat

D. Input File Required in AEDISC Model to Represent the Blade Properties

AE Center of Rotation: Center rotation of the propeller. This should be compatible with mesh data.

AE Rotation axis: Axis of rotation of the propeller. You may define yaw, roll or pitch of the propeller by this data.

AE Radius: Radius of the propeller.

AE Rotation Rate: Rotation rate of the propeller around rotation axis. (rad/s)

AE Number of Blades: Number of blades in propeller. This value is used to calculate propeller solidity.

AE Number of Sections: Number of dividing sections for blade element theory.

Author: Kaan Yenipazar E-mail: kyenipazar@simscale.com Date: 30.03.2022

AE Center of Rotation= 0 0 0

AE Rotation Axis= -1 0 0

AE Radius= 0.24

AE Rotation Rate= 315

AE Number of Blades= 2

AE Number of Sections= 18

#r/R	chord(m)	pitch(deg)
0.15	0.02688	34.11
0.2	0.03024	42.88
0.25	0.03384	40.83
0.3	0.03648	35.05
0.35	0.03792	30.43
0.4	0.0384	26.83
0.45	0.03816	23.97
0.5	0.03696	21.64
0.55	0.03528	19.73

0.6	0.03312	17.93
0.65	0.03048	16.26
0.7	0.02736	14.95
0.75	0.02448	13.81
0.8	0.02136	12.98
0.85	0.01848	12.19
0.9	0.0156	11.81
0.95	0.01176	11.25

E. Input File Required in AEDISC Model to Represent the Section Properties

nSection: Number of dividing sections of the blade, to be used for blade element theory.

nMach: Number of Mach number computing points.

nAoa: Number of angle of attack computing points.

nReynolds: Number of Reynolds number computing points.

Section database should be in the form of square matrix. Each mach number value should have a case for all aoa values etc.

During iteration, any value outside the boundary of given database will be equated to the closest boundary value.

Author: Kaan Yenipazar E-mail: kyenipazar@simscale.com Date: 30.03.2022

#---

nSection= 9

nMach= 3

nAoa= 20

nReynolds= 4

#r/R	mach	Reynolds	aoa	cl	cd
0.2	0.06	10000	-180	-0.00000	0.058927
0.2	0.06	10000	-179	0.0925554	0.059314

…

#The rest of the 2D aerodynamic database should be inserted here.